Title
Monitoring Distributed, Dynamic Strain in Civil Infrastructure using Phase-Sensitive Optical Time-Domain Reflectometry

Author
Hubbard, Peter G

Publication Date
2022

Peer reviewed|Thesis/dissertation

Monitoring Distributed, Dynamic Strain in Civil Infrastructure using Phase-Sensitive Optical Time-Domain Reflectometry

by

Peter George Hubbard

A dissertation submitted in partial satisfaction of the

requirements for the degree of

Doctor of Philosophy

in

Engineering - Civil and Environmental Engineering

in the

Graduate Division

of the

University of California, Berkeley

Committee in charge:

Professor Kenichi Soga, Chair
Professor James W. Rector
Professor Alberto Sangiovanni-Vincentelli

Summer 2022

Monitoring Distributed, Dynamic Strain in Civil Infrastructure using Phase-Sensitive Optical Time-Domain Reflectometry

Abstract

Monitoring Distributed, Dynamic Strain in Civil Infrastructure using Phase-Sensitive Optical Time-Domain Reflectometry

by

Peter George Hubbard

Doctor of Philosophy in Engineering - Civil and Environmental Engineering

University of California, Berkeley

Professor Kenichi Soga, Chair

The micro-scale mechanical behavior of civil infrastructure and the earth immediately surrounding it is indicative of material properties, condition and use level. In addition, the geometry of infrastructure systems can be complex and spanning large extents. Phase-sensitive optical time domain reflectometry (ϕ-OTDR), also known as distributed acoustic sensing (DAS) or distributed vibration sensing (DVS), is a revolutionary technology that uses interferometry within optical fibers to make distributed measurements of strain at higher precision than ever before possible. This technology can measure extremely small strains (nanostrain level) at high spatial resolutions (several meters) and over long distances (10's of kilometers). Since ϕ-OTDR can measure such small perturbations, it has gained widespread attention within the earth and planetary science community for measuring seismic wave propagation. These measurements have been predominantly focused on capturing the phase behavior of seismic waves at a crustal or exploration scale. However, for application to measuring dynamic strain in civil infrastructure the measurements must be understood for their strain magnitude as well as phase behavior. This dissertation serves to demonstrate the use of ϕ-OTDR for monitoring civil infrastructure systems through the presentation of several practical verification cases. Optical fibers were coupled to a soil site, a pavement system, and a superstructure to demonstrate how ϕ-OTDR can be used to quantitatively measure dynamic strain in these elements. The ϕ-OTDR measurements were verified through the use of velocity transducers (geophones), strain gauges, and another distributed fiber optic sensing technique called optical frequency-domain reflectometry (OFDR). Numerical modeling of ϕ-OTDR measurements is demonstrated for describing the measurements in a pseudo-static case as well as during stress-wave propagation. It is shown that ϕ-OTDR provides capabilities for monitoring civil infrastructure that currently-used techniques cannot due to its superior measurement precision and high acquisition rates. ϕ-OTDR is demonstrated as a new tool for monitoring civil infrastructure.

For Katie and Evelyne

Contents

List of Figures

List of Tables

Acknowledgments

I would like to sincerely thank Professor Kenichi Soga for the opportunity to pursue my Ph.D., the continuous encouragement, inspiration and support. I would like to thank my colleagues at the Soga Research Group including Dr. James Wang, Dr. Linqing Luo, Yaobin Yang, Tianchen Xu, Andrew Yeskoo, Dr. Ruonan Ou, Hayato Nonaka, Jaewon Saw, and James Xu for their friendship and support of the field acquisitions detailed in this work. Special thanks to Professor Brady Cox, Professor Joseph Vantassel, Michael Yust, Dr. Farnyuh Menq and Robert Kent for working with me on the field acquisition in Austin, TX (Chapter 3) and the subsequent analysis. I would also like to thank the OptaSense team for supporting me with a wealth of experience, knowledge and instrumentation support, specifically Dr. Chris Minto, Dr. Martin Karrenbach, Todd Bown, Paul Clarkson and Ray Sutyla.

Chapter 1

Introduction

1.1 Background

Distributed fiber optic sensing (DFOS) is a family of innovative technologies that turn an otherwise passive length of optical fiber into a nerve-like receptor that can sense deformation, temperature and vibration over long lengths (10's to 100's of km) at high resolution (meter-scale) and fast speeds (thousands of measurements per second). DFOS technologies have been rapidly improving within the fields of optics and electrical engineering over the last few decades and there is a rich potential for applications that have major societal impact.

At the same time, the civil infrastructure that society relies on every day is facing a growing list of challenges including age-induced deterioration, which recent to the time of this dissertation's writing contributed to the Surfside condominium and Fern Hollow Bridge collapses [1, 2]. Structural health monitoring (SHM) is a concept of evaluating the health of built structures and their surroundings to mitigate the risks of infrastructure failures [3]. DFOS has been a leading technology in research for use in SHM because of its simple centralized architecture, lack of complex individual sensors and ability to localize problematic phenomena that may be missed by point-based systems [4].

However, DFOS implementation for civil engineering has focused on the monitoring of static strain and temperature. Dynamic behavior, such as structural vibrations and wave propagation has been elusive for DFOS to capture. Dynamic behavior is critical for SHM because it indicates both the vibrational behavior of materials as well as transient events that slow measurement frequencies miss. In addition to measurement rates, DFOS technologies used for strain monitoring in civil engineering have focused on relatively large strains (10's of $\mu\varepsilon$). Measuring much smaller strain levels is useful for directly detecting damage in infrastructure before it becomes a problem as well as measuring small strains caused by infrastructure use.

A DFOS technique called phase-sensitive optical time-domain reflectometry (ϕ-OTDR) is extremely promising for civil infrastructure monitoring because it has the potential to measure strains at the sub-nanostrain level ($1 \times 10^{-9} \frac{m}{m}$) at repetition rates of several thousand

samples per second and distances of over 100 km. Employing ϕ-OTDR can open an entirely new field of monitoring extremely small changes in infrastructure over long distances to determine performance degradation as well as real-time use characteristics. Exploring the potential of ϕ-OTDR for use in civil infrastructure is the purpose of this dissertation.

1.2 Hypothesis and Research Objectives

It is hypothesized that the ϕ-OTDR sensing technique can be used to monitor the dynamic strain in civil infrastructures with a combination of strain precision, acquisition rate and maximum measurement length superior to any other available DFOS technique currently used. Thus, measurements can be conducted to achieve a wide-ranging combination of observations including the high amplitude dynamics of superstructures to low amplitude strain-wave propagation in soils and even small-strain behavior of pavements during road use. The objectives of this dissertation are:

1. Develop installation procedures and validate the strain measurements made in practical civil engineering deployments by comparing ϕ-OTDR to other instrumentation;

2. Test ϕ-OTDR's potential for measuring phenomena in civil infrastructure that is currently not possible with the tools common in the field due to its superior strain precision, acquisition rates and measurement distance.

1.3 Outline of the Dissertation

This dissertation consists of six chapters including this introduction and is organized as follows:

- Chapter 1 introduces the topic of the dissertation, identifies the motivation for the research and outlines the dissertation structure;

- Chapter 2 is a literature review on ϕ-OTDR, its underlying physics, development, applications, and relationship to other DFOS technologies;

- Chapter 3 demonstrates the capability of ϕ-OTDR for quantitatively measuring the dynamic strain of the ground. The spatial transfer function for horizontal ϕ-OTDR arrays is developed and its impacts on measurements are discussed. ϕ-OTDR measurements made during an active-source seismic experiment are presented and compared with standard geophones to validate the technique and explore its limitations;

- Chapter 4 explores the capability of ϕ-OTDR for measuring the small-strain behavior of pavements through a real-world deployment. ϕ-OTDR is implemented using road asphalt-embedded fiber optic cables and used to measure strains from events as large

as a truck driving to as small as an animal walking on the road. Measurements are compared with 3D finite element modeling results and another fiber optic sensing technique called optical frequency-domain reflectometry (OFDR). The advantages of ϕ-OTDR over other DFOS techniques are discussed including its superior strain precision, acquisition rate and measurement length;

- Chapter 5 implements ϕ-OTDR in a large-scale laboratory test for monitoring a superstructure under dynamic loading. A model wind turbine tower with a dynamic shaker is instrumented with ϕ-OTDR by applying a specialized attachment technique that transfers the structural strain to the optical fiber along its length. The ability of ϕ-OTDR to capture both local and global dynamic properties of the tower is explored and also compared to OFDR. The potential and advantages offered by ϕ-OTDR for real-world SHM implementations is discussed;

- Chapter 6 presents final remarks on the studies and recommends future research on the topic of ϕ-OTDR implementations for civil infrastructure monitoring.

Chapter 2

Literature Review

This literature review begins with the fundamentals of DFOS including the guiding of light in optical fibers and the backscattering phenomena that make distributed measurements possible. How optical signals are mapped in space to their backscattering location is briefly introduced, followed by the concepts of spatial resolution and sampling interval in DFOS systems. Next, DFOS techniques that have been used for sensing dynamic strain are reviewed including applications within civil engineering. The development of ϕ-OTDR is reviewed in detail including predecessor technologies. Specific architectures for ϕ-OTDR systems are presented and what makes them capable of quantitatively measuring phase changes associated with strain is discussed. An example ϕ-OTDR architecture was built in the laboratory and its measurements are used to demonstrate the measurement principle. Other common applications of ϕ-OTDR within the research community are reviewed, specifically within the earth and planetary science community. Finally, the justification of the research objectives of this dissertation is given based on the current state of knowledge.

2.1 Principles of Distributed Fiber Optic Sensing

2.1.1 Guiding Light in Optical Fiber

Fiber optic sensing was developed after the invention of fiber optic waveguides which power the internet and communication systems of the modern world. It was shown by Nobel laureate Charles Kao in the 1960's that optical fibers with a core and cladding could be created to propagate light with low enough losses to make fiber optic communication a practical technology [5]. Prior to that, it had been shown that solid and liquid media could be used to guide light, but that considerable energy was lost through absorption making their practical lengths limited [6, 7]. Guiding light in fibers relies on a contrast in index of refraction between a fiber's core and its cladding. The principle of guiding light is typically explained using ray optics and Snell's law, however this representation does not adequately describe the physics of wave propagation in single mode fibers. Nonetheless, Figure 2.1

shows the principle of total internal refraction guiding multiple modes of light waves within an optical fiber. Each ray represents the path of each mode of light wave. The principle of guiding waves demonstrated in the figure is governed by Snell's law. The relationship can be written as:

$$n_1 \sin\theta_1 = n_2 \sin\theta_2 \tag{2.1}$$

where n_1 and n_2 are the indexes of refraction of the core and cladding in Figure 2.1, respectively. θ_1 and θ_2 are the angles that the ray makes with the normal extending into core and cladding, respectively. When $\theta_2 > 90°$, the entire ray is refracted internally and does not escape the core. However, if $\theta_2 < 90°$, most of the light passes through the core-cladding interface. A small amount (on the order of a few percent) remains in the core as described by the Fresnel equations, but this power leaks out quickly from each contact with the cladding [8]. The value of θ_1 that results in $\theta_2 = 90°$ is called the critical angle, θ_c.

Figure 2.1 shows a section of optical fiber that is guiding multiple rays of light. The purple and green rays have different paths but both are effectively passed through the fiber. Since more than one light path is possible through the fiber, this is an example of a multimode fiber. The red ray does not meet the criteria ($\theta_1 > \theta_c$) to be guided, resulting in signal loss at the core-cladding interface. When multiple modes of light are guided, the different rays all have unique path lengths. This causes a once condensed optical signal, like a pulse, to disperse over a fiber's length. For this reason coherent signal propagation over long distances is difficult with multimode fibers. DFOS techniques in general do not work well with multimode fibers.

Though ray optics are a useful way to visualize the guiding of light in optical fibers, it does not adequately describe single mode fibers. Single mode fibers would only guide the purple ray in Figure 2.1. This is called the fundamental mode, and guiding it is the key to long-range optical communications and sensing.

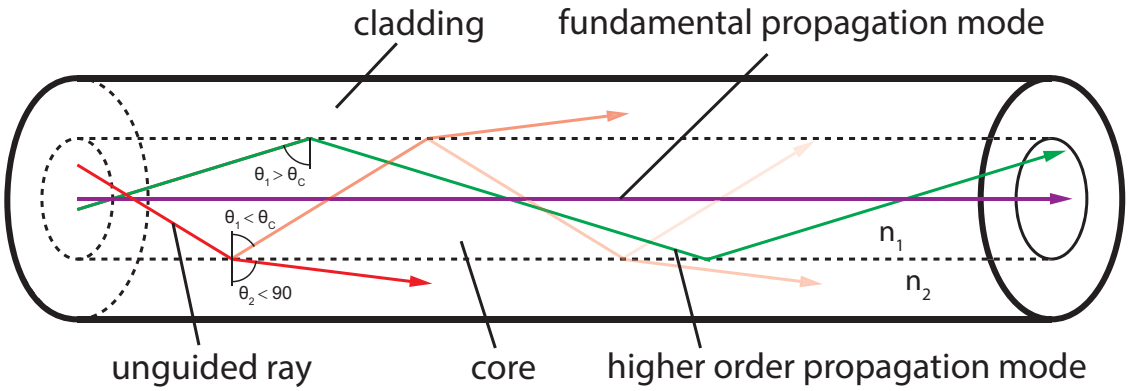

Figure 2.1: Illustration of the ray optics representation of light propagation in multimode fibers.

Single mode fibers only support one path of electromagnetic waves propagating along their length. This is achieved by having a core radius so small that other modes cannot fit. In fact, in single mode propagation a portion of the light energy travels outside of the core within the cladding. Wave optics must be used to describe single mode propagation. Light waves propagating in an optical fiber can be described using Maxwell's equations. It was shown by Gloge [9] that the solutions to Maxwell's equations for a step-indexed optical fiber can be approximated to describe the signal power as a function of radius within the fiber for different modes of propagation. This relationship is [9]:

$$\bar{p}(r) = \kappa(u^2/v^2)\frac{P}{\pi a^2}\begin{cases} J_{l^2}(ur/a)/J_{l^2}(u) & \text{within the core} \\ K_{l^2}(wr/a)/K_{l^2}(w) & \text{within the cladding} \end{cases} \tag{2.2}$$

where $\bar{p}$ is the average power density as a function of fiber radius r, u is the normalized frequency in the core, w is the normalized frequency in the cladding, κ is a mode-dependent scalar, a is the radius of the core, J is the Bessel function of the first kind, K is the Bessel function of the second kind and l is the mode index. The parameters u and w change with the design of the fiber and in-turn determine the parameter v as:

$$v^2 = u^2 + w^2 = ka\sqrt{(n_{core}^2 - n_{cladding}^2)} \tag{2.3}$$

v is dimensionless and is used to determine the number of modes that a fiber can support. If v is less than 2.405, the Bessel functions of the first kind in Equation 2.2 do not have roots other than zero, and hence only one mode can exist. Such a case is shown in Figure 2.2. The fiber described in the figure has a core radius (a) of 3 μm, refractive indexes of 1.442 and 1.440 for the core and cladding, respectively, and is used to propagate light with a wavelength of 1 μm. This results in a v value of 1.4311 and can only support a single mode. A significant portion of the signal's power, 67% in this case, is propagated outside of the core.

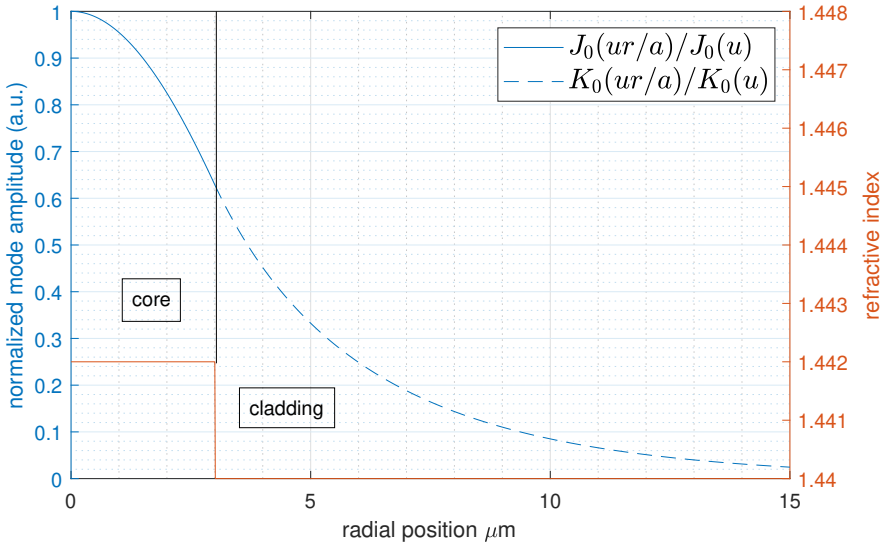

Figure 2.2: Power distribution of the guided mode within a single mode fiber for 1000 nm wavelength light with a core diameter of 3 μm, and refractive indices of 1.442 and 1.440 for the core and cladding, respectively.

If the v value is increased more modes can propagate. Figure 2.3 shows an example of this by expanding the core size of the fiber described in Figure 2.2 to 10 μm resulting in a v value of 4.770. The figure shows two of four possible modes propagated by the fiber. These are both known as hybrid modes with dominant magnetic fields (HE) and are described by Bessel functions of the 0^{th} order.

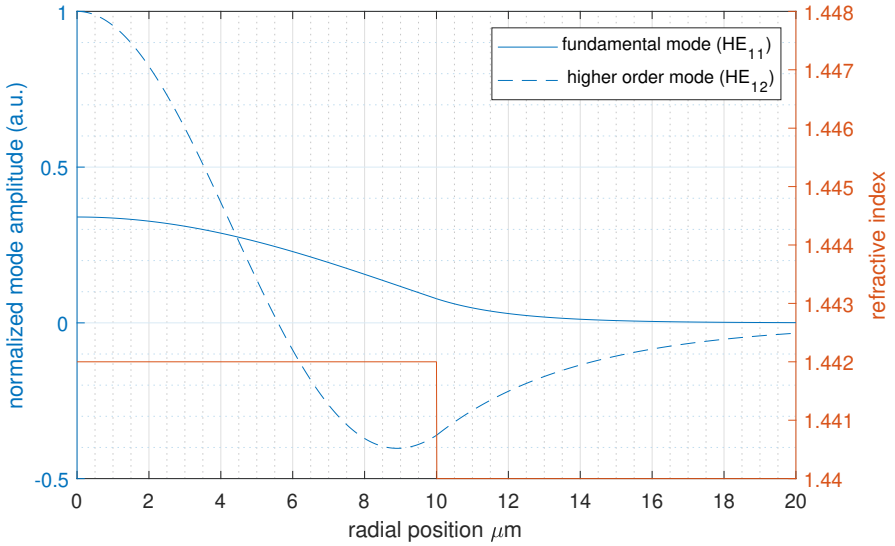

Figure 2.3: Power distribution of two modes within a multimode fiber for 1000 nm wavelength light with a core diameter of 3 μm, and refractive indices of 1.442 and 1.440 for the core and cladding, respectively.

The development and understanding of single mode fibers was crucial for implementing coherent signal propagation using fiber optics. Low-loss materials were then explored to improve the loss characteristics of optical fiber from the initial 20 dB/km estimated by Kao [5] to the modern day accepted loss value for telecommunications of 0.5-1.0 dB/km [10]. Part of this improvement was understanding that a portion of the signal field propagates in the cladding, so reducing the loss characteristics of the cladding was critical. Loss is expressed in decibels of power relative to the initially launched light according to the expression:

$$\alpha = -\frac{10}{z}\log(\frac{P(z)}{P(0)}) \tag{2.4}$$

where α is the loss in dB/km, z is the length of the fiber being examined, and P is the optical power. It is understood that losses in optical fibers come from absorption and scattering. Figure 2.4 shows the intrinsic loss in silica fiber from wavelengths 1-1.8 μm. Rayleigh scattering is the cause of most losses in silica fibers. This scattering is leveraged in DFOS because a portion of it is guided back to the beginning of the optical fiber where the incident source light was launched [11].

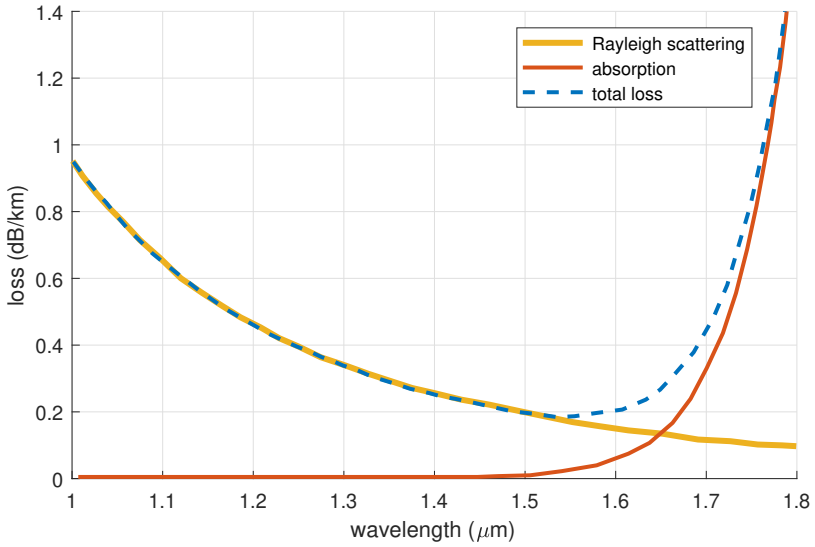

Figure 2.4: Intrinsic losses in single mode optical fiber as comprised of Rayleigh scattering and absorption (recreated from [12]).

2.1.2 Light Scattering Mechanisms

DFOS uses backscattered light within optical fibers to make observations about the fiber. There are three mechanisms for backscatter in optical fibers; Rayleigh, Brillouin, and Raman scattering. The relative spectra of each of these scattering mechanisms are shown in Figure 2.5 relative to 1550 nm-wavelength light, a common wavelength for fiber optic sensing.

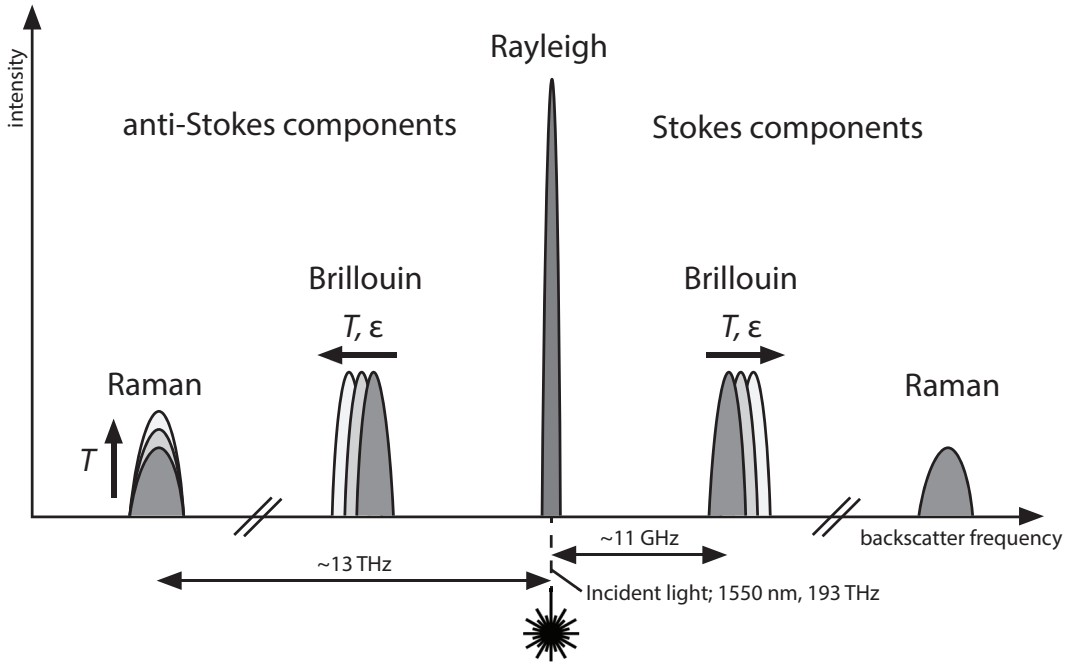

Figure 2.5: The spectra of Rayleigh, Brillouin and Raman scattering in silica optical fibers shown schematically relative to the laser wavelength of 1550 nm, a typical wavelength for fiber optic sensing.

Brillouin and Raman scattering processes are inelastic. The frequency of the scattered light is different than the laser light that caused them. Each of these types of scattering have Stokes, increased energy, and anti-Stokes, decreased energy components. Conveniently, the properties of inelastic scattering in solid media are related to changes in the physical matrix of that media. Raman scattering's anti-Stokes component intensity has a strong temperature dependence, so it is commonly used for distributed temperature sensing (DTS). For Brillouin scattering, the center frequency of both the Stokes and anti-Stokes components shift with changes in strain and temperature. Brillouin scattering is used in distributed strain and temperature sensing (DSTS). In terms of fiber optic sensing, inelastic scattering processes are convenient because they are examining an absolute condition of an optical fiber allowing for compatible measurements to be made at totally different times or even by different instruments.

Rayleigh scattering, on the other hand, is elastic so it occurs at the same frequency as the incident light. There are two main types of Rayleigh-based fiber optic sensing; interferometric and spectral analysis. In interferometric methods, the phase of the Rayleigh backscatter is used to detect a change in optical path length due to mechanical strain or temperature change [13]. This technique has been applied in a distributed manner in the case of distributed acoustic sensing (DAS) also called distributed vibration sensing (DVS). It also has been

implemented discretely by engineered scattering locations within the fiber for the interfering light to originate from [14].

Spectral analysis techniques using Rayleigh backscatter have also been used to measure strain and temperature. Spectral methods examine the relationship between the power and frequency of Rayleigh backscatter by changing the frequency characteristics of the source laser. Strain and temperature changes alter the Rayleigh backscatter spectrum [15]. Similarly to interferometric methods, spectral analysis can be conducted in a distributed fashion by using the random scattering sources that naturally exist within optical fibers, or discrete scatters can be placed in a fiber. A discrete scatterer that is used for spectral analysis is called a fiber Bragg grating (FBG) [16]. Rayleigh scattering can be advantageous because it has the highest power of all the scattering mechanisms, allowing for high sensitivity and long measurement distances.

2.1.3 General DFOS Concept

Figure 2.6 shows the general DFOS concept. Light originating from an interrogator unit (IU), sometimes also called an analyzer, is launched into an optical fiber. The light then propagates along the fiber with some of its energy being backscattered from all locations. A subset of the backscattered light originating from a specific location along the fiber is then captured back at the IU and analyzed for its properties. Properties may include its frequency content, amplitude, phase or polarization.

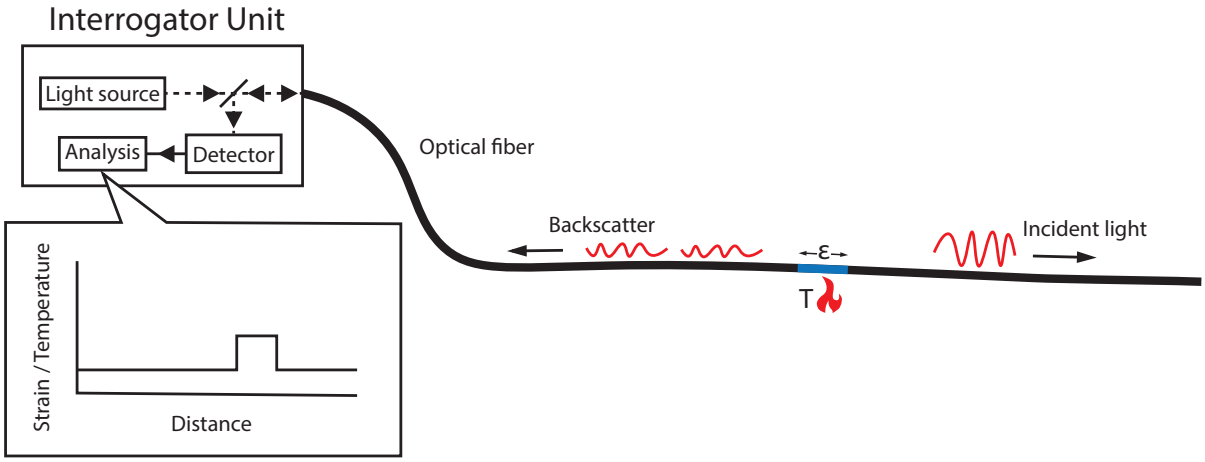

Figure 2.6: Descriptive diagram of the general DFOS technique (after [17]).

The specific position of where in the fiber the light backscattered from is determined by:

$$z = \frac{\mathbf{c}\Delta t}{2n} \tag{2.5}$$

where $\mathbf{c}$ is the velocity of light in free space, Δt is the time elapsed between launch and detection and n is the average refractive index of the fiber. The factor of $\frac{1}{2}$ is because the light needs to travel in both directions to complete a round-trip back to the IU. Equation 2.5 is useful when the light source is pulsed and analysis is conducted in the time-domain, which allows Δt to be a measurable quantity. If the analysis is done in the frequency domain using a continuous laser source of variable frequency, the relationship is [18]:

$$z = f_b \frac{\mathbf{c}}{\beta 2n} \tag{2.6}$$

where f_b is the beat frequency of the light interference at the detector, and β is the laser tuning rate. Equations 2.5 and 2.6 describe the spatial mapping schemes for the two main platforms of DFOS systems, optical time-domain reflectometers and optical frequency-domain reflectometers, respectively.

After the origin of the detected signal is mapped back to the fiber location where it came from and analysed for its measurement quantity by examining some characteristic of the backscatter (i.e. the frequency, amplitude, phase or polarization), the result is a spatial profile of that measurement. Due to the need to digitize the measurement process, each measurement is made at specific sampling locations along the fiber, each with a length of fiber influencing that measurement. Two important parameters for DFOS systems are the sampling interval and the spatial resolution that determine the characteristics of the spatial measurement profiles.

2.1.4 Sampling Interval versus Spatial Resolution

Figure 2.7 generally shows the relationship between a DFOS system's sampling interval and spatial resolution. The spatial resolution of a DFOS system describes the length of fiber that influences a single measurement point. It can be determined by different factors depending on the optical technique employed. For time-domain reflectometry methods, the spatial resolution is typically determined by the light pulse shape and size, and the gauge length if one is used [19–21]. The spatial resolution for frequency-domain reflectometry is determined by the frequency span and linearity of a tunable laser source [22].

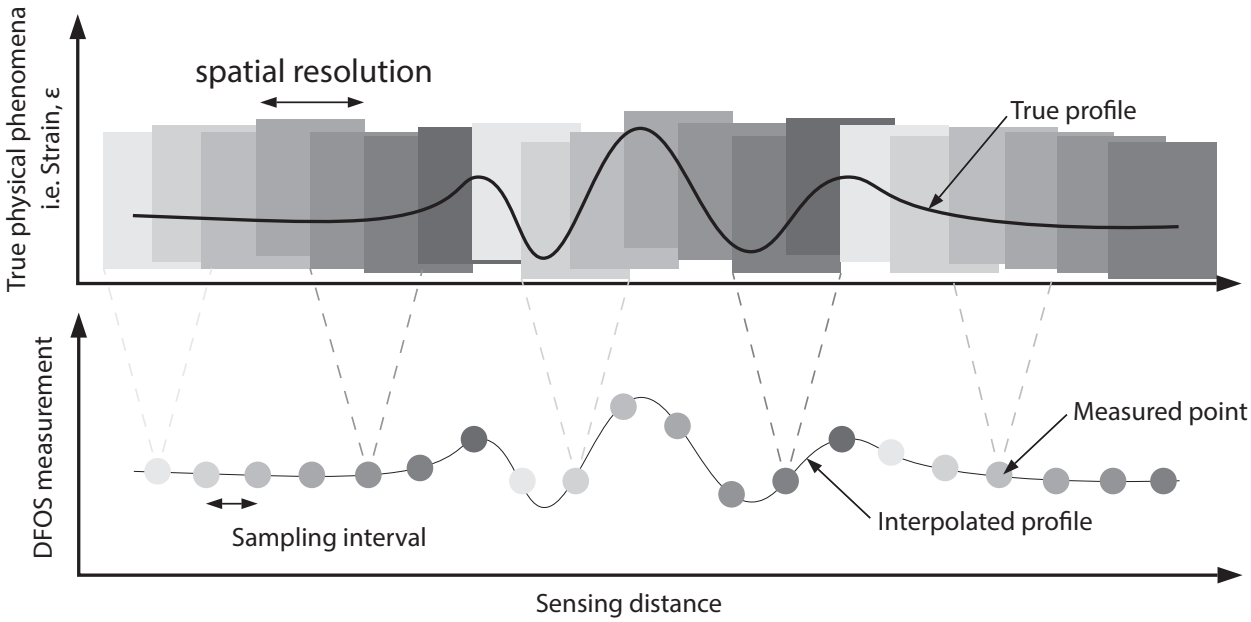

Figure 2.7: The principles of spatial resolution and sampling interval after [4].

The sampling interval of a DFOS system goes by many different names, including channel spacing, trace separation, readout interval and gauge pitch. These terms all refer to the spacing between registered measurement points which are located at the center of a given spatial resolution span. The sampling interval is determined by the digitization rate of the signal, since points at the detector map to points in space along the fiber. In DFOS, the sampling interval is equal-to or less-than the spatial resolution, so that information is acquired over the entire fiber length. Depending on the application, the sampling interval may be desired to be dense enough to sufficiently interpolate a spatially continuous signal according to the Nyquist-Shannon sampling theorem [23]. This technique is demonstrated in Chapter 3.

2.2 DFOS Techniques for Dynamic Strain Sensing

The primary applications of DFOS within engineering have been for monitoring strain and temperature. Strain is the main focus of this dissertation, and particularly dynamic strain. Dynamic strain can be defined as a measure of successive strain-change from a reference state. In order to measure dynamic strain effectively, the measurements must be sampled at sufficiently high rates to capture the behavior of interest. The necessary acquisition rate may

vary from one acquisition to another. In Chapter 3, the needed acquisition rate for capturing strain waves is several hundreds of Hz, however for the applications in Chapters 4 and 5 tens of Hz may be sufficient. The dynamic requirements significantly reduce the number of DFOS technologies that can be applied. For example, Brillouin optical time-domain reflectometry can measure the absolute strain in an optical fiber based on physical fundamentals of how the light field interacts with the vibrational characteristics of the glass matrix. However, because of the weak scattering power many measurements must be averaged together, making measurement times are on the order of minutes [4]. Therefore, this technology is usually not viable for dynamic strain monitoring unless some advancements are made [24]. In this section, the general techniques that are used for dynamic, distributed fiber optic sensing (DDFOS) are presented, and then applications within civil engineering are discussed.

2.2.1 OTDR-based Techniques

Optical time-domain reflectometry (OTDR) is performed by a device that examines the intensity of Rayleigh backscatter that occurs when pulses of light are injected into a fiber. It was shown by Barnoski and Jensen, and Personick [25, 26] that Rayleigh backscatter could be mapped to its origin location within the fiber and its relative power change over a fiber's length is proportional to signal attenuation. The concept was also demonstrated as being able to detect discrete reflection locations along a fiber that are indicative of damage. Notably, this OTDR technology employed lasers with short coherent lengths, so destructive interference of backscatter corrupting the signal was not an issue. Now, OTDR is ubiquitous in the telecommunications industry and an important tool for all fiber optic technicians and practitioners.

Figure 2.8 shows a typical OTDR trace that may be obtained from inspecting a fiber in the field. OTDR quantifies and maps power loss associated with obstructions such as splices and connectors to their locations along a fiber. They also capture the attenuation characteristics that may vary from one section of a link to another based on the design of different fibers, bend radii or damage. For the interested reader, Figure 2.8 also shows the proper termination of a fiber for sensing applications, which is to eliminate end reflections by adding some type of attenuator.

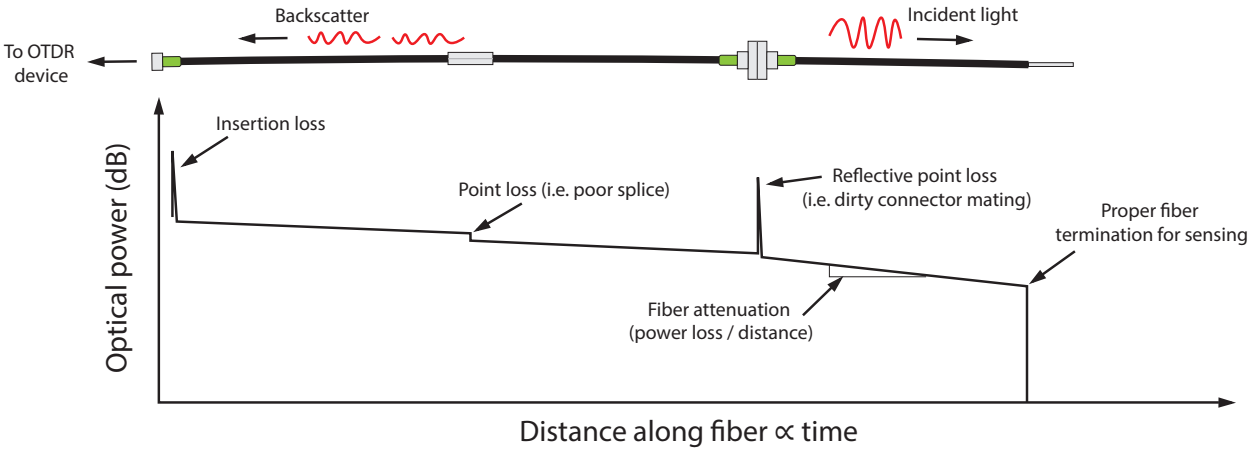

Figure 2.8: Schematic diagram of an example OTDR trace for fiber integrity checking and common sources of loss after [11].

OTDR measurements and their time scales

Since OTDR maps the signal returning from a scattered light pulse to a location along a fiber, for repetitive measurements to be made the data must be reorganized to describe the measurements in both location along the fiber and in time. Figure 2.9 demonstrates this process, which is also crucial for how the data in many sensing systems is processed. Figure 2.9 (top) shows the light pulse power that is injected into a fiber with time. The pulses are rectangular in envelope in this idealized example and are separated in time by $\frac{1}{f_p}$. The total length of the fiber under test (FUT) z_{fut} must be related to f_p by:

$$f_p \leq \frac{\mathbf{c}}{2nz_{fut}} \tag{2.7}$$

which is a variation of Equation 2.5. Equation 2.7 ensures that there is only one light pulse occupying the fiber at any given time. The center of Figure 2.9 shows a repetitive OTDR signal that repeats with frequency f_p, and is digitized at frequency f_s. Therefore, the trace repeats at exactly every f_s/f_p samples. The data can be sliced every f_s/f_p and stacked along a new discrete dimension, labeled as k in Figure 2.9. The result is data that is sampled at two different timescales; along the j axis it is sampled at f_s and along the k axis it is sampled at f_p. Generally speaking, $f_s >> f_p$ and these axes can be referred to as the fast and slow axes, respectively [27].

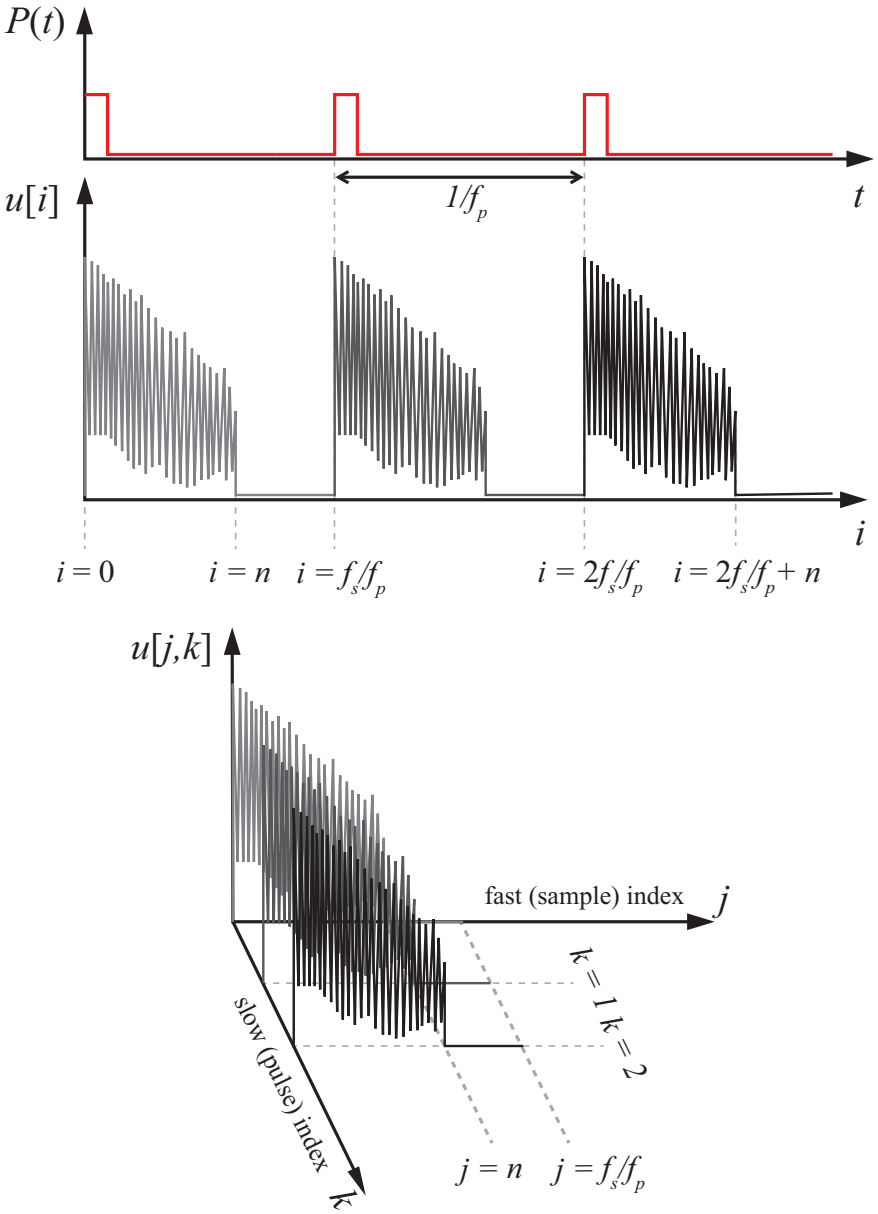

Figure 2.9: Demonstration of the different time scales at work in OTDR systems after [27].

OTDR strain sensing techniques using Rayleigh scattering

Leveraging OTDR for sensing requires examining some change that can be associated with a physical phenomena of interest. In the case of Rayleigh based OTDR these changes can be phase, amplitude, spectral power or polarization. This dissertation focuses on the use of Rayleigh backscatter's phase for detecting deformations. This will be elaborated specifically

in Section 2.3.

The amplitude of Rayleigh backscatter detected with OTDR can be modulated for sensing by changing the fiber geometry or by interfering separate coherent light beams. Fiber geometry can be changed by imparting deformation to a fiber in a known fashion, such as through a special constrictive/dilative coating or a microbend. Such techniques may be used for pressure or chemical sensing [28].

Similarly, the polarization of Rayleigh backscatter has sensitivity to bending, magnetic fields and pressure. Techniques have been developed based on OTDR that examine the changes in state of polarization (SOP) along a fiber's length to localize perturbations [29].

It has also been shown that when pulses of various frequency are injected into a sensing fiber, the shift in power spectrum of each scattering location along a fiber can be measured. This Rayleigh backscatter spectrum shifts linearly with strain and temperature, so they can be cross-correlated to resolve measurement values [30, 31]. This is the time-domain manifestation of OFDR, which will be discussed later in this literature review.

OTDR sensing techniques using Brillouin and Raman scattering

The OTDR technique can be used in a similar fashion for Brillouin and Raman scattering as it is for Rayleigh scattering. Brillouin-OTDRs and Raman-OTDRs are used to examine the fundamental changes in inelastic scattering that was presented in Figure 2.5. Raman-OTDRs are a common configuration for DTS systems and Brillouin-OTDRs are common implementations of DSTS [4, 32].

2.2.2 OFDR-based Techniques

OFDR was initially developed as an improvement on Rayleigh-based OTDR for inspection of fiber links that eliminated the need for creating short light pulses and digitizing at very fast rates [22]. The main difference between OTDR and OFDR is that the backscattered signal is digitized in the frequency domain rather than the time domain. This is done by applying variable frequency filters to the analog signal before digitization and recording samples of intensity versus frequency [33].

Rayleigh-based sensing using OFDR

Rayleigh OFDR will be used later in this dissertation as a verification tool for ϕ-OTDR measurements, so the technique is of particular interest to introduce. The Rayleigh OFDR technique for measuring strain and temperature was first proposed by Froggatt and Moore [15] and has had widespread success in commercial implementations. The technique relies on the randomness of Rayleigh backscatter along a fiber that can be modeled as a probe of random fluctuations in the permittivity of a fiber. As the random fluctuations are stretched or compressed through mechanical strain, temperature change or pressure, the frequencies of incident light that would produce a certain intensity of Rayleigh backscatter changes. In

fact, the power of backscatter at all frequencies reflected by the random field shift linearly in frequency with strain and temperature. This is similar to the concept of an FBG but distributed along a fiber with random periods [34]. In order to determine this shift, the different frequencies need to be individually probed since Rayleigh backscatter only occurs at the incident light wavelength (see Figure 2.5).

Rather than the finite pulses required in OTDR, a swept frequency continuous beam is sent down the fiber and the backscatter is recombined with a reference beam at a detector. The combination forms a beat frequency f_b that varies with backscatter origin position. This process simultaneously probes the different Rayleigh backscatter frequencies and down converts the signal to a smaller bandwidth for analysis [22]. After digitization in the frequency domain, the signal is converted to a spatial profile through time's proportionality to space and an inverse Fourier transform. This technique allows for the sampling interval of the fiber to be a function of the total band of laser wavelengths sampled, rather than the sampling directly along the 'fast axis' in OTDR. The sampling interval Δz is defined as[15]:

$$\Delta z = \frac{\pi}{2n\Delta k} \tag{2.8}$$

and similarly the maximum sensing distance z_{max} is defined as:

$$z_{max} = \frac{\pi}{2n\delta k} \tag{2.9}$$

where Δk is the continuous range of wavenumbers produced by the laser and δk is the wavenumber step size digitized by the system. After transforming the signal from the wavenumber domain to the space domain, subsets of the spatial signal centered at each sampling location are selected. A discrete frequency domain cross-correlation is preformed for each subset of samples to determine the spectral shift, and in turn the strain and temperature change. The maximum range of strain or temperature measurements is proportional to the tuning range of the laser. There is a cross-coupling between the spatial resolution z_{res} and strain resolution ε_{res} of these OFDR systems, described by [15] as:

$$z_{res}\varepsilon_{res} = \frac{\Lambda_{max}}{4n} \tag{2.10}$$

where Λ_{max} is the maximum wavelength injected by the tunable laser source. The spatial resolution is therefore determined by the length of the cross-correlated subset of signal in the space domain and is inversely proportional to the strain resolution of the instrument. The main challenge of Rayleigh OFDR is spatial range, limitation on strain resolution and range of strain measurements, which all depend on the performance of the tunable laser source.

Brillouin and Raman-based sensing using OFDR

OFDR techniques have been used with both Brillouin and Raman scattering for measurement of strain and temperature [35, 36]. Unlike the Rayleigh-based technique, OFDR using

inelastic scattering is done incoherently. This technique may be referred to as incoherent optical frequency-domain reflectometry (IOFDR) [37]. The difference is that the probing signal is modulated in amplitude rather than being tuned in frequency [38]. The main defining principle is the same as Rayleigh OFDR, though. The signal is measured in the frequency domain and then an inverse Fourier transform maps the measurements to the physical phenomena in space along the fiber. In the case of Raman scattering, the spectral power at the Stokes and anti-Stokes frequencies are mapped to the fiber and the relationship between them can used to determine the temperature [39]. For Brillouin scattering, OFDR maps the spectra of the Stokes or anti-Stokes components to the distance along the fiber, and the peak power is used to determine the strain and/or temperature change [35].

2.2.3 Other DFOS Techniques

OTDR and OFDR are the main platforms of DFOS. There are, however, techniques that do not fall within these families. Examples include optical coherence-domain reflectometry (OCDR) [40], Brillouin optical correlation-domain reflectometry (BOCDR) [41], Brillouin optical correlation-domain analysis (BOCDA) and Brillouin optical time domain analysis (BOTDA) [42]. The latter three are specific to Brillouin scattering, while OCDR uses Rayleigh scattering. There are many variations of DFOS technologies being published fairly constantly due to the rich research culture on both the developmental and application sides of DFOS. Readers are recommended to explore recent review papers and comprehensive books on the topic of DFOS to learn more about the latest technologies [4, 11, 18, 43].

2.2.4 Applications within Civil Engineering

In this section we summarize the DDFOS technologies that appear in the literature for monitoring strain in civil infrastructure systems including Rayleigh- and Brillouin-based sensing. The purpose of this review is to demonstrate the current capabilities of DDFOS that are used in civil engineering, highlight the current limitations of these technologies and the improvements that would be beneficial to the field.

Brillouin-based techniques

Brillouin-based DDFOS for strain monitoring has been developed based on various techniques including BOCDA [44], BOTDA [45] and BOTDR [46]. Each of these techniques aim to determine the Brillouin frequency spectrum along a length of fiber and how it changes with time. Fundamentally, it has been noted that the Brillouin frequency spectrum shifts when subject to strain at a factor of $\sim$50kHz/$\mu\varepsilon$ and it has an intrinsic width of $\sim$30 MHz [47]. This makes resolving small measurements difficult. Brillouin-based DDFOS techniques have achieved measurement precision as high as $\pm$0.5 MHz or 10 $\mu\varepsilon$, though raw data processing was not done in real-time to achieve this performance [48].

Brillouin-based DDFOS methods have been validated for structural health monitoring applications in laboratory and field settings. Oskoui et al. [49] employed a BOTDA-based technique for dynamically monitoring two multi-span bridges. The technology was able to detect cracks based on a normalized crack index method. The strain measurement precision was not discussed though cited publications about the same technique report precision of 40 $\mu\varepsilon$ [50]. Scarella et al. [51] used the same technology for a laboratory assessment of monitoring cables for cable-stayed bridges. It was noted that strain resolution was a major limitation in the testing that caused some of the damage test cases to be undetectable.

In another research group, Minardo et al. [35] and Coscetta et al. [52] used a BOTDA-based technology for monitoring a cantilever beam and wind turbine blades under dynamic loading. The technique was effective for high-amplitude vibration at rather low frequencies. Minardo et al. noted that the technique could resolve the first mode of vibration of the cantilever beam but higher modes were difficult due to the sampling rate of 18 Hz. Coscetta et al. employed a sampling rate of 15 Hz. It was noted that the acquisition rate was limited by the time the system took to average several measurements, which is common in Brillouin-based technologies due to low SNR.

Overall the application of Brillouin-based technologies has been limited in dynamic structural health monitoring so far. It has been clear, though, that the main limitations of the technology are strain measurement precision and acquisition rate. Both of these challenges can be directly attributed to the weak nature and spectral broadness of Brillouin scattering.

Rayleigh-based techniques

Rayleigh-based DDFOS use in civil engineering has focused on OFDR technologies, and has been evaluated for monitoring dynamic behavior of infrastructure in the lab and field. Wheeler et al. evaluated a commercial OFDR system for its ability to detect dynamic strains in rail infrastructure associated with passing trains [53, 54]. Later, Broth and Hoult [55] examined the same system for detecting damage in concrete beams. Similar investigations were carried out by Reiger and Hoult and Henault et al. [56, 57].

The technology used in these studies was commercialized by Luna Innovations Inc. as their ODiSI line of distributed strain and temperature sensing systems [58, 59]. It was clear in these studies that the OFDR suffered from limited temporal sampling frequency, spatial range and strain precision. Wheeler et al. [53] noted that under ideal conditions the commercial OFDR system used could potentially achieve 50 Hz sampling rate and a $\pm$ 10 $\mu\varepsilon$ precision. The specific sampling rate used was not indicated however a strain precision of $\pm$ 25 $\mu\varepsilon$ was observed. Reiger and Hoult [56] noted that the ODiSI-B used in their study could achieve 250 Hz for a 2 m-length of fiber, or 100 Hz for a 10 m-length with a strain precision of $\pm$ 1 $\mu\varepsilon$. They noted that the system did not perform up to this strain precision, though. The lastest Luna Innovations OFDR system (ODiSI-6xxx series) is used in Chapters 4 and 5 as a verification tool for ϕ-OTDR and reports a maximum measurement distance of 100 m, a strain precision of 2-5 $\mu\varepsilon$ and sampling rates inversely related to sensing distance of 1-250 Hz [60].

It has begun to be noticed that more precision, longer ranges and higher acquisition rates for DDFOS may be attainable with Rayleigh OTDR-based techniques. Though prior to this dissertation this research has existed at the developmental level, largely outside of the civil engineering domain. For example, Liehr et al. [30] showed that a novel technique blends the favorable attributes of OFDR and OTDR systems to achieve sensitivity as low as 47.5 $p\varepsilon$ with sampling rates in the kHz range and spatial resolutions in the meter range. However it is limited to relatively short fibers due to the exceptionally high pulse rates used (see Equation 2.7.

This dissertation seeks to improve on the DDFOS capabilities currently deployed in civil engineering by exploring the capability of a revolutionary new technique, ϕ-OTDR. ϕ-OTDR has been developed over the last three decades and increases the precision of fiber optic strain measurements by making them on the size order of the wavelength of light [61]. This is done through optical interferometry that can determine extremely small changes in fiber length over distances only governed by the power of the backscatter and the ability to detect it (often in excess of 100 km). ϕ-OTDR measurements are made extremeley rapidly, allowing for measurement rates to approach the maximum theoretical pulse rate of DFOS systems described in Equation 2.7.

ϕ-OTDR may also be referred to as DAS or DVS, which actually defines a group of technologies that ϕ-OTDR belongs to. To provide an adequate review of the development of ϕ-OTDR, the group of DAS/DVS technologies and their collective development is discussed next.

2.3 DAS/DVS Technologies

This section presents a summary of the basic physical phenomena that are used to make DAS/DVS measurements. Then, several typical DAS/DVS system configurations are presented to demonstrate how the measurements are made in practice. The distinction between quantitative ϕ-OTDR and qualitative C-OTDR is explained using a laboratory bench-top DAS/DVS setup in a configuration where both measurement types are possible. Finally, conversion of ϕ-OTDR measurements to physical units and considerations for interpreting these data are discussed.

2.3.1 Optical Interferometry

DAS/DVS uses coherent Rayleigh scattering within single mode optical fibers to detect changes in relative phase of the light over a length of fiber. These relative measurements are the result of interferometry. Interferometry using light waves is an extraordinarily sensitive measurement technique that is behind many of the most sensitive instruments in the world. For example, the Laser Interferometer Gravitational-Wave Observatory (LIGO) uses this technique to measure distances $1/10{,}000^{\text{th}}$ the width of a proton caused by gravity waves

originating from across the universe [62]. It relies on constructive and destructive interference of light waves to determine a change in optical path length (OPL).

An example of a classic interferometer is the Michelson interferometer shown in Figure 2.10a. The light path, shown by the red arrows originates at the laser, then it encounters a beam splitter where portions of it are directed to two different mirrors. The light then reflects off of the mirrors and is recombined and directed to a detector. The detector would measure an oscillating field intensity with displacement of one of the interferometer's mirrors, as shown in Figure 2.10b.

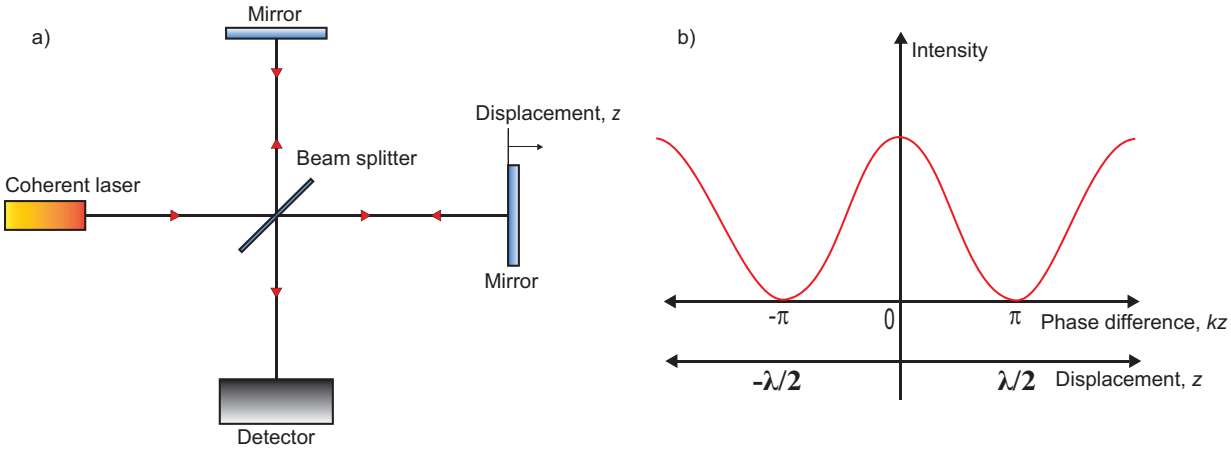

Figure 2.10: Schematic of a Michelson interferometer and the response of the combined field irradiance to changing the optical path length.

The electric field that the detector experiences can be described by:

$$\mathbf{E_t} = \mathbf{E_1} + \mathbf{E_2} = E_1 \cos(\omega t - kz_1) + E_2 \cos(\omega t - kz_2) \tag{2.11}$$

where E_t is the total time varying electric field, E_1 and E_2 are the magnitudes of the portions of light after splitting, z_1 and z_2 are the path lengths and k is the wavenumber. A detector, like the human eye measures the time-average of the squared field, also called the irradiance ($\mathcal{I}$). In the case of the waves interfering in a homogenous dielectric the irradiance can be described as:

$$\mathcal{I} = \epsilon v < (\mathbf{E_1} + \mathbf{E_2})^2 > \tag{2.12}$$

where $< \mathbf{E} >$ denotes the time average of $\mathbf{E}$, ϵ is the permittivity of the dielectric and v is the velocity of the waves. It can be then written as a summation of the two field's irradiances and a cross-term, as:

$$\mathcal{I} = \epsilon v(< \mathbf{E_1}^2 > + < \mathbf{E_2}^2 > + 2 < \mathbf{E_1 E_2} >) = \mathcal{I}_1 + \mathcal{I}_2 + 2\epsilon v\sqrt{\mathcal{I}_1 \mathcal{I}_2}\cos(k(z_2 - z_1)) \tag{2.13}$$

The irradiance is therefore a function of the phase difference between the wavefields. In the case described in equations 2.11 - 2.13 the phase difference is due to a change in path length which is determined by the position of the mirror in Figure 2.10a. Since the electric fields are periodic in z, the resulting field combination will vary depending on the two path lengths.

DAS/DVS systems use the Rayleigh scattering within single mode optical fibers to perform interferometry much like the technique described in this section. The displacement of the mirror in Figure 2.10 is replaced by an increase in path length between centers of Rayleigh scattering. These scattering centers, which are distributed along an optical fiber act as at least one of the mirrors in the interferometer. The difference between qualitative (C-OTDR) and quantitative (ϕ-OTDR) is whether or not the phase behavior analogous to the moving mirror in Figure 2.10 can be determined and therefore the displacement can be calculated.

2.3.2 DAS/DVS System Architectures

As DAS/DVS systems include implementations of technologies that are only able to detect disturbances qualitatively and the quantitative strain-measurement tools that are the primary focus of this dissertation. The former type of DAS/DVS systems are often referred to as intensity-only systems because they report a highly random intensity value of an interferometer response, neglecting the phase. Quantitative systems, also known as phase-sensitive DAS systems or differential-phase-measuring DVS systems [11] utilize the intensity and phase information of an interferometer in a more controlled configuration allowing for a linear sensor response to strain. This section will first present the older intensity-only system configuration, and then several embodiments of phase-sensitive systems.

Intentisty-only (C-OTDR) Systems

It was noticed that when a coherent light source was used in a conventional OTDR configuration the response of the instrument changed with acoustic waves experienced by the fiber [63]. This phenomena was described thoroughly by Juskaitis et al. [13]. The technique is referred to as coherent optical time-domain reflectometr (C-OTDR). Figure 2.11 shows this technique as descibed by Juskaitis et al. as an interferometer response of two random scattered fields originating from two halves of an incident pulse with a infinitely discrete disturbance happening between the halves.

The system uses A coherent laser beam that is modulated to create individual pulses which are then injected into a sensing fiber. The pulse interacts with the inhomogeneities that exist in the fiber and some of the energy is scattered as Rayleigh backscatter. The light returning to the detector can be described as an interference of light scattering from each half of the pulse. Figure 2.11 shows the two scattered fields from each half as originating from groups A and B of scatterers. The backscattered light then passes through a circulator, which directs the counter-propagating light towards the detector. The detector then measures the

combined field, and any changes in the combined field that occur due to disturbance in the scattering region. Some authors refer to the scattering region as a resolution cell [11].

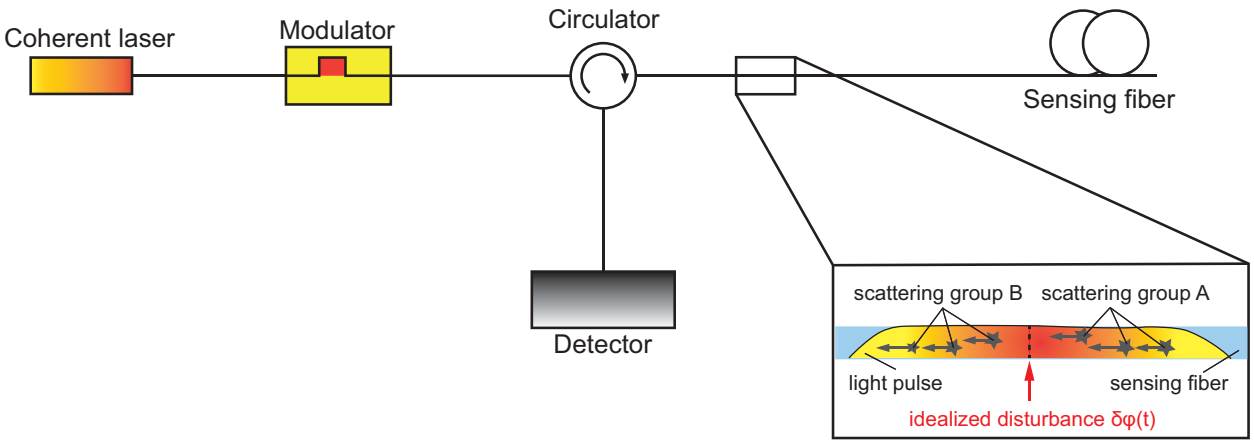

Figure 2.11: Schematic of a C-OTDR system as described by measuring the sum of two random scattering distributions caused by a single pulse with a idealized (infinitely local) disturbance happening between them.

The field received at the detector in this idealized case would be [13]:

$$\mathcal{I}(t) = |\mathbf{E_A}|^2 + |\mathbf{E_B}|^2 + 2|\mathbf{E_A}||\mathbf{E_B}|\cos(\phi_0 + 2\delta\phi(t)) \tag{2.14}$$

where $\mathbf{E_A}$ and $\mathbf{E_B}$ are the magnitudes of the electric fields scattered by each scattering group, ϕ_0 is the initial phase difference of the light coming from each group, and $2\delta\phi(t)$ is the total delay caused by phase disturbance $\delta\phi(t)$. For quantitative measurement this representation has two problems. First, ϕ_0 is unknown and can be any value from 0 to 2π. This would result in completely different interferometer responses depending on the initial phase offset. This principle is shown in Figure 2.12 for the same $\delta\phi(t)$ signal with different ϕ_0 values of zero and $\pi/2$. Figure 2.12 also assumes $\mathbf{E_A}$ and $\mathbf{E_B}$ have the same magnitude.

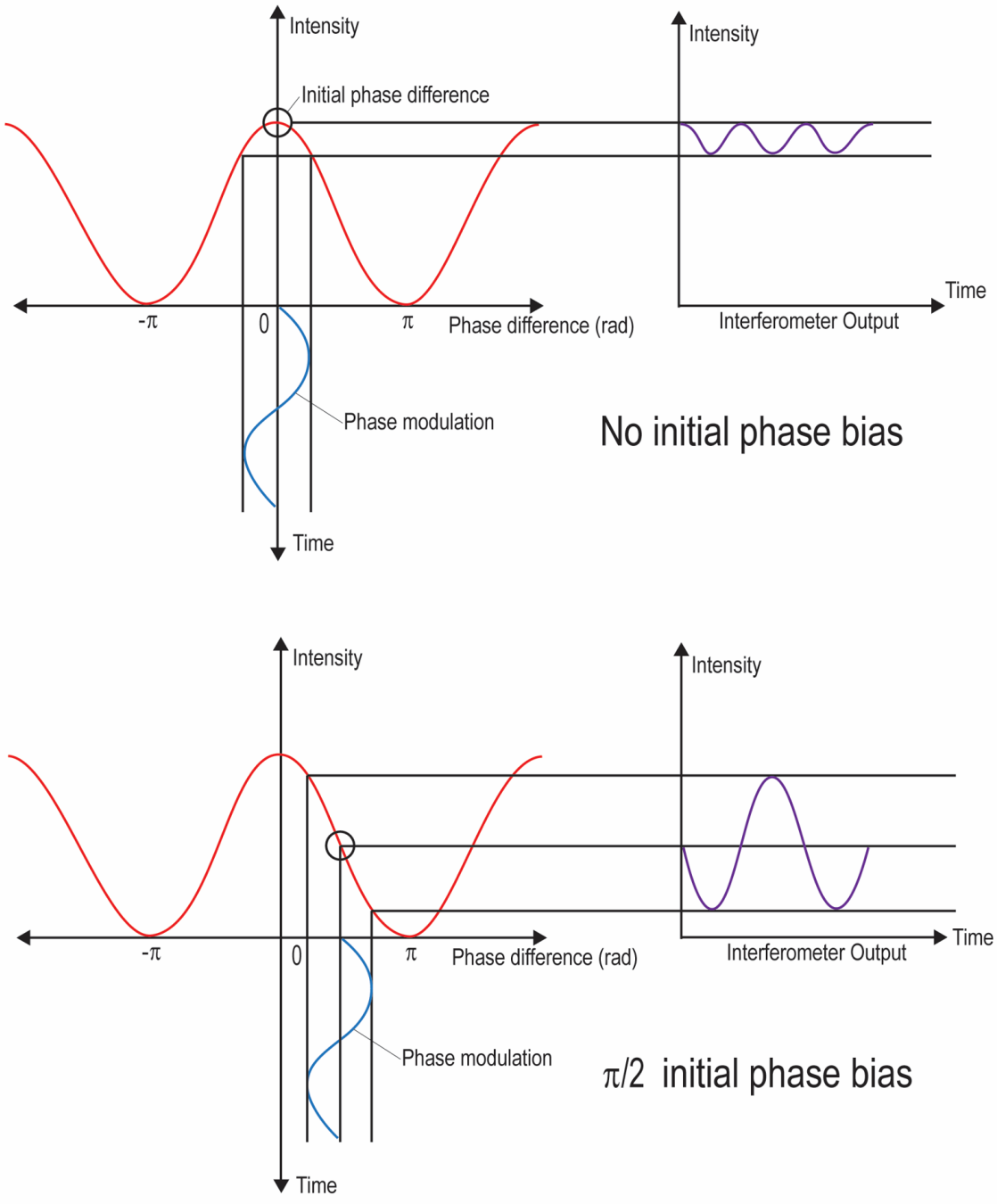

Figure 2.12: Interferometer responses of the idealized C-OTDR system for a single measurement point with different initial phase biases. This response assumes an infinitely discrete phase modulation and equal scattered field intensities.

The idealized C-OTDR measurements shown in Figure 2.12 have different magnitudes, frequency and phase with the same input signal. The second problem with the representation in Equation 2.14 is that it is impossible to have a perfectly discrete disturbance. In reality, strains are distributed over some length of fiber, further complicating the instrument response and making it even less suitable for quantitative strain measurement. Nonetheless, C-OTDR systems have seen widespread and commercial success, beginning with the patent by Taylor and Lee in 1993 [64].

ϕ-OTDR systems are related to C-OTDR in that they also implement a distributed interferometer along an optical fiber, but they do so in such a way that the response is linearized. These systems with a linear response to strain are the ϕ-OTDR systems that are the focus of this dissertation, and are detailed next.

Phase-Sensitive (ϕ-OTDR) Systems

The main advancements that ϕ-OTDR systems achieve over C-OTDR systems are that (1) the interferometer examines a length of fiber between specific backscattering locations and (2) the initial phase bias problem described by Figure 2.12 is solved through coherent detection of some kind. There are many embodiments of ϕ-OTDR systems. Several of the popular design platforms are presented here. A commercial dual-pulse system was used for the main work of this dissertation, however a heterodyne system was constructed in the laboratory due to its simplicity to understand the workings of ϕ-OTDR systems as part of this review.

Dual-Pulse Systems The dual-pulse ϕ-OTDR system was first proposed by Dakin and Lamb in a patent application in 1988 which was subsequently published in 1990 [65]. This type of system injects two pulses of slightly different frequencies, f_1 and f_2, into a sensing fiber. The pulses are separated in time (ΔT) by:

$$\Delta T = \frac{2gn}{c} \tag{2.15}$$

where g is the gauge length, or separation distance between the origins of scattered light from each pulse. This corresponds to the injected pulses being spaced at double the gauge length of the DAS system. The pulses scatter from locations along the sensing fiber and recombine in flight, resulting in a combined field from scattering that does not occur at the same time for each pulse. The leading pulse scatters first, and the trailing pulse travels $g/2$ in the forward direction before scattering and combining with the backscatter from the leading pulse.

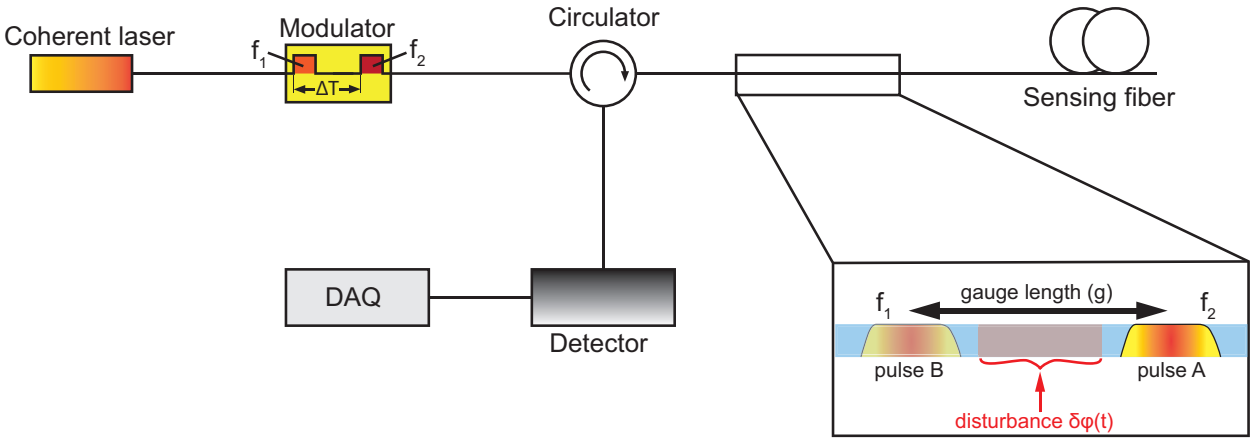

Figure 2.13: Schematic of a dual-pulse ϕ-OTDR system after [61, 65]

.

The combined field from two scattered pulses has a beat frequency that is a function of the frequency difference between the two pulses, and is phase modulated by any change change in light phase between the scattering centers. The causes of phase change, including strain will be discussed later. The combined field is given by:

$$\mathcal{I}(t) = |\mathbf{E_A}|^2 + |\mathbf{E_B}|^2 + 2|\mathbf{E_A}||\mathbf{E_B}|e^{j(2\pi[|f_1 - f_2|t + \delta\phi(t)] + \phi_A - \phi_B)} \tag{2.16}$$

where $\delta\phi(t)$ is the total change in phase that occurs between the scattering centers. Recovering the phase information from a dual-pulse systems can be done in a variety of ways. One such way is to perform I/Q demodulation on the sampled digital intensity data recorded from the detector as done in the realization of this technology patented by Lewis and Russell [66]. Another technique is to phase delay each trailing pulse such that the interference is sampled at several phase differences of the interferometer, allowing for the external perturbation to be recovered [67]. The commercial ϕ-OTDR IU employed in the body chapters of this dissertation uses the dual-pulse architecture. Patents that led to the commercialization of the technology include Russell, Hayward & Lewis (2008) [68], Lewis and Russell (2010) [66], and Lewis & Russell (2012) [69].

Imbalanced Mach-Zehnder Interferometer Systems An alternative method of examining the optical phase modulation of Rayleigh backscatter experienced by a fiber due to strain was proposed by Posey et al. [70]. This technique relies on an imbalanced Mach-Zehnder interferometer with the separation in light scatterer locations being determined by a delay loop. Figure 2.14 shows a schematic of this type of system. Unlike the dual-pulse system, only a single pulse is launched into the fiber at a time. The backscattered light from

that single pulse is combined with itself by splitting and delaying it. The delay loop length defines the gauge length of the system.

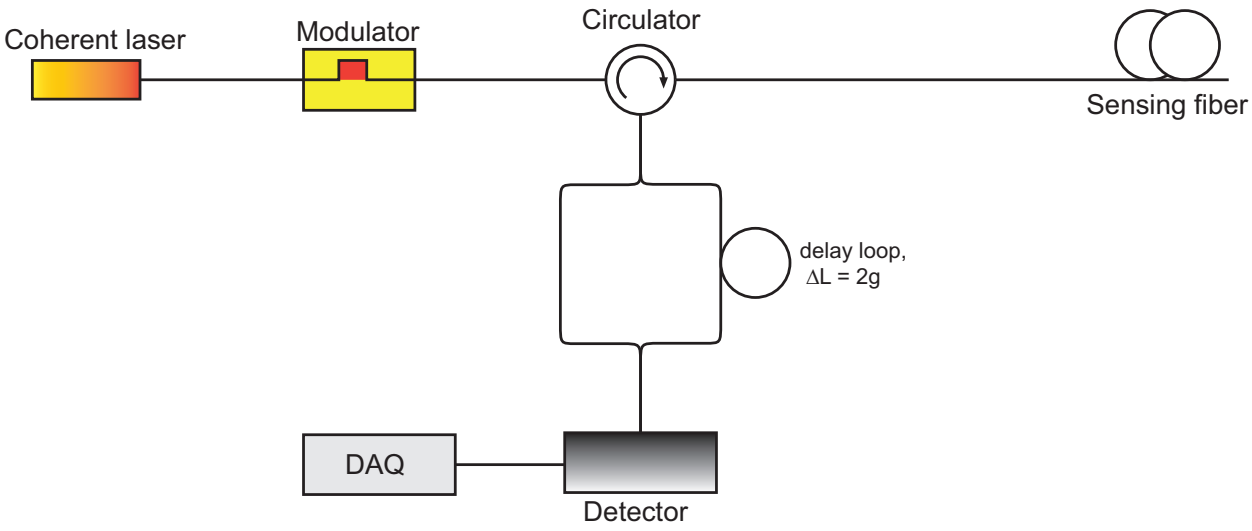

Figure 2.14: Schematic of an imbalanced Mach-Zehnder ϕ-OTDR system.

The detection process for Mach-Zehnder systems is typically conducted by an array of detectors that add phase shifts, since the signal does not have a carrier frequency. The combined field with no external shift added can be described by:

$$\mathcal{I}(t) = |\mathbf{E_A}|^2 + |\mathbf{E_B}|^2 + 2|\mathbf{E_A}||\mathbf{E_B}|e^{j(2\pi[\delta\phi(t)]+\phi_A-\phi_B)} \tag{2.17}$$

Since the external signal occurs at DC (i.e. there is no frequency term), additional phase shifts must be introduced to be able to solve for $\delta\phi(t)$. Posey et al. [70] and Masoudi et al. [71] did this using three detectors that imposed phase shifts of $\frac{-2\pi}{3}$, 0 and $\frac{2\pi}{3}$, respectively. These phase shifted outputs can be readily solved to determine $\delta\phi(t)$ [72].

Michelson Interferometer Systems A similar design to the Mach-Zehnder-based system is one based on a Michelson interferometer. In the Michelson interferometer-based system Faraday rotation mirrors are used to redirect the light towards the detector with an arm imbalance that defines the gauge length of the system. The use of Faraday rotation mirrors makes the system less susceptible to polarization fading, which is a degradation in the signal due to the interfering fields having orthogonal polarization states [73]. Figure 2.15 shows this type of system. Due to the robustness of the Michelson interferometer configuration, this setup has been described in several patents and is likely the platform for commercial instruments [74, 75].

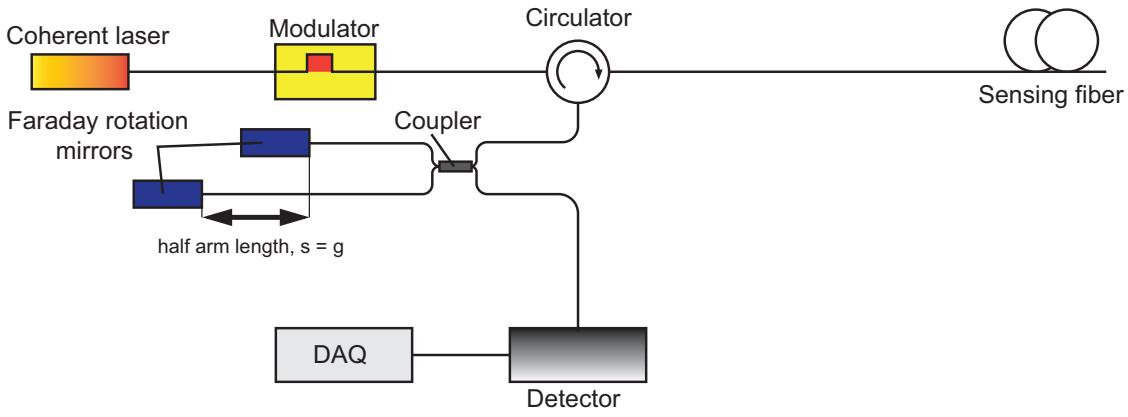

Figure 2.15: Schematic of an imbalanced Michelson Interferometer ϕ-OTDR system.

Alternatively, another modulator can be added to one of the interferometer paths in either the Michelson or Mach-Zehnder configurations to introduce a frequency difference similar to the dual-pulse configuration so only one detector is needed [76].

Heterodyne Systems Heterodyne systems digitize the phase difference between a frequency-shifted backscattered pulse and a local oscillator. The local oscillator is usually a split path from the source laser. The concept was patented by Hartog and Kader and is the basis of commercial instruments, most famously the Schlumberger hDVS which derives its name from the technique (heterodyne DVS). Figure 2.16 shows a schematic of this type of system.

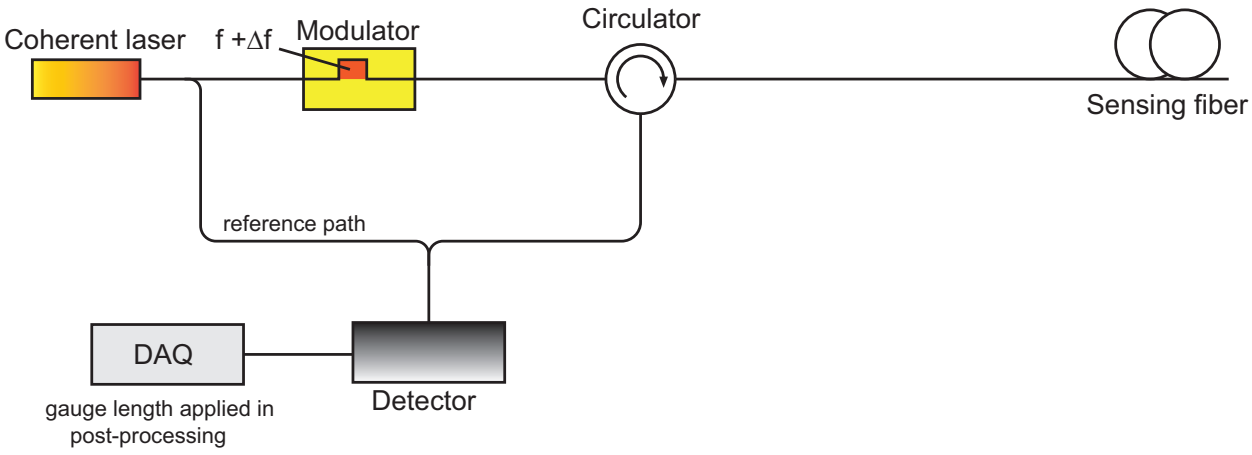

Figure 2.16: Schematic of a heterodyne ϕ-OTDR system.

The gauge length of heterodyne systems is determined in post-processing by taking the spatial derivative of the data. Since all phase measurements are made relative to a reference, the gauge length can be set arbitrarily. Due to the simplicity of the heterodyne system, a version was created in the laboratory to demonstrate the technique and the difference between ϕ-OTDR and C-OTDR measurements in practice.

Signal Fading and Diversity Processing in DAS/DVS systems Due to the randomness of Rayleigh backscatter, it is possible that one of the scattered electromagnetic fields that are used for the phase measurements is too weak to make a reliable interference pattern. As shown in Equations 2.16 and 2.17 that if either $|\mathbf{E_A}|$ or $|\mathbf{E_B}|$ are very small, the interference term will vanish. This is called signal fading. Fading can happen due to weak Rayleigh backscattering or because of changes in polarization state [77, 78]. To combat signal fading, many DAS/DVS system employ techniques that vary system parameters in order to reduce signal fading at any of the measurement locations. The most common forms of diversity processing are wavelength and spatial diversity. In wavelength diversity processing, a system would use several different wavelengths of lasers to preform the same measurements, and select the best result from the array of different lasers [79]. In spatial diversity processing, a system may examine a length of fiber for the best signals, and then perform some sort of spatial selection and weighting to provide a high SNR measurement to a user [80]. Understanding the diversity employed by a DAS/DVS system is important especially when the amplitude of strain measurements are desired. The commercial system employed in the body chapters (Optasense ODH-4) performs wavelength diversity processing across four different laser wavelengths to reduce signal fading.

2.3.3 Laboratory DAS/DVS Construction and Demonstration

A heterodyne-based DAS/DVS system was constructed in the laboratory for the purpose of understanding the architectures published in the literature and explore the difference between ϕ-OTDR and C-OTDR systems. The detailed schematic of the system and a photo of the optical components are shown in Figure 2.17.

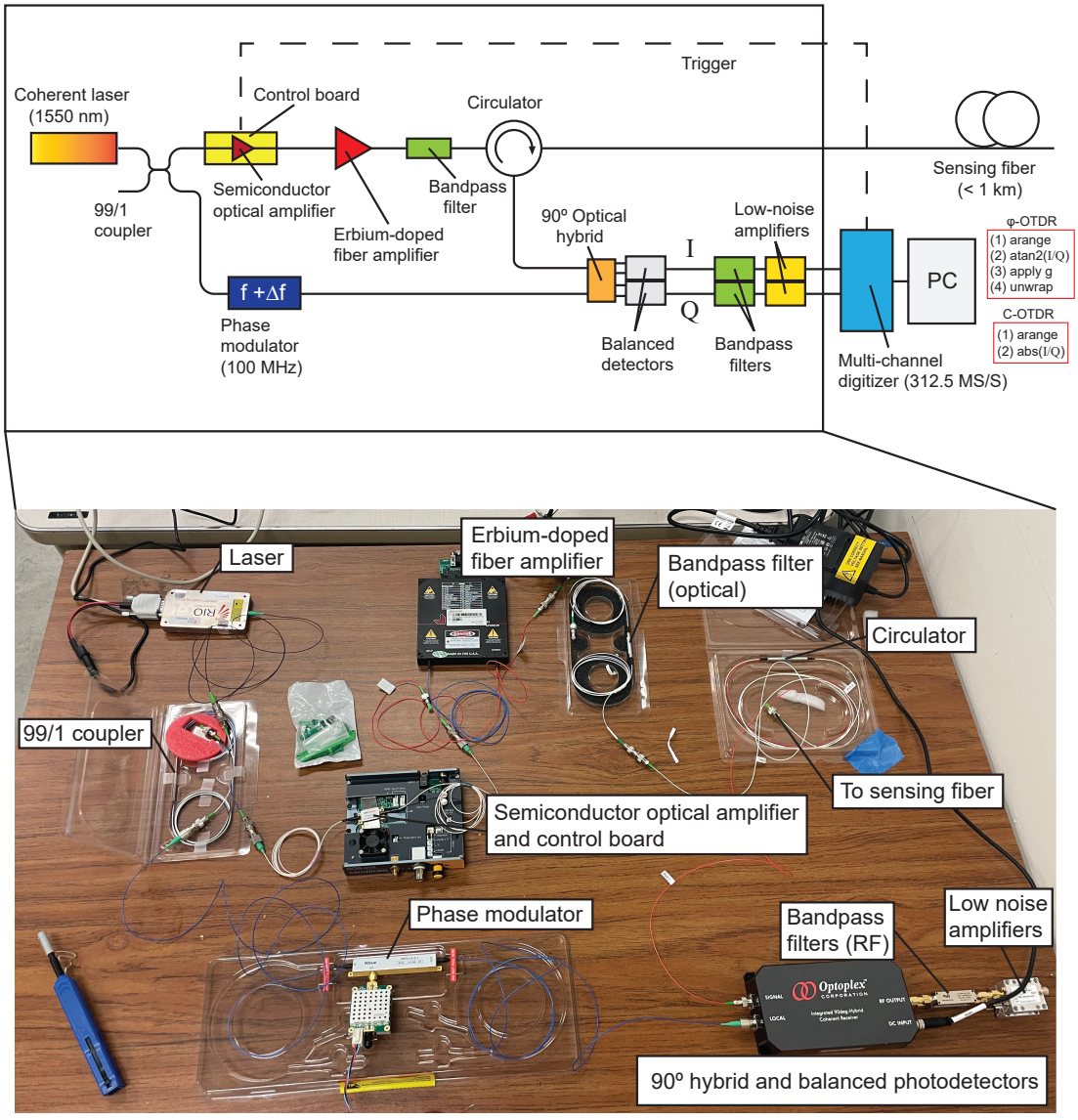

Figure 2.17: Heterodyne ϕ-OTDR system constructed in laboratory.

The system used a highly coherent, narrow-linewidth 1550 nm semiconductor laser to create both the source signal and local oscillator. The source laser beam was split using a 99/1 fiber coupler. The 99% arm of the coupler fed a simiconductor optical amplifier (SOA) that modulated the signal into 50 ns-wide approximately rectangular pulses at a repetition rate of 100 kHz. The pulses then passed through an Erbium-doped fiber amplifier (EDFA) and bandpass filter to reduce the spontaneous-emission noise from the EDFA before being launched into the sensing fiber.

The signal in the reference arm of the interferometer was phase modulated by a constant 100 MHz signal. The backscatter from the sensing fiber and the reference arm both entered a 90° optical hybrid and pair of balanced detectors to fully resolve four-quadrant phase though I-Q demodulation, or intensity though summing the absolute values of the I and Q components. The I and Q signals passed through narrow 100 MHz-centered bandpass filters and low-noise amplifiers before being separately digitized at 312.5 MS/S (million samples per second). The digital data was then sent in a block to the PC which arranged the data into complex phasors with I and Q components and also organized the data according to the fast and slow axes (see Figure 2.9).

For the ϕ-OTDR configuration The PC then was used to compute the 4-quadrant arctangent (denoted atan2 in Figure 2.17) and apply the gauge length. To apply the gauge length the phase measurements were differenced based on their delayed arrival to the detector and the phase was unwrapped. The delay time to the detector is also described by Equation 2.15 where ΔT is now the time over which the phase difference is taken, rather then the time difference between two pulses in a dual-pulse system. The four-quadrant arctangent and the unwrapping were performed using MATLAB's 'angle' and 'unwrap' functions on the resulting phasors, respectively [81]. For the C-OTDR configuration the magnitude of the complex phasors was taken with no application of gauge length.

The system and processing flow were tested using a sub-woofer to create pressure waves at 40 Hz. The sub-woofer tone was created directly towards a coil with 1 km of optical fiber being interrogated by the heterodyne system. The data was simultaneously used for both ϕ-OTDR and C-OTDR. The test configuration and resulting ϕ-OTDR data from when a 40 Hz tone was played are shown in Figure 2.18. The ϕ-OTDR employed a 32 m gauge length and the trace shown is centered 160 m into the sensing fiber.

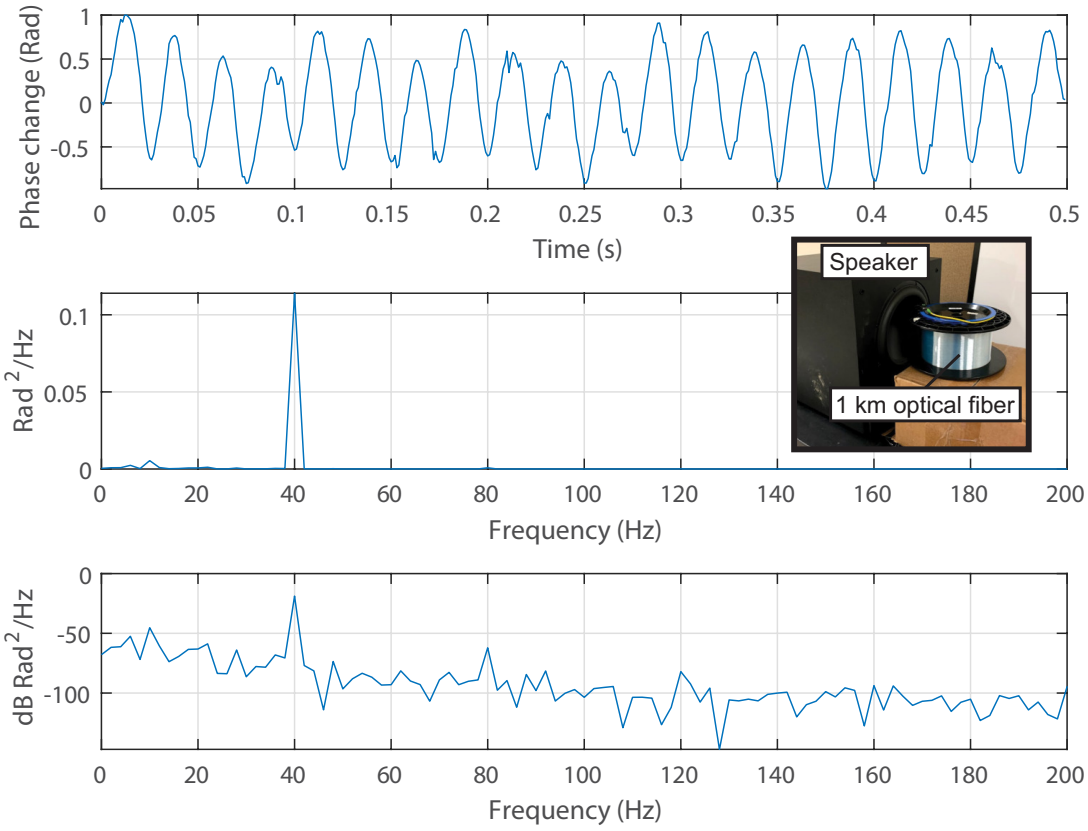

Figure 2.18: Example ϕ-OTDR data acquired from laboratory heterodyne setup when subject to a 40 Hz acoustic signal produced by a sub-woofer.

The corresponsing C-OTDR data is shown in Figure 2.19. It is clear that the C-OTDR data does not capture the waveforms of the input signal effectively. In fact, even the power spectra cannot identify the predominant input frequency. An overtone at 52 Hz appears to be the highest signal power captured and might be identified as the input signal by a user. However the 52 Hz signal is a result of the large phase change wrapping the interferometer response as shown in Figure 2.12.

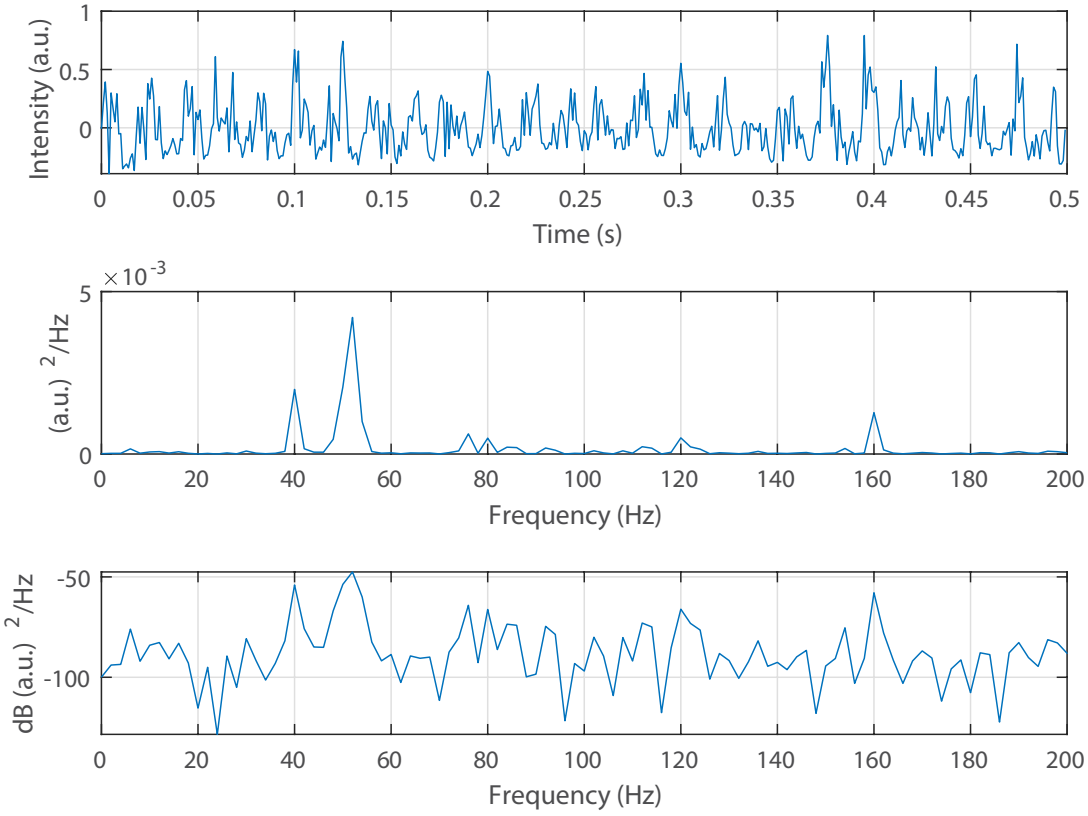

Figure 2.19: Example C-OTDR data acquired from laboratory heterodyne setup when subject to a 40 Hz acoustic signal produced by a sub-woofer.

The reason that the signal from the sub-woofer works so effectively at modulating the phase of the interferometer signal is because the fiber is very sensitive to pressure, which causes a mechanical strain. Bucaro and Hickman [82] tested the sensitivities of different fibers to acoustic pressure. For a coated-fiber similar to the fiber used in the lab experiment, the expected relative phase change with pressure (ψ) can be expressed as:

$$\psi = \frac{d\phi}{\phi \Delta P} \approx 5 \times 10^{-12} \frac{1}{\text{dyn/cm}^2} \tag{2.18}$$

The light phase over a gauge length of fiber accounts for two-way transit as [19]:

$$\phi = 2nkg = \frac{4\pi n g}{\lambda} \tag{2.19}$$

Therefore the pressure signal can be calculated using the amplitude of the phase change in Figure 2.18 ($\approx$ 1 radian) using the equation:

$$\Delta P = \frac{d\phi\lambda}{4\pi n g \psi} \tag{2.20}$$

Equation 2.20 estimates that the pressure modulation created by the sub-woofer was 350 dyn/cm^2 or $\sim$ 124 dB relative to 20 μPa, which is a standard sound power level (SPL) unit. The conversion factor for pressure modulation was analytically derived from calculating the strain experienced by a fiber under a pseudo-static pressure [83]. Therefore, phase change measured by ϕ-OTDR is more directly related to strain than pressure. Nonetheless, the ability to detect pressure change is how the popular name 'distributed acoustic sensing' was coined.

2.3.4 Interpretation of ϕ-OTDR Measurement Units

The most fundamental measurement made by ϕ-OTDR systems is a change in phase of the interferometer response, $d\phi$. The proportional change in phase over a length of fiber in one direction, $\frac{d\phi}{\phi}$ can be expressed as a summation of the effects of axial strain ($\varepsilon = \frac{dL}{L}$), relative refractive index change ($\frac{dn}{n}$) and relative optical wavenumber change ($\frac{dk}{k}$) as [19]:

$$\frac{d\phi}{\phi} = \frac{dL}{L} + \frac{dn}{n} + \frac{dk}{k} \tag{2.21}$$

These impacts are not independent. The refractive index is related to the strain through the phenomenon of photoelasticity, also known as the Pockels effect [84]. The cross-coupling of strain and refractive index is described by [85] as:

$$\frac{dn}{n} = -\frac{n^2}{2}\left[\nu\varepsilon(p_{11} + p_{12}) + \varepsilon(p_{12})\right] \tag{2.22}$$

where ε is the axial strain, ν is the Poisson's ratio and p_{11} and p_{12} are the Pockels coefficients [86]. Substituting Equation 2.22 into Equation 2.21 and assuming the change in optical wavenumber is negligible yields:

$$\frac{d\phi}{\phi} = \varepsilon - \frac{n^2}{2}\left[\nu\varepsilon(p_{11} + p_{12}) + \varepsilon(p_{12})\right] \quad \text{when} \quad \frac{dk}{k} \approx 0 \tag{2.23}$$

Typical values of Pockels coefficients p_{11} and p_{12} and Poisson's ratio ν for silica glass are 0.126, 0.270 and 0.17, respectively [83]. Substituting these values into Equation 2.23 allows the photoelastic scaling factor, ξ to be defined:

$$\frac{d\phi}{\phi} = \xi\varepsilon \approx 0.78\varepsilon \tag{2.24}$$

Calculating the unaltered light phase over a gauge length of optical fiber must account for the two-way transit [19].

$$\phi = 2nkg \tag{2.25}$$

Substituting Equation 2.25 into Equation 2.24 yields:

$$d\phi = 2nkg\xi\varepsilon = \frac{4\pi ng\xi\varepsilon}{\lambda} \tag{2.26}$$

2.3.5 Considerations for ϕ-OTDR Dynamic Strain Measurement

The representation of ϕ-OTDR measurements in Equation 2.26 has several shortcomings, which are sources of ϕ-OTDR strain measurement error. These sources of error are:

- laser frequency drift [87]
- temperature-induced refractive index changes [88]
- differential phase determination (unwrapping) errors [89]
- spatial averaging of the strain field [90]
- neglecting the optical pulse shape [91]

First, changes in optical wavenumber were neglected in the derivation of Equation 2.26. The validity of this assumption depends on the stability of the laser and the associated error is termed laser frequency drift. Drift may be adequately small over short time frames, but generally it is present and manifests as a slow drifting of the measurements [87].

The second problem is that temperature impacts on refractive index are ignored. Temperature has a non-negligible effect on the refractive index of a fiber, and this impact can even be used for temperature sensing [88]. Fortunately, temperature and laser drift tend to happen at low frequencies, typically below about 0.5 Hz. Errors due to both laser frequency drift and temperature-induced refractive index changes can be reduced by high pass filtering or time-differentiating the phase data, which attenuates signals near DC[11].

Phase determination errors can be the result of incorrect unwrapping, or sometimes called demodulation [92], of the circular phase. This can be due to phase changes that are too large between time samples to accurately track. It can also be the result of signal fading which causes low SNR and therefore a poorly determined phase measurement [93]. These phase errors typically manifest as jumps (step functions) in the time domain phase data, or broadband noise in the frequency domain. The maximum phase rate ($d\dot{\varphi}_{max}$) that can be tracked is described by:

$$d\dot{\phi}_{max} = \pi f_{Ny} \tag{2.27}$$

where f_ny is the effective optical Nyquist frequency of the ϕ-OTDR system. This varies from system to system depending on diversity processing configurations. If the maximum

phase rate is exceeded then the system will not track the phase correctly and there will be an error.

The spatial averaging and optical pulse shape impacts will be explored in depth in Chapter 3. However it is important to define the notation that will be used for ϕ-OTDR measurements in this dissertation. Since measurement of strain over a gauge length of fiber specific implications for the amplitude and phase of a measured dynamic strain field [90, 94], it is not thorough to refer to the measurements made by ϕ-OTDR as strain (ε). Measurements are more accurately referred to as average strain ($\hat{\varepsilon}$). In addition to the application of spatial averaging, dynamic measurements are also convolved in space with the shape of the optical pulse that they are made with [91]. This has a diminishing impact as strain frequencies decrease, however it is also not entirely correct to refer to the measurements as purely average strain ($\hat{\varepsilon}$), instead they will be referred to throughout this dissertation as $\hat{\varepsilon}_{\phi-OTDR}$ to make it clear that what is being described is the ideal (noise-free) ϕ-OTDR-measured strain approximation.

For the practical purposes and assuming the maximum phase rate is not exceeded, it can be stated without much error that:

$$\hat{\varepsilon}_{\phi-OTDR} = \frac{\lambda d\phi}{4\pi n g \xi} \tag{2.28}$$

when

$$\mathcal{F}\left\{\hat{\varepsilon}_{\phi-OTDR}\right\} = \hat{E}_{DAS}(f) = 0 \quad \rightarrow \quad f > \ \sim 0.5 \ \text{Hz} \tag{2.29}$$

For this reason it is a standard operation in this dissertation to highpass filter all of the $\phi - OTDR$ measurements, mitigating the low-frequency noise. Other noise sources exist which are specific to the electronics including thermal effects on the photodetector, shot and amplifier noise [95], though these sources are typically not addressed by an end user.

2.4 ϕ-OTDR in the Earth and Planetary Science Community

The earth and planetary science community has led the implementation of ϕ-OTDR for scientific research. This is primarily because as ϕ-OTDR was commercialized, a fruitful application space that was the target of patents and innovation was the oil and gas industry. ϕ-OTDR was demonstrated as an effective tool for monitoring seismic waves used for imaging and monitoring oil and gas fields. This quickly spread into measuring seismic waves for other applications including monitoring geothermal and carbon sequestration systems, crustal imaging, earthquake seismology, gaciology, volcanology and others. A common observation of using ϕ-OTDR in these disciplines is that it is rich with signals from unintentional anthropogenic origin including people movement, vehicles, and even building dynamics. The body of research within earth and planetary science can be viewed as another origin for the

research in this dissertation, which seeks to join the work and observations made in the earth and planetary science community with research done in civil infrastructure monitoring using DFOS. Therefore, it is important to conduct a review of the history of ϕ-OTDR application within earth and planetary science. Notably, an important contribution that the civil engineering DFOS background brings is the importance of fiber-cable-infrastructure coupling. Coupling of the sensing fiber to its surroundings is crucial for accurate strain measurements, which has generally not been emphasized in earth and planetary science research.

2.4.1 Exploration and Crustal Scale Imaging

ϕ-OTDR data was shown in the early 2010's to be able to emulate geophone and accelerometer data by providing phase-coherent seismic information over long lengths of fiber optic cables installed along the ground surface or within wells (Daley et al. 2013). Though the amplitude of the measured information was not initially a main interest, the measurement of phase relationships of seismic wave arrivals allowed for ϕ-OTDR to be used effectively for subsurface imaging and monitoring at the exploration scale. Mestayer et al. 2011 and Molenaar et al. 2011 are two of the earliest published examples of downhole ϕ-OTDR deployments used to monitor hydraulic fracturing and demonstrate the possibility of vertical seismic profiling (VSP) using ϕ-OTDR data. This work has been further developed over the last decade through downhole deployment of ϕ-OTDR in boreholes with varying installation techniques and ϕ-OTDR IUs [96–100]. Importantly, these experiments showed that coupling of the fiber optic cable to the well through cementation greatly improves data quality [101].

ϕ-OTDR was also widely adopted for passively imaging the earth's crust using ambient noise techniques. The implementation of ϕ-OTDR fit well into the developing field of ambient noise imaging that was relying on nodal sensors to make measurements of naturally occurring surface wave energy [102]. This technique was costly and laborious due to the need to separately deploy each nodal sensor. ϕ-OTDR made it possible to leverage existing telecommunications optical fiber to collect ambient seismic noise across large apertures [103, 104]. The directional sensitivity of ϕ-OTDR measurements presents a challenge for correctly interpreting ambient noise data recorded on ϕ-OTDR in certain geometries [90], but overall, it has been proven as a very effective tool for passively imaging the subsurface. Successful implementations of using ϕ-OTDR for passive imaging have included using purposefully installed fiber optic cables for sensing as well as leveraging unused telecommunications cables [103, 105]. It has been thoroughly demonstrated that ϕ-OTDR can be used to measure ambient noise to infer important geotechnical parameters and indices such as the horizontal component of the horizontal-to-vertical spectral ratio (HVSR) and shear wave velocity profile using the inversion of surface wave dispersion behavior [106, 107].

2.4.2 Earthquake Seismology

ϕ-OTDR has also received much attention for its use in earthquake seismology. Because of the inherent array-nature of ϕ-OTDR, beamforming and multi-dimensional transformations

have become effective techniques for analyzing even very weak wavefields from earthquakes using ϕ-OTDR data. Lindsey et al. [108] described the use of ϕ-OTDR with various optical fiber installation techniques for measuring the wavefields from local and teleseismic events. This lead to a growing field of research that had expanded from seismic event detection to characterizing the subsurface using energy from earthquakes [109, 110]. It was demonstrated ϕ-OTDR even be used with submarine telecommunications cables to map offshore geology [111].

2.4.3 Monitoring of Anthropogenic Processes

During the demonstration of ϕ-OTDR as an effective tool for measuring earth-processes, it was apparent that it was equally as effective for measuring anthropogenic signals. In fact, as unused telecommunication cable (dark fiber) gained popularity for collecting ϕ-OTDR data over large spatial aperatures and in urban settings, anthropogenic signals dominated the seismic datasets. One of the earliest studies to use dark fiber was Jousset et al. [112]. In that seminal study, vehicle signals were prominent in the data. It was presented that vehicle signals could not only be detected, but that their origin and nature was strain on the telecommunications cable from the roadbed's deformation. A simple model was introduced for back-calculating the P-wave velocity from the strain level and speed of a vehicle on the road near the ϕ-OTDR array. Lindsey et al. [105] extended this work to examine the roadbed strain caused by passing vehicles along a section of dark fiber in Palo Alto, CA. It was demonstrated that the reduction in anthropogenic activities during the COVID-19 pandemic was evident by both examining the spectral content of the ϕ-OTDR records and the cumulative strain that was measured. This study also showed the effectiveness of a simple ground deformation model for identifying and counting vehicles. Vehicle signals were also leveraged as noise sources for enhancing ambient noise interferometry [103, 113]. Williams et al. [114] showed that offshore telecommunications fiber detects vibrations from nearby wind turbines. Other researchers have noted energy from human footsteps being recorded on ϕ-OTDR arrays and have developed methods for extracting and identifying them [115]. In addition, ϕ-OTDR has also been used to detect signals from trains [116, 117], explosions [118], concerts [119] and even ships in the ocean [120]. Though many of these studies for monitoring anthropogenic activities have explained that the origin of the signals is strain, from either direct ground deformation (sometimes called geodetic strain) or propagating stress-waves, the specific coupling of the optical fiber to the surroundings has been difficult to quantify when dark fiber is used, making the amplitude of the strain measurements unreliable.

2.5 Justification of Research Objectives

From evaluating the bodies of literature pertaining to ϕ-OTDR in the civil engineering, optical and electrical engineering, and earth and planetary science fields the research objectives

of this dissertation are affirmed. The specific objectives and their justifications are:

1. **Develop installation procedures and validate the strain measurements made in practical civil engineering deployments by comparing ϕ-OTDR to other instrumentation.**

   Though ϕ-OTDR has been proposed as a strain-measuring technique in its earliest development [121], it has not been validated alongside other accepted techniques in the field of civil infrastructure monitoring. Moreover, the amplitude of the measurements made in earth and planetary science studies have been variable at best due to a justified lack of emphasis on cable coupling and installation. In order for ϕ-OTDR to be considered an adoptable technique civil infrastructure monitoring installation techniques must be developed and comparisons with known and accepted methods must be made.

2. **Test ϕ-OTDR's potential for measuring phenomena in civil infrastructure that is currently not possible with the tools common in the field due to its superior strain precision, acquisition rates and measurement distance.**

   It is clear in the literature that the implementation of dynamic, distributed strain sensing in civil infrastructure monitoring has been limited. The only implementations within the field have been of OFDR, a technology with inferior range, strain precision and acquisition rate as compared to ϕ-OTDR. Nonetheless, the value of dynamic, distributed strain sensing has been demonstrated as potentially being able to localize damage and detect changes in dynamic behavior in complex infrastructure. The limited measurement length makes implementation of the currently-available commercial OFDR systems impractical, and the limited acquisition rate severely limits the dynamic behavior that can be detected. In addition, the strain precision reported in the literature that is possible with ϕ-OTDR is orders of magnitude smaller than OFDR. Currently, there are no DFOS technologies that are as promising as ϕ-OTDR for long distance, distributed dynamic strain monitoring.

Research objective 1 is addressed in part by all body chapters in this dissertation. Chapter 3, however, goes in the most detail of validating the measurements made by ϕ-OTDR by comparing them to dynamic strain measured by an array of highly sensitive velocity transducers (geophones). Chapters 3, 4 and 5 present effective installations of optical fiber for ϕ-OTDR including cable type and installation procedure.

Research objective 2 is also accomplished in part by all of the body chapters, however particularly Chapters 4 and 5 show implementations in civil infrastructure where observations made by ϕ-OTDR are completely unique. In Chapters 4, ϕ-OTDR is demonstrated as a technology that can practically turn a road surface into a touchscreen, by being able to both localize and detect strains from extremely small events. Chapter 5, on the other hand, shows how ϕ-OTDR can not only detect the global changes in structural properties, like changes in natural frequency, but also localize defects creating a unique two-pronged value for SHM.

Chapter 3

Measurement of Soil Deformation and Stress-Wave Propagation

This chapter is adapted from an article published in the journal *Sensors* on June 17th, 2022. The article is available open-access at the following citation [122]:

Peter G. Hubbard et al. "Quantifying the Surface Strain Field Induced by Active Sources with Distributed Acoustic Sensing: Theory and Practice". In: *Sensors*. 22(4589). (2022). DOI: 10.3390/s22124589.

This chapter provides a demonstration, for the first time, that ϕ-OTDR strain measurements are consistent with strain computed using geophone measurements for large amplitude and wide bandwidth signals. First, the transfer function for a linear ϕ-OTDR array is developed considering a system's gauge length, pulse shape, and the cable that is used for the measurements. 3-D numerical simulations of ground strain caused by active sources are presented to demonstrate the theoretical angular response of ϕ-OTDR arrays. Next, An installation method that provides effective ground-coupling to the fiber optic cable is then presented. This is followed by experimental results from measuring ground strain with both ϕ-OTDR and geophones when stress-waves are created by large vibrosies sources and a smaller sledge hammer. The results show that the angular reception patterns can be observed in the field, and that the measuremetns made with both technologies are equivalent. The implications of the ϕ-OTDR transfer functions are discussed including a methodology for assessing the field data quality based on the wavelength-to-gauge length ratio. This contents of this chapter lay the groundwork for the use of ϕ-OTDR in geotechnical engineering.

3.1 Background

It has been described for a geophysical application that the measurements made by ϕ-OTDR are approximately proportional to average normal strain ($\hat{\varepsilon}$) or average strain-rate ($\hat{\dot{\varepsilon}}$) in the

ground [97], as defined by:

$$\hat{\dot{\varepsilon}}_{\phi-OTDR} \approx \frac{\left[u\left(x+\frac{g}{2},t+dt\right)-u\left(x-\frac{g}{2},t+dt\right)\right]-\left[u\left(x+\frac{g}{2},t\right)-u\left(x-\frac{g}{2},t\right)\right]}{gdt} \tag{3.1}$$

where u is the displacement in the direction of the cable (i.e., the x-direction), and dt is the time step between samples. It should be noted that Equation 3.1 assumes perfectly discrete scattering locations, when it is actually a distribution over the light pulse's shape [94]. This has allowed for the approximate conversion of ϕ-OTDR-measured strain to pointwise particle velocity assuming non-dispersive signals and large wavelengths relative to the gauge length of the ϕ-OTDR system. This relationship is:

$$\hat{\varepsilon}_{\phi-OTDR} \approx \frac{du}{dx} = \frac{du}{cdt} = \frac{v}{c} \tag{3.2}$$

where c is the phase velocity of the propagating seismic wave and v is the particle velocity in the direction of the ϕ-OTDR measurement.

The relationship given in Equation 3.2 only works when the average strain is close to the pointwise strain ($\frac{du}{dx}$) and when c can be easily estimated for all frequency components within the measured signal. It is demonstrated effectively for isolated body wave arrivals within boreholes in Daley et al. [97]. Wang et al. [109] applied the relationships in both Equations 3.1 & 3.2 to a surface ϕ-OTDR array and co-located geophones to measure long-wavelength signals at the crustal scale. It was shown that the waveforms matched well for non-dispersive signals within a frequency band of 1-5 Hz and amplitudes less than 100 nε/s. c was estimated by examining the moveout of a constant phase across the array. This finding was significant for seismological applications of ϕ-OTDR, as the recorded signals were generated from a M_L 4.3 earthquake and recorded across a wide aperture array of both geophones and ϕ-OTDR. It was noted that the amplitudes for the first few cycles were approximately the same between ϕ-OTDR and geophones but began to deviate later in the waveform following the S-wave arrival. This was attributed to interference between P- and S-wave coda, and a misalignment of the geophone and ϕ-OTDR measurement locations. In this chapter, it will be shown that ϕ-OTDR measurements can be consistent with geophone measurements at an engineering scale regardless of wavefield complexities for broadband and high amplitude signals.

Most reported ϕ-OTDR applications have not examined the amplitude of the signals or put emphasis on converting them to physical units because the phase behavior of the measurements was of primary interest. For example, Mateeva et al. [123] presents one of the first explanations of ϕ-OTDR for seismic monitoring in boreholes, where a comparison between ϕ-OTDR and geophones is performed for picking body wave arrivals. This required identifying seismic phases in the raw data; the signal's specific amplitude or units was not used. Song et al. [124] shows the use of ϕ-OTDR for measuring surface wave dispersion to invert the velocity structure of the near subsurface. A step in this process is normalizing the amplitude of the traces, which is a common step in surface wave processing. Vantassel et al. [125] demonstrated that measurements of surface wave dispersion using ϕ-OTDR

and geophone data could be compared in their respective raw units and produce essentially equivalent results, if frequency-dependent normalization was applied to the dispersion images following processing. Since the phase component of the ϕ-OTDR measurement alone has served the needs of the geophysical community, there has been little effort to study and quantify the signal amplitude. However, for more advanced imaging techniques, such as full-waveform inversion (FWI), both phase and amplitude are required [126]. Geophysical research has begun to move in the direction of using ϕ-OTDR for FWI. For example, Egorov et al. [127] used ϕ-OTDR VSP data for FWI. The ϕ-OTDR data was converted to equivalent units as the geophones using Equation 3.2 and then a shaping filter was applied to better match the ϕ-OTDR and geophone traces. Eaid et al. [128] also conducted FWI using ϕ-OTDR in units of strain, but the FWI residuals were normalized by the L_2-norm of the ϕ-OTDR data, effectively removing its amplitude. Furthermore, to use ϕ-OTDR as an engineering tool to monitor soil structure interaction and ground deformation the amplitude of the strain measurements must be verified and not subjectively shaped.

This chapter aims to provide a procedure for using ϕ-OTDR data as quantitative ground strain measurements for stress-wave-based imaging techniques, such as FWI, that do not rely on the subjective shaping of the signal's amplitude, or for engineering problems like soil-structure interaction and ground deformation monitoring. Specifically, this chapter will first demonstrate how ϕ-OTDR data can be modeled as a finite-difference of the displacement field, and then how to practically implement a quantitative acquisition in the field. The implications of measuring a spatially differenced displacement field are explored through the transfer function of ϕ-OTDR and 3-D finite difference simulations of seismic waves produced by active sources. These theoretical observations are compared with field-measured wavefields when an optical fiber is carefully coupled with the ground and seismic waves are created with active sources. The amplitudes of the strain measurements made with ϕ-OTDR are validated through quantitative comparison to geophones.

3.2 ϕ-OTDR Spatial Transfer Function for Linear Surface Arrays

Since ϕ-OTDR measurements made along an array have dimensions of space and time, the transfer function is also two-dimensional in wavenumber and frequency. We develop the transfer function of ϕ-OTDR $H(f,k)$ as a multiplication of two transfer functions of independent variables, $H_f(f)$ and $H_k(k)$ such that:

$$H(f,k) = H_f(f)H_k(k) \tag{3.3}$$

where f and k are linear wavenumber and frequency respectively. $H(f,k)$ transfers the axial strain field along the array, described by its Fourier transform $E(f,k)$ into ϕ-OTDR strain measurements with Fourier transform $\hat{E}_{\phi-OTDR}(f,k)$ as:

$$\hat{E}_{\phi-OTDR}(f,k) = H(f,k)E(f,k) \tag{3.4}$$

We assume that $H(f,k)$ does not vary in f (i.e. a single measurement channel's response is the same for all temporal frequencies). Therefore, we state:

$$H_f(f) = 1 \tag{3.5}$$

The spatial transfer function $H_k(k)$ can be described as a combination of effects from the gauge length, pulse shape and cable used for the ϕ-OTDR array as:

$$H_k(k) = \mathbb{G}(k)\mathbb{P}(k)\mathbb{C}(k) \tag{3.6}$$

where $\mathbb{G}(k)$, $\mathbb{P}(k)$, and $\mathbb{C}(k)$ are the transfer functions induced by the application of the gauge length, pulse shape and cable, respectively.

3.2.1 Transfer Function due to Gauge Length

The application of the gauge length can be represented as convolution of the spatial strain field $\varepsilon_x(x)$ with a scaled rectangular pulse. We use subscript x to denote that the strain field is also a function of space and time, though now only variation in space is being described. In the space domain this is stated as:

$$\hat{\varepsilon}_{x,g}(x) = \varepsilon_x(x) * \frac{1}{g}\Pi(\frac{x}{g}) \tag{3.7}$$

where $\hat{\varepsilon}_{x,g}(x)$ is the averaged spatial strain field through application of the gauge length, and $\Pi(x)$ is the rectangular window defined by Bracewell [129] as:

$$\Pi(x) = \begin{cases} 0, & |x| > \frac{1}{2} \\ 1, & |x| < \frac{1}{2} \end{cases} \tag{3.8}$$

This operation is equivalent to multiplication in the wavenumber domain with $\mathbb{G}(k)$ defined as:

$$\mathbb{G}(k) = \mathcal{F}\Big\{\frac{1}{g}\Pi(\frac{x}{g})\Big\} = \frac{\sin(\pi k g)}{\pi k g} \tag{3.9}$$

which has been described previously by Dean et al. [94] as the gauge length effect on ϕ-OTDR measurements made of axially propagating pressure waves.

3.2.2 Transfer Function due to Pulse Shape

The pulse shape of ϕ-OTDR systems can be approximated as a Gaussian window. Dean et al. [91] presented the filter caused by the pulse shape in the time domain. It is represented here in the space domain for compatibility with the other transfer functions. The pulse

shape filter is a Gaussian function in both the space and wavenumber domains. In the space domain it is:

$$p(x) = \frac{1}{\sqrt{2\pi}\sigma_x} e^{\frac{-x^2}{2\sigma_x^2}} \tag{3.10}$$

and in the wavenumber domain it is:

$$\mathbb{P}(k) = e^{\frac{-k^2}{2\sigma_k^2}} \tag{3.11}$$

where σ_x and σ_k are the standard deviations in the space and wavenumber domains, respectively, of the Gaussian functions. These are related to the pulse width h_p of the ϕ-OTDR system by:

$$\sigma_x = \frac{h_p}{2.3548} \tag{3.12}$$

and

$$\sigma_k = \frac{1}{2\pi\sigma_x} \tag{3.13}$$

This assumes a pulse width that is defined as the full-width at half maximum (FWHM) of a Gaussian function. Note that most ϕ-OTDR systems define the pulse duration in time t_p, which can be converted to a spatial length using the speed of light in vacuum $\mathbf{c}$ and the group refractive index of the optical fiber through:

$$h_p = \frac{t_p \mathbf{c}}{n} \tag{3.14}$$

3.2.3 Transfer Function due to Cable Coupling

The transfer function caused by the cable can be approximated using the strain transfer relationship for layered cables developed by Ansari and Libo [130] and expanded by Li et al [131]. This solution assumes no slipping at cable material interfaces or within the host media. The assumption requires a cable that is well bonded to both the host media and the optical fiber core. The relationship was originally applied to ϕ-OTDR data by Reinsch et al. [132] for the case when the seismic wavelength and ϕ-OTDR gauge length are equal. However we suggest a differing approach that incorporates the seismic wavelength and the gauge length separately into the formulation by integrating the governing equation over the gauge length of a ϕ-OTDR system. The ratio of strain experienced by an optical fiber to the uniform axial strain in the cable's host media can be described as [131]:

$$\zeta(x) = 1 - \frac{\cosh(\beta x)}{\cosh(\beta \frac{L}{2})} \tag{3.15}$$

Where $\zeta(x)$ is the ratio of strain transferred as a function of position along the cable, β is the shear lag parameter and L is the length of the bonded fiber section. β is a function of the material properties of a layered cable as:

$$\beta^2 = \frac{2}{r_{of}^2 E_{of}[\sum_{j=2}^{n}(1/G_j)\ln(r_j/r_{i-1}) + (1/G_1)\ln(r_1/r_{of})]} \tag{3.16}$$

where r_{of} is the radius of the optical fiber including the core and cladding, r_j is the outer radius of layer j, E_{of} is the Young's modulus of the optical fiber and G_j is the shear modulus of layer j. We approximate the uniform strain distribution as the strain in one-half of a seismic wavelength, and take the average over a single gauge length of optical fiber. This results in a function of wavenumber as:

$$\mathbb{C}(k) = \frac{1}{g}\int_{-\frac{g}{2}}^{\frac{g}{2}}\left[1 - \frac{\cosh(\beta x)}{\cosh(\beta\frac{1}{k})}dx\right] = 1 - \frac{2\sinh(\beta\frac{g}{2})\,\mathrm{sech}(\frac{\beta}{k})}{g\beta} \tag{3.17}$$

where $\mathbb{C}(k)$ is the ratio of average strain on the optical fiber to average strain on the cable exterior over a gauge length as a function of linear wavenumber.

The full ϕ-OTDR transfer function is then described as:

$$H(f,k) = \frac{\sin(\pi k g)}{\pi k g} e^{\frac{-k^2}{2\sigma_k^2}}\left[1 - \frac{2\sinh(\beta\frac{g}{2})\,\mathrm{sech}(\frac{\beta}{k})}{g\beta}\right] \tag{3.18}$$

These transfer functions are best understood with a physical example which is given after the presentation of field measurements in Section 3.9. Next we develop the relationship between strain measurements made with geophones and ϕ-OTDR because geophones will be used later as a verification tool.

3.3 Relationship between Geophone and ϕ-OTDR Measurements

Geophone measurements are proportional to particle velocity when the fundamental frequency of the geophone's oscillating proof mass f_0 is close to the exciting frequency f [133]. In this case the Fourier transform of the velocity experienced by a geophone's housing $V_{geo}(f)$ can be described by:

$$V_{geo}(f) = \frac{V_{mass}(f)}{J(f)} \tag{3.19}$$

where $V_{mass}(f)$ is the Fourier transform of the velocity of the proof mass which is proportional to electrical potential generated by the geophone and $J(f)$ is the transfer function due to the mechanical and electrical properties of a geophone. $J(f)$ is the transfer function of a damped, forced harmonic motion system with a single degree of freedom defined as [133]:

$$J(f) = \frac{Sf^2}{-f^2 + 2iD(f_0)(f) + (f_0)^2} \tag{3.20}$$

where S is a scaling factor to convert from electrical potential to velocity, D is the damping of the geophone coil and i is the imaginary unit.

The displacement of the ground can be measured by removing $J(f)$ from $V_{mass}(f)$ as done in Equation 3.19 and integrating with respect to time. This is expressed as:

$$U_{geo,f}(f) = \frac{V_{geo}(f)}{i2\pi f}, \quad \text{when} \quad V_{geo}(0) = 0 \tag{3.21}$$

The average strain between two geophones is determined by subtracting the displacements measured by a pair of geophones and dividing by their separation distance. This is the same as taking the scaled finite difference of the spatial displacement field as:

$$\hat{\varepsilon}_{x,geo}(x) = u_{x,geo}(x) * \frac{2}{\Delta x} \mathrm{I}_{\mathrm{I}}(\frac{x}{\Delta x}) \tag{3.22}$$

where $u_{x,geo}(x)$ is the displacement field measured by geophones as a function of space, Δx is the geophone spacing and $\mathrm{I}_{\mathrm{I}}(x)$ is the odd impulse pair defined by Bracewell [129] as:

$$\mathrm{I}_{\mathrm{I}}(x) = \frac{1}{2}\delta(x + \frac{1}{2}) - \frac{1}{2}\delta(x - \frac{1}{2}) \tag{3.23}$$

and δ is the Dirac delta function. In the wavenumber domain this operation is:

$$\hat{E}_{k,geo}(k) = U_{k,geo}(k) \frac{i2\sin(\pi k \Delta x)}{\Delta x} \tag{3.24}$$

Equation 3.22 is performing the same operation as Equation 3.7 since:

$$u_x(x) = \int \varepsilon_x(x) dx \tag{3.25}$$

and

$$\frac{1}{i2\pi k} \frac{i2\sin(\pi k \Delta x)}{\Delta x} = \frac{\sin(\pi k g)}{\pi k g}, \quad \Delta x = g \tag{3.26}$$

The technique of using geophones to take a finite difference of the displacement field has been used in seismic gradiometry for directly inverting wave equations that incorporate spatial gradients of displacement [134, 135]. The finite difference process assumes homogeneity over the stencil span (i.e. geophone spacing) and results deviate from the true strain as wavenumbers increase. It is effective when:

$$U_k(k) \frac{i2\sin(\pi k \Delta x)}{\Delta x} \approx U_k(k) i2\pi k \tag{3.27}$$

which is a judgement call for a user depending on the accuracy required by the application. For example, Langston [134] suggests a Δx of no larger than 10% of the shortest wavelength to be reliably measured.

In practice, the transformation of the geophone measurements into average strain that are similar to ϕ-OTDR measurements is made by differencing two time-integrated and instrument-corrected geophones spaced by the ϕ-OTDR gauge length as:

$$\hat{\varepsilon}_{\phi-OTDR}(x,t) \approx \frac{\int v_{geo}(x+\frac{g}{2},t)dt - \int v_{geo}(x-\frac{g}{2},t)dt}{g} \tag{3.28}$$

Note that this approximation neglects the impacts of a ϕ-OTDR system's pulse shape and cable design. Equation 3.28 is valid only when a ϕ-OTDR channel is centered between two geophones. This is shown schematically in Figure 3.1. In this case the scattering centers, or the origin of the Rayleigh backscatter, are at the same location as the first order centered finite difference of the geophones. The two light pulses in Figure 3.1 show the position of the interrogating light pulses at the time of scattering.

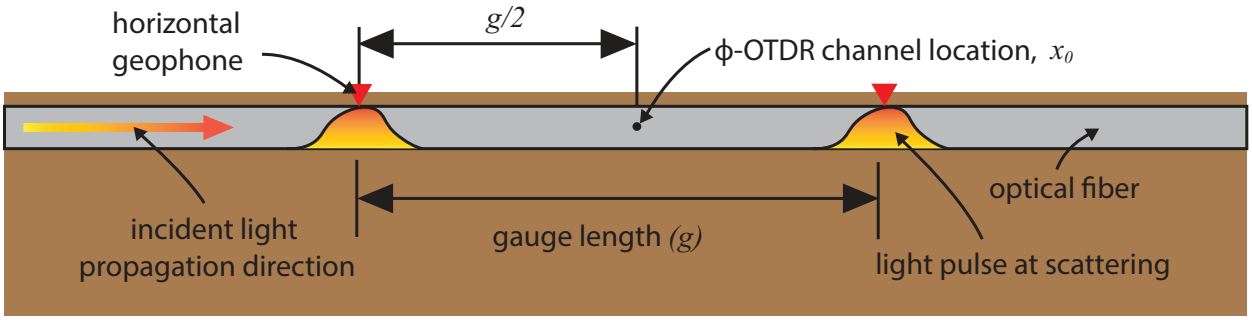

Figure 3.1: Schematic of ϕ-OTDR sensing as described by the difference between two geophones collocated with the interrogating light pulses at the time of back scattering.

3.4 Directionality of 1-D Strain Measurements

The representation of a strain seismic sensor has been presented by Benioff [136]. Lomnitz [137] described the frequency response of this type of system to axially incident plane waves. This was elaborated on by Martin et al. [138] for the case of using strain-rate ϕ-OTDR measurements at the ground surface, neglecting the pulse shape and cable coupling. Martin et al. [138] presents the analytical full waveform representations of pointwise and distributed strain-rate measurements to all types of planar surface and body waves. The expressions found in that work have been time-integrated and simplified by removing the amplitude and oscillatory factors and are presented in Table 3.1. The purpose of these expressions is to compare the directional sensitivity of different wave types between theoretical point and approximate ϕ-OTDR measurements. The directional sensitivity (z) is a multiplier of the

solution to the wave equation that determines what strain occurs as a function of angles in the horizontal and vertical planes between an incoming wave and the measurement direction of a sensor, and the wavelength (λ) of the seismic wave. The angles are denoted as θ and α for the horizontal and vertical planes, respectively. This is given for both a point sensor (z_ε) and a distributed measurement over a gauge length ($z_{\varepsilon,g}$). The body waves are also a function of the angle in the vertical plane (α). Note that for a horizontally traveling body waves (i.e., α=0) the P and Rayleigh expressions are equal, and SH and Love expressions are equal. It is important to note that these expressions assume a far-field, plane wave source which is not always a valid assumption in active source testing.

Table 3.1: Directional and wavelength sensitivity of point and distributed strain measurements to seismic waves adapted from Martin et al. [138]

Wave Type	**Measurement type**	**Quantity**	**Expression**
Rayleigh	point	$z_\varepsilon(\theta,\ \lambda)$	$\frac{2\pi}{\lambda}cos^2(\theta)$
	distributed	$z_{\varepsilon,g}(\theta,\lambda)$	$\frac{2}{g}cos(\theta)sin(\frac{\pi g cos(\theta)}{\lambda})$
Pressure (P)	point	$z_\varepsilon(\theta,\alpha,\lambda)$	$\frac{2\pi}{\lambda}cos^2(\theta)\ cos^2(\alpha)$
	distributed	$z_{\varepsilon,g}(\theta,\alpha,\ \lambda)$	$\frac{2}{g}cos(\theta)cos(\alpha)sin(\frac{\pi g cos(\theta)cos(\alpha)}{\lambda})$
Love	point	$z_\varepsilon(\theta,\ \lambda)$	$\frac{\pi}{\lambda}sin\,(2\theta)$
	distributed	$z_{\varepsilon,g}(\theta,\lambda)$	$\frac{2}{g}\sin(\theta)sin(\frac{\pi g cos(\theta)}{\lambda})$
Horizontally Polarized Shear (SH)	point	$z_\varepsilon(\theta,\alpha,\lambda)$	$\frac{\pi}{\lambda}sin\,(2\theta)\,cos(\alpha)$
	distributed	$z_{\varepsilon,g}(\theta,\alpha,\ \lambda)$	$\frac{2}{g}\sin(\theta)sin(\frac{\pi g cos(\theta)cos(\alpha)}{\lambda})$
Vertically Polarized Shear (SV)	point	$z_\varepsilon(\theta,\alpha,\lambda)$	$\frac{\pi}{\lambda}cos^2(\theta)\ sin(2\alpha)$
	distributed	$z_{\varepsilon,g}(\theta,\alpha,\ \lambda)$	$\frac{1}{g}\frac{cos(\theta)sin(2\alpha)}{cos(\alpha)}sin(\frac{\pi g cos(\theta)cos(\alpha)}{\lambda})$

If the ratio of distributed strain to pointwise strain is calculated, it can be shown for all surface waves:

$$R_{\varepsilon,SW}(\theta,\lambda) = \frac{\lambda sin(\frac{\pi g cos(\theta)}{\lambda})}{\pi g cos(\theta)} \tag{3.29}$$

and for all body waves:

$$R_{\varepsilon,BW}(\theta,\alpha,\lambda) = \frac{\lambda sin(\frac{\pi g cos(\theta)cos(\alpha)}{\lambda})}{\pi g cos(\theta)cos(\alpha)} \tag{3.30}$$

where $R_{\varepsilon,SW}$ and $R_{\varepsilon,BW}$ are the ratios of distributed to pointwise strain for surface waves and body waves, respectively. Notice that:

$$R_{\varepsilon,SW}(\theta,\lambda) = R_{\varepsilon,BW}(\theta,\alpha,\lambda) = \mathbb{G}(\frac{1}{\lambda}),\quad \text{when} \begin{cases} \theta = 0°, 180° \\ \text{and} \\ \alpha = 0°, 180° \end{cases} \tag{3.31}$$

Equations 3.29 and 3.30 can be viewed as extending the gauge length transfer function described in Equation 3.9 to azimuthal effects of an incoming wave.

It is useful to visualize these expressions as a function of the ratio between signal wavelength (λ) and gauge length of an ideal distributed sensor (i.e. a ϕ-OTDR system that neglects pulse shape and cable design effects). Figure 3.2 shows this for the case of α=0° along with the relative amplitude measured between the distributed and pointwise sensors as a function of θ for P, Rayleigh, SH, and Love waves. SV waves have been omitted for brevity. For Rayleigh and P waves at λ/g=1, the distributed sensor response is zero for incoming waves at 0°, 90°, 180°, and 270°. Love and SH waves always have zeros at 0°, 90°, 180°, and 270°, though the response of the distributed sensor is noticeably distorted from the pointwise strain measurement at low λ/g values. As λ/g increases, the response of the distributed sensor approaches the pointwise strain measurement. This phenomenon is important for using ϕ-OTDR for active source stress wave measurements because surveys need to be designed in such a way to avoid, or to expect, the zeros in the reception patterns for the waves that are being produced when either frequencies are high (i.e., short wavelengths) or when g is long. For example, an off-end survey geometry can never be expected to measure Love or direct SH waves. To avoid the zeros in the reception patterns, a variety of source positions need to be used if it is desired to maximize sensitivity to all types of seismic waves, and hence maximize the information gained from a site. In the next section we develop this idea further with numerical examples of simulated distributed sensor reception with different values of λ/g.

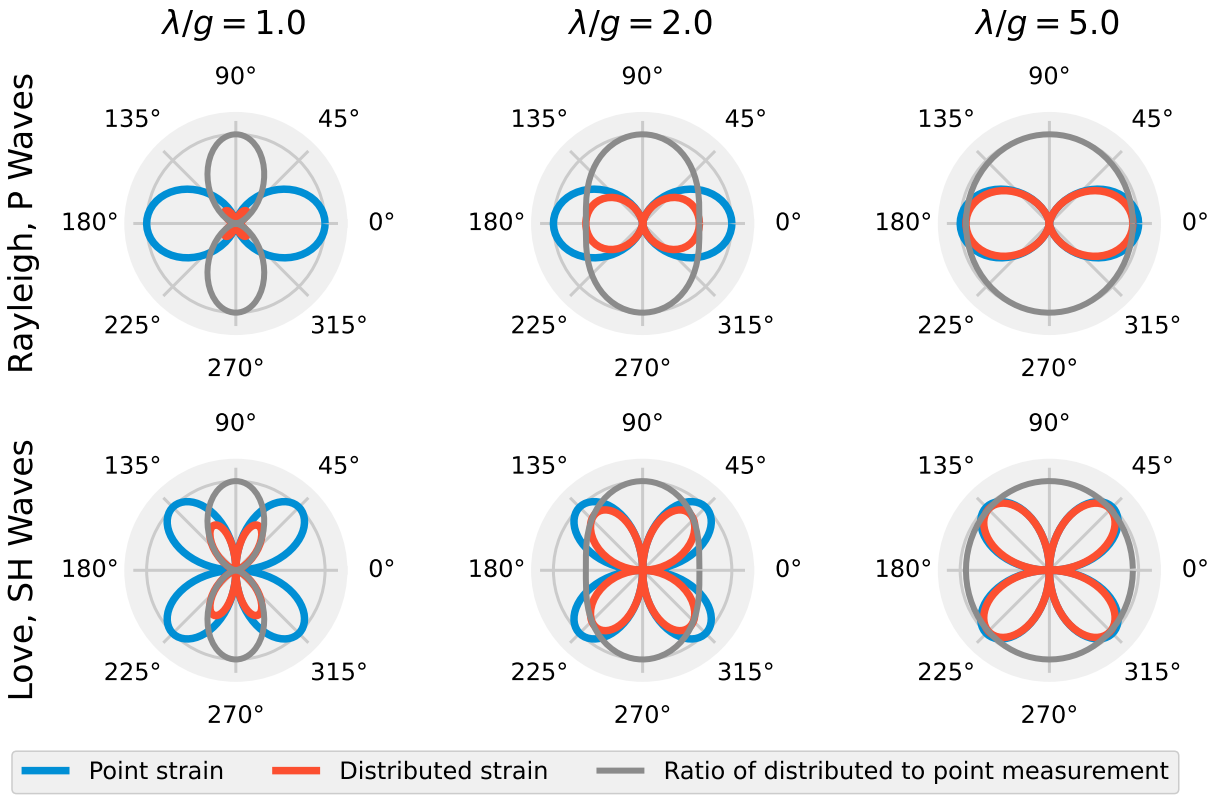

Figure 3.2: Radial reception patterns for pointwise strain and ideal distributed sensor-measured strain for wavelength to gauge length ratios (λ/g) of 1, 2 and 5 for Rayleigh, P, Love and SH waves. The patterns are plotted such that the maximum pointwise strain value is 1. In addition, the ratios of theoretical distributed strains and pointwise strains are shown as a function of angle in the horizontal plane (θ), which approaches unity for all wave types and angles as λ/g increases.

3.5 Numerical Approximation of ϕ-OTDR Measurements

The magnitude response of distributed strain measurements is examined for their dependance on λ/g and directionality through numerically simulated distributed and pointwise strain data. ϕ-OTDR data is approximately simulated by taking the finite difference of the calculated displacement field as would be done for geophone measurements described in Equation 3.22. This includes evaluating the point displacement at two locations in a model, taking a 1-D difference between them in the direction of the virtual ϕ-OTDR array and

dividing by their separation distance.

To demonstrate this technique, 3-D elastic stress wave propagation was simulated using Seismic Waves, 4th Order (SW4) node-based finite difference code [139]. The model consisted of an elastic half-space solid 200 m-wide, 200 m-long, and 100 m deep. The grid spacing was 0.5 m in all directions, resulting in 32,321,001 total grid points. The material was assigned a shear wave velocity of 250 m/s, compression wave velocity of 433 m/s and a density of 1800 kg/m^3. The velocity values created a material with a Poisson's ratio of 0.25 (also known as a Poisson solid). There was a free surface top boundary condition and absorbing super grid damping layers surrounding the model to minimize wave reflections at the boundaries. The model was excited using a point force at the top surface with a magnitude of 100 kN defined by a Ricker wavelet. The force was applied with different polarizations, including vertical, parallel to and perpendicular to the 1-D strain measurement direction. Each source with horizontal polarization began their Ricker wavelet source signal in the positive x or y-direction. The simulations created both surface and body waves with varying wavelengths. Since the model was a Poisson solid, Rayleigh waves propagated at 0.919 times the shear wave velocity, while Love waves propagated at approximately the shear wave velocity [140].

To evaluate the numerical models in terms of λ/g, the fundamental frequency of the source wavelet was set such that the vertical source created Rayleigh waves with a 10 m wavelength (22.975 Hz), and the horizontal sources created Love waves with a 10 m wavelength (25 Hz). Displacement and pointwise strain were evaluated at each grid point at the surface of the model for each run. The displacement values across the surface were then converted to equivalent 1-D distributed strain measurements for λ/g of 1 and 5. Essentially, each row of grid points is approximately converted to its own 1-D ϕ-OTDR array at the model's top surface.

The pointwise and distributed strain in the x-direction as evaluated 0.3 s after source initiation is shown in Figure 3.3 for the different source polarizations. The simulation results show the normal strain in the x-direction which is denoted in tensor notation as ε_{xx} for pointwise and $\hat{\varepsilon}_{xx}$ for distributed strain. These results can be thought of as approximately what a ϕ-OTDR array oriented parallel to the x-axis would measure. The top row displays the vertical source, the center row displays the horizontal source perpendicular to the strain measurement and the bottom row shows the horizontal source parallel to the strain measurement. The three columns from left to right correspond to pointwise strain, distributed strain with $\lambda/g \approx 5$ and distributed strain with $\lambda/g \approx 1$, respectively. All amplitudes are normalized relative to maximum strain exhibited across all simulations.

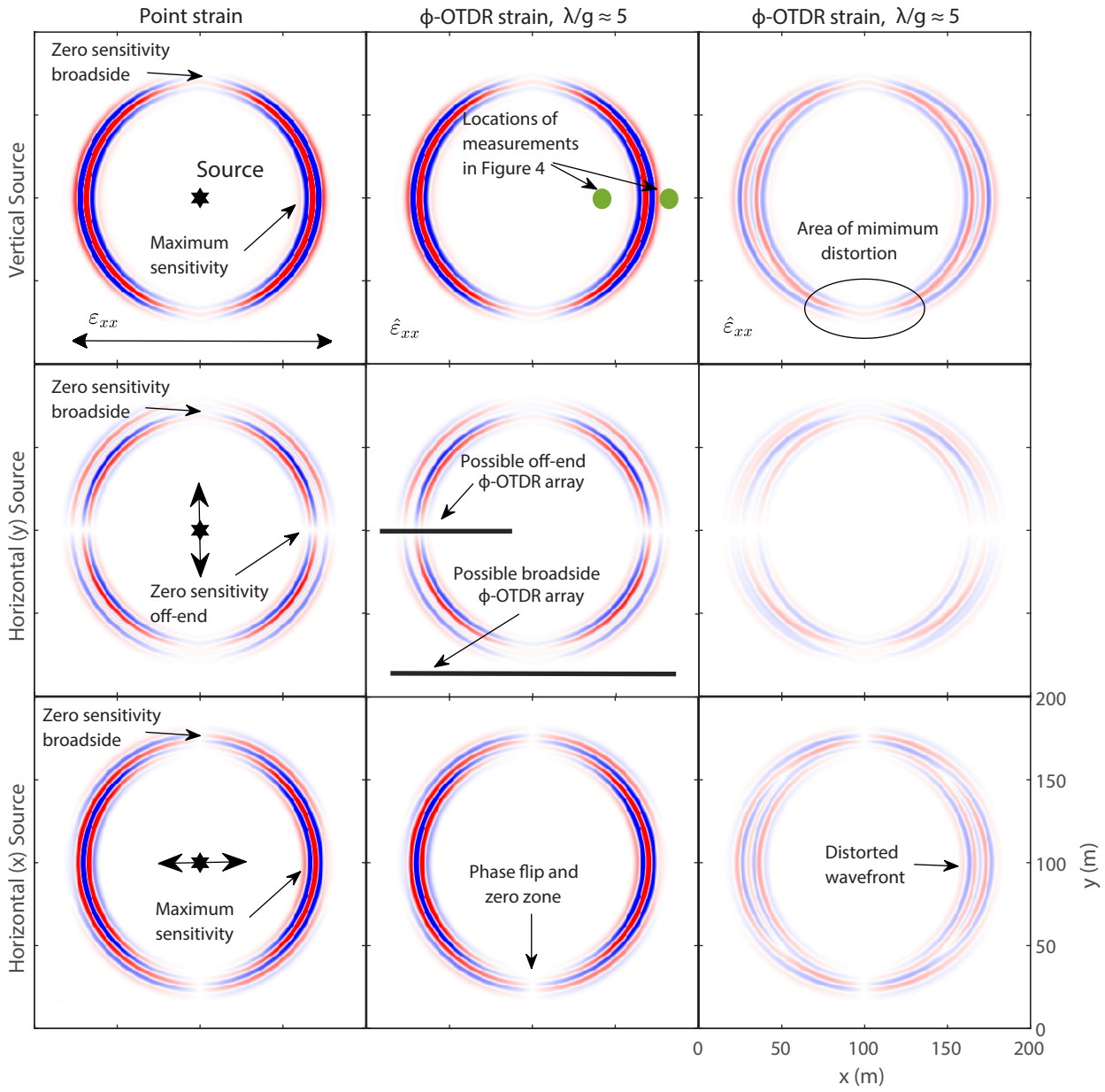

Figure 3.3: Simulations of normalized pointwise (ε_{xx}) and distributed ($\hat{\varepsilon}_{xx}$) strain in the x-direction at the top surface of a 200 m by 200 m by 100 m elastic half-space model caused by a 100 kN force. The strain is shown as measured by an ideal distributed strain sensing system aligned in the x-direction with wavelength-to-gauge length ratios (λ/g) of 5 and 1. This is approximately what ϕ-OTDR would measure neglecting effects from the pulse shape and cable transfer functions. Each source with horizontal polarization began their Ricker wavelet source signal in the positive x or y- direction. The source is shown centered in the model to demonstrate the theoretical pointwise strain and corresponding distributed measurements at all angles. All tiles are normalized relative to the maximum strain across all simulations. The simulations were conducted using Seismic Waves 4th Order [139].

The reception patterns for pointwise strain and distributed strain are evident in the simulation results, including zero sensitivity to perfectly broadside (90° or 270°) sources in the vertical and both horizontal directions. These zero sensitivity zones are labelled in the pointwise strain simulation results. An off-end source-receiver orientation would result in maximum sensitivity to the vertical or x-direction horizontal source, which are also labelled, while there would be no sensitivity to the y-direction horizontal source. It is important to note the phase-flips that occur for the broadside orientation of the x-direction source and the off-end orientation for the y-direction source. This observation is similar to the observations made by Luo et al. [141] of broadside microseisms measured by downhole ϕ-OTDR. This results in strain with an opposite sign being measured depending on what side of this phase-flip the receiver is on. This will be evident later in the field-acquired data.

The wavefields are captured well by the approximate ϕ-OTDR data for the case of $\lambda/g \approx 5$. The wavefronts have a significantly lower amplitude and become distorted when $\lambda/g \approx 1$. This is most evident for the y-direction horizontal source. Importantly, the distortion diminishes toward the broadside source-receiver orientation, which is labelled in the top-right tile. This observation is consistent with Equations 3.29 and 3.30, and Figure 3.2 that demonstrate that the ratio of distributed strain to pointwise strain approaches one for angles near $\theta = 90°$ and 270° degrees regardless of λ/g.

The amplitude distortion caused by low λ/g values is shown in Figure 3.4. Strain simulated by the off-end source-receiver orientation for the vertical source is shown at offsets of 40 and 80 m. The location of these receivers is also indicated in the top-center tile of Figure 3.3. The $\lambda/g \approx 5$ case is very close of the pointwise strain amplitude. The measured amplitude diminishes for the $\lambda/g \approx 2.5$ case before becoming completely distorted for $\lambda/g \approx 1$. This follows with Equation 3.9 which describes the gauge length of ϕ-OTDR as a filter in the wavenumber domain. For a monochromatic plane wave solution, the $\lambda/g \approx 1$ case would result in zero strain measured (see [125]); the strain is non-zero because the source Ricker wavelet has a non-finite bandwidth. This result is important because it indicates how ϕ-OTDR arrays will fundamentally respond to the most common active source and geometry, the off-end hammer strike. Due to the wide bandwidth of the wavelet generated by an impulse signal like a hammer or weight drop, the ability for ϕ-OTDR to adequately measure the pointwise strain field is a function of λ/g. This can be mitigated if either the user quantifies the amplitude reduction due to the λ/g ratio (i.e. using Equation 3.9) for the particular application or, preferably, examines the spatially differenced displacement field as the desired quantity in their forward modelling of a problem. For example, Titov et al. [142] forward-modeled ϕ-OTDR data directly using the spatial difference method for a VSP-type ϕ-OTDR deployment and gained insights for interpreting field data. Since the finite difference is a very simple operation to conduct, it provides a straightforward way to compare ϕ-OTDR and modeled data especially for a deployment where subsurface quantities are known.

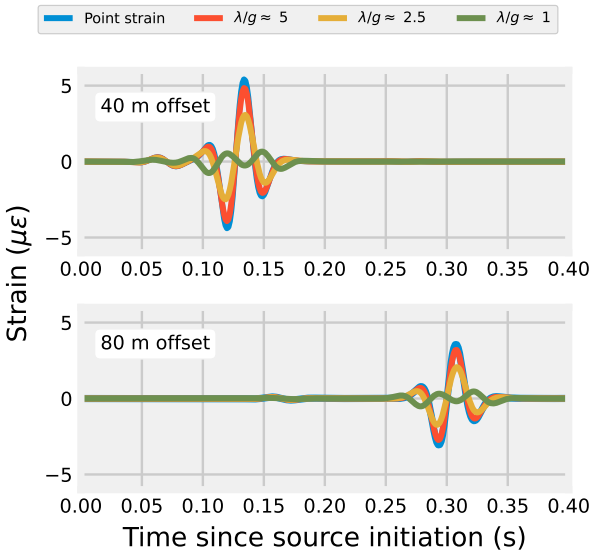

Figure 3.4: Simulations of ideal distributed strain at the top surface of an elastic model at offsets of 40 and 80 m caused by a 100 kN force in vertical direction. Wavelength-to-gauge length ratios of 1, 2.5 and 5 relative to the Rayleigh wavelength are shown for a virtual ϕ-OTDR array extending radially away from the source position. The simulations were conducted using Seismic Waves 4th Order [139].

3.6 Experimental Campaign

An experiment was conducted at the NHERI@UTexas [143] Hornsby Bend test site in Austin, TX to compare active source seismic strain signals recorded simultaneously using ϕ-OTDR and geophones. An overhead view of the test setup is shown in Figure 3.5. The test used a 94 m-long geophone array (48 geophones at 2 m spacing) directly above two different 200 m-long fiber optic cables buried in a shallow trench. The cables were installed carefully to ensure good coupling with the ground.

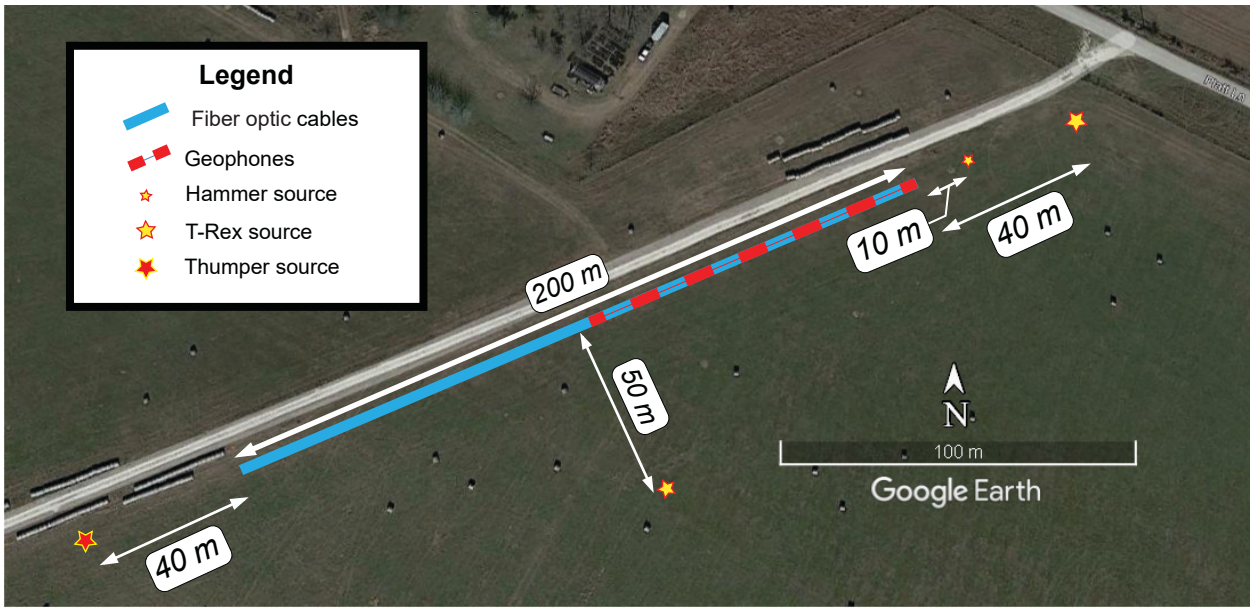

Figure 3.5: Plan view of the experimental setup at the Hornsby Bend test site along Platt Lane in Austin, TX, USA, where a 94 m geophone array and two 200 m ϕ-OTDR arrays (NanZee and AFL cables) were installed at the same location. The geophones were spaced at 2 m and the gauge length of the ϕ-OTDR system was 2.04 m. The two different ϕ-OTDR cables were spliced together at the far end of the array and interrogated simultaneously. The T-Rex and Thumper vibroseis trucks were used to vibrate the ground 40 m from the arrays in an off-end configuration. T-Rex was also used 50 m from the arrays in a broadside configuration. A sledgehammer was used to strike the ground vertically 10 m from the arrays in an off-end configuration.

The cable installation process is shown in Figure 3.6(a-c). First, the end points of the trench were surveyed with a total station and a line was pulled tight to mark the position of the trench. Next, a trenching machine was used to excavate a 10-15 cm deep trench along the marking line (Figure 3.6(a)). Once the trench was excavated, the cables were placed side-by-side at the bottom of the trench (Figure 3.6(b)). The trench was then backfilled using the same volume of soil that was removed. A skid-steer loader was used to push the soil into the trench and then driven on top to compact the soil (Figure 3.6(c)).

Two fiber optic cables cables with tightly buffered fibers were used for ϕ-OTDR arrays. One was NanZee Sensing Technology's NZS-DSS-C02 (Figure 3.6(d)), and the other was AFL's X3004955180H-RD (Figure 3.6(e)). Note that tight buffering only refers to the layer directly outside the optical fiber [144], such that a polymer coating was applied directly to each individual fiber. Outside of that tight buffer the construction can vary widely from one cable design to another. The NanZee cable has a layer of steel braid that is wound securely around a single tight buffered fiber, which is then encased in a polyethylene jacket. The AFL

cable, in contrast, has a layer of aramid yarn surrounding four tight buffered fibers encased in a polyurethane jacket.

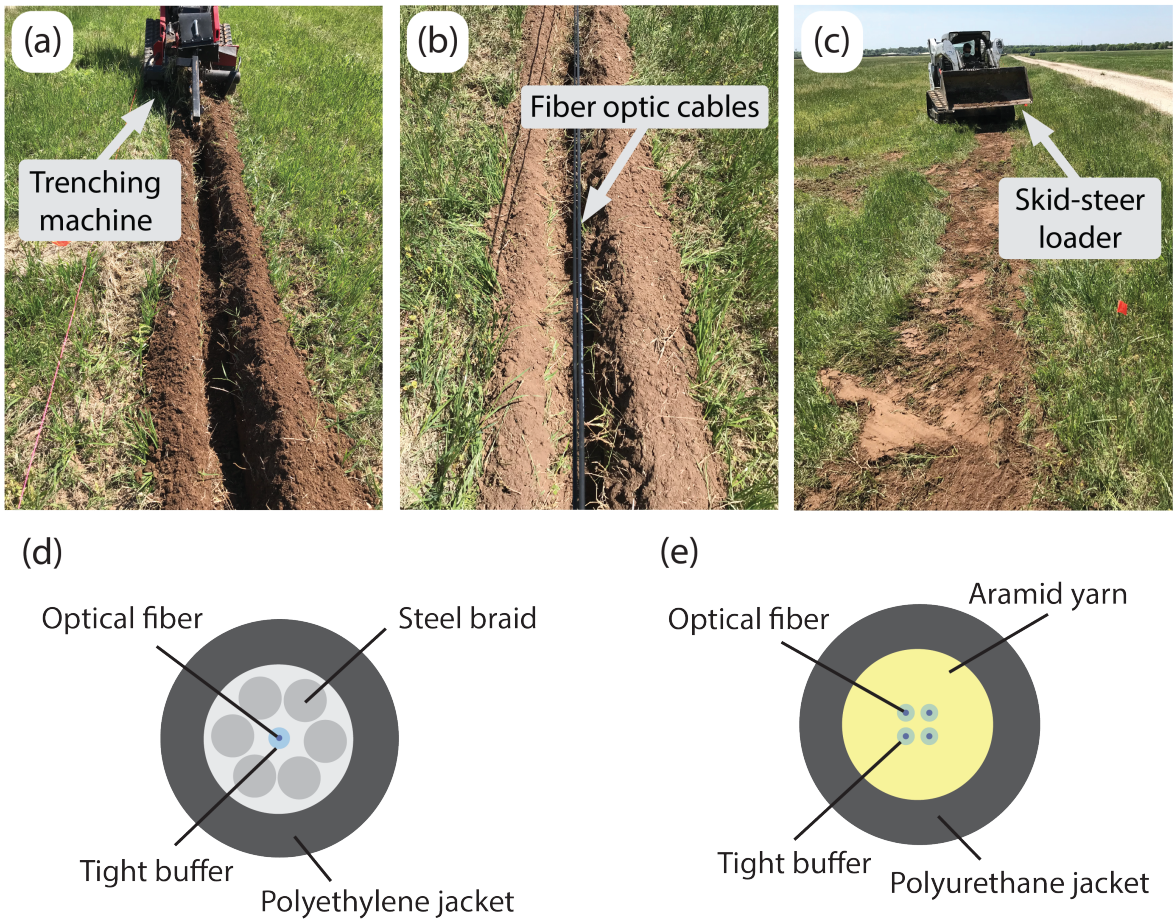

Figure 3.6: The fiber optic cables were tightly coupled with the ground by: (a) using a trenching machine to excavate a trench between 10 and 15cm deep, (b) placing the two cables within the trench next to each other, and (c) backfilling and compacting the trench with a skid-steer loader to ensure the soil was densified around the cables. The two installed cables were (d) NanZee Sensing Technology's NZS-DSS-C02 and (e) AFL's X3004955180H-RD.

The cables were fusion spliced together inside a junction box so that they could be simultaneously interrogated using a single ϕ-OTDR interrogator unit (IU), which for this study was an OptaSense ODH-4. One end of the cables was brought into an instrumentation trailer that housed the IU, geophone data acquisition systems, and vibroseis control electronics. The other end was terminated to reduce end-reflections by fusion splicing on an E2000-style connector and propping open the connector cover so light could escape. The OptaSense ODH-4

IU was configured to have a gauge length of 2.04 m, a channel spacing of 1.02 m, and a pulse repetition rate of 100 kHz for the majority of the acquisition. Gauge lengths of 4.08- and 8.16 m were also used for a few shot records that are used in this study to quantify the value of a smaller gauge length in Section 3.8. Due to the demodulation scheme used by the ODH-4, which determines the optical phase over four consecutive pulse repetitions, the 100 kHz pulse rate produces a sensing bandwidth of 12.5 kHz. The ϕ-OTDR data was downsampled in real-time to 1 kHz, which involved the application of an anti-aliasing filter and decimating the time series. The downsampling process was handled by the acquisition software provided with the IU. The horizontal geophones used were Geospace Technologies GS-11D with a fundamental frequency of 4.5 Hz. The geophones were housed in PC21 land cases with 7.6 cm aluminum spikes. They were oriented horizontally along the direction of the ϕ-OTDR cables (i.e., in-line) for direct comparison to the ϕ-OTDR data. There were 48 geophones spaced at 2 m for a total array length of 94 m. The geophones were connected to two 24-channel Geometrics Geode seismographs. Geophone measurements were also collected at 1 kHz.

One week after cable installation seismic waves for the study were generated by three different sources: the NHERI@UTexas vibroseis trucks T-Rex and Thumper and a sledgehammer. Wavefields generated by the seismic sources were recorded simultaneously by the ϕ-OTDR and geophone arrays. Figure 3.5 shows the geometry of the acquisition. T-Rex was used to vibrate the ground vertically as well as in both horizontal directions 40 m from the arrays in an off-end configuration, and 50 m from the arrays in a broadside configuration. T-Rex produced a linear chirp vibration from 3 to 80 Hz lasting 12 s. Thumper was used to vibrate the ground vertically 40 m from the arrays in an off-end configuration but with a linear chirp from 5 to 200 Hz also lasting 12 s. The maximum output forces created by T-Rex and Thumper during their vibrations were 267- and 27 kN, respectively [143]. A sledgehammer was also used to generate seismic signals by striking the ground vertically at 10 m from the arrays in an off-end orientation. Note that this is only a subset of the total data acquisition which included different source orientations and locations. Other studies including Vantassel et al. [125] have used this dataset, and much of the data is publicly available on DesignSafe-CI [145].

3.7 Experimental Evaluation of ϕ-OTDR Reception Patterns

First, the ϕ-OTDR-recorded measurements are presented qualitatively to examine the impacts of ϕ-OTDR reception on signal characteristics. As discussed later, both cables were of sufficiently high quality and good coupling such that the cable choice made little difference in signal measurement, so only the NanZee cable is shown in this section. Figure 3.7 shows seismic recordings from the NanZee cable ϕ-OTDR array using a 2.04 m gauge length during vibrations from T-Rex cross-correlated with the input source sweep signal.

This cross-correlation results in a zero-phase source wavelet with center frequency of 41.5 Hz. The data is shown for both off-end and broadside configurations of the vertical and both horizontal directions of excitation using the T-Rex vibroseis source. The ϕ-OTDR array is oriented in the x-direction, which is labeled on the horizontal axis. The data is shown normalized relative to the maximum amplitude across all the records for straightforward comparison.

The off-end configurations (the left tiles in Figure 3.7) give maximum signal amplitude for the vertical source and horizontal source oscillating in-line with the x-direction. The horizontal and vertical source orientations create predominantly Rayleigh waves propagating between 250- and 500 m/s with frequencies from 6-30 Hz. An SV headwave is also discernible travelling at approximately 600 m/s with a frequency less than 80 Hz. As expected from the simulations presented in Figure 3.3, the y-direction horizontal source in the off-end orientation produces a much smaller signal received on the ϕ-OTDR array, though there is a slight sensitivity to what is thought to be a fundamental mode Love wave with velocities from 180-350 m/s and frequencies from 8-25 Hz. This sensitivity may be due to imperfect alignment of the horizontal y-direction source with respect to the array. As demonstrated in Figure 3.2 the sensitivity to Love and SH waves picks up abruptly as the angle deviates from 0° or 180°.

For the broadside source position (the right plots in Figure 3.7), the reception patterns of ϕ-OTDR are more obvious. All three source directions cause a minimum signal reception where the angle of incidence is 270°. However, as shown from the simulations presented earlier, only the horizontal source excited in-line with the x-direction sees a phase-flip at the 100 m location. The vertical source induces several modes of Rayleigh waves as well as an SV headwave. The y-direction horizontal source creates Rayleigh waves directly perpendicular to the source that transition to Love waves at farther offsets. The opposite is true for the x-direction horizontal source, which creates Love waves perpendicular to the source that transition to Rayleigh waves. There is also a distinct headwave observed in the y-direction horizontal source data that may be an SH-type headwave. From visual examination, wavelengths across all vibrations range from approximately 6 - 80 m indicating that the smallest λ/g value is about 3. However, a more quantitative method for estimating λ/g is proposed next.

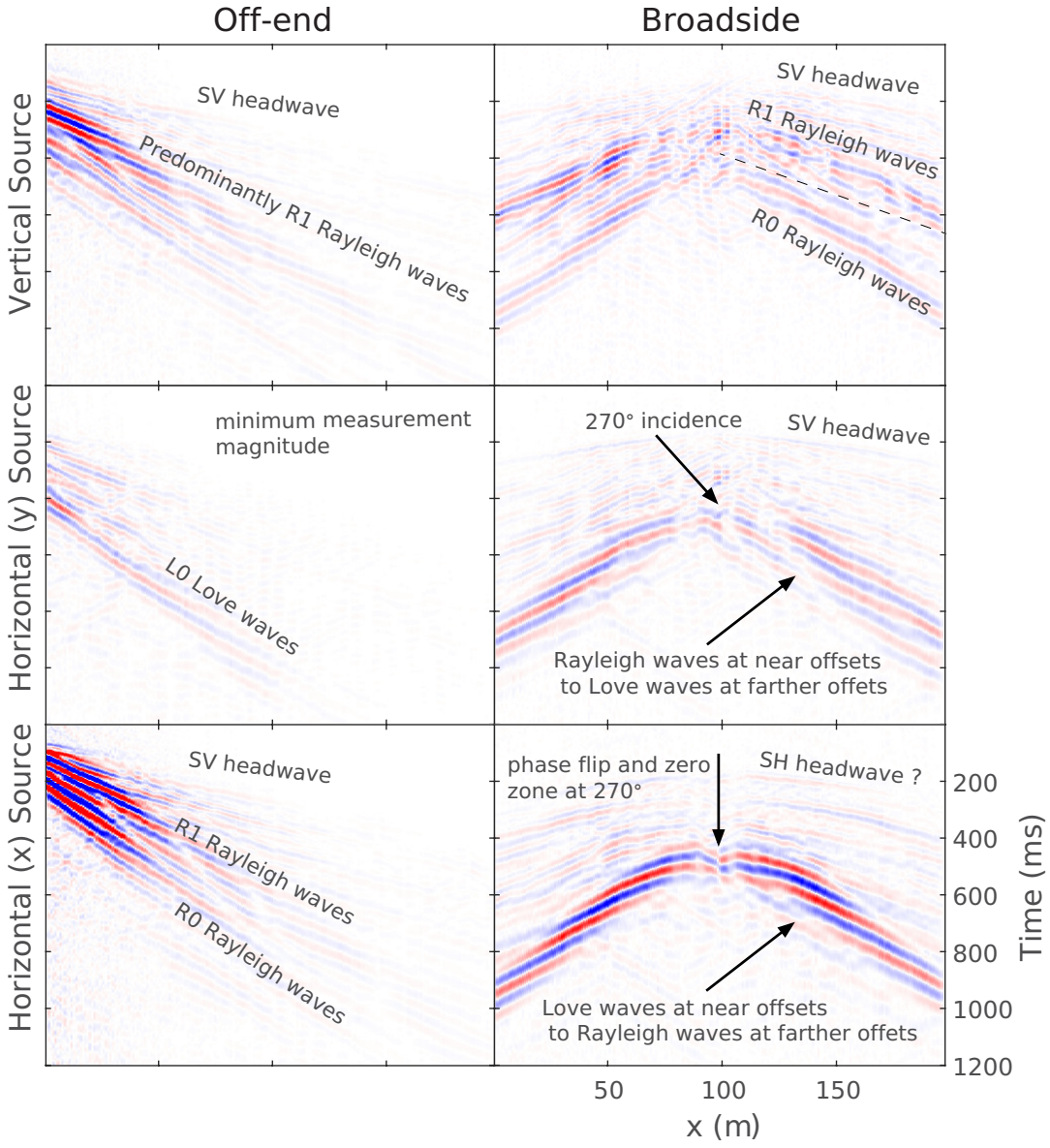

Figure 3.7: Experimental results using the NanZee cable ϕ-OTDR array of testing the angular reception pattern of ϕ-OTDR subject to active source vibration in both off-end and broadside configuration for vertical and both horizontal directions of excitation using the T-Rex vibrosies source. The ϕ-OTDR array is oriented in the x-direction. The off-end geometry is 50 m from the beginning (x=0) of the ϕ-OTDR array, and the broadside configuration is 50 m perpendicular from the midpoint of the 200-m-long ϕ-OTDR array.

3.8 Estimating Wavelength-to-Gauge Length Ratio for Field Data

In this section vibrations from the Thumber vibroesis truck are used to estimate the λ/g values experienced at the test site for a wide bandwidth (5 - 200 Hz) signal and various gauge lengths. Figure 3.8 shows three source-correlated strain wavefield measurements made during 5-200 Hz vibroseis sweeps using gauge lengths of 2.04-, 4.08-, and 8.16 m from left to right. The center row shows the 2-D Fourier ($f-k$) transform of each correlated set of measurements relative to the maximum power in the $g = 2.04$ m case. The bottom row shows f as a function of λ/g by remapping the $f-k$ transform.

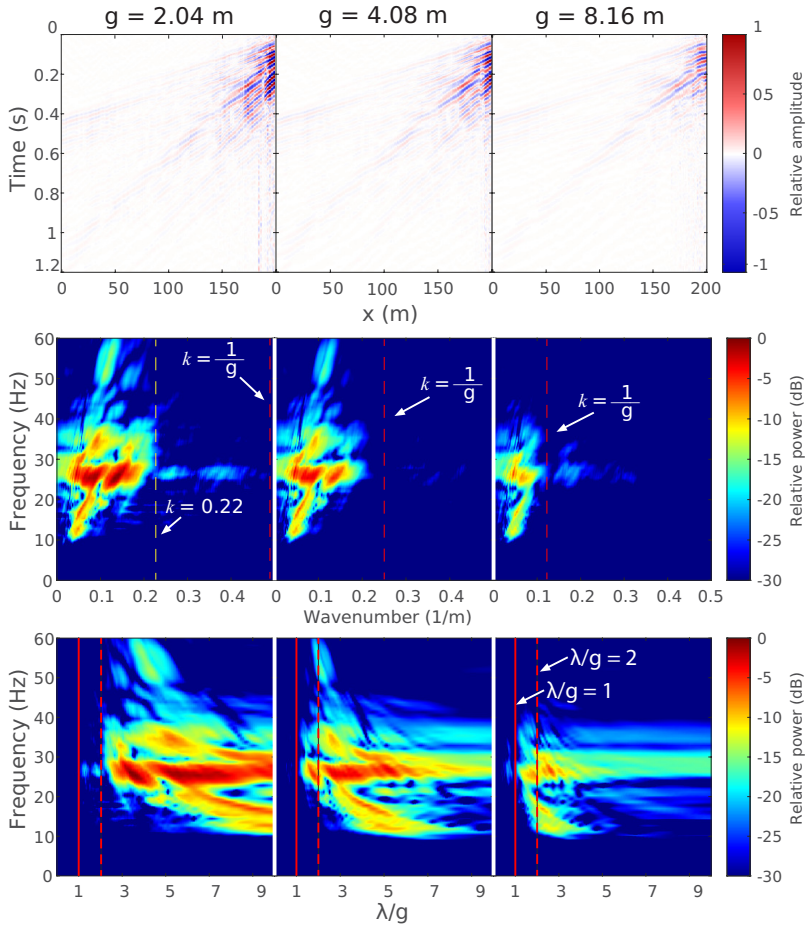

Figure 3.8: (Top) Source-correlated wavefields generated by the Thumper vibroseis truck 40 m from the ϕ-OTDR arrays in the off-end configuration recorded using the NanZee cable and using different gauge lengths of 2.04-, 4.08- and 8.16 m; (Center) The $f-k$ transforms of the recorded wavefields; (Bottom) The remapped $f-k$ transforms as a function of λ/g.

This type of data visualization allows for the identification of signal power relative to λ/g to assess the data quality for strain quantification. Figure 3.8 shows that the signal power when $g = 2.04$ m is almost entirely above $\lambda/g = 2$. Whereas when $g = 4.08$ m or 8.16 m the signal power extends lower in λ/g until it abuts the $\lambda/g = 1$ line. There is not expected to be much power below $\lambda/g = 1$ due to attenutation, but proximity to the $\lambda/g = 1$ line acts as an indicator for where the signal energy occurs. Even so, a $\lambda/g = 2$ value is not ideal and only results in measuring 63% of the strain amplitude. This can be estimated using Equation 3.9 for the case of $g = 2.04$ m and $\lambda = 4.08$ m as:

$$\mathbb{G}(\frac{1}{4.08\text{ m}}) = \frac{\sin\left(\pi \frac{1}{4.08\text{ m}}(2.04\text{ m})\right)}{\pi \frac{1}{4.08\text{ m}}(2.04\text{ m})} = 0.63 \tag{3.32}$$

However, most of the signal power seems to be above $\lambda/g = 3$, which corresponds to 83% of the strain field. Depending on the accuracy desired by a practitioner, acceptable λ/g values may vary.

3.9 Comparison of Strain Measurements from ϕ-OTDR and Geophones

In this section, geophones are used to verify the amplitude of the strain measurements made with ϕ-OTDR. The first processing step of processing the ϕ-OTDR data is to mitigate the laser frequency drift and temperature-induced variation at low frequencies. To do so, a 3 Hz high pass filter was applied to the raw ϕ-OTDR phase measurements and then the measurements were converted to strain using Equation 2.28. The geophone measurements were converted from the raw form to particle velocity by compensating for their frequency dependent response as described in Equation 3.19. Next, the velocity time-series were integrated to achieve units of displacement and the finite difference was applied to the displacement measurements. This is the process described in Equation 3.28. Then, a ϕ-OTDR channel at about the same location as the center of a differenced geophone pair was selected for comparison.

3.9.1 Uncertainty in ϕ-OTDR Channel Location

The result when T-Rex vibrated the ground 40 m from the array in the off-end configuration is shown for six different ϕ-OTDR channels and differenced geophone pairs in Figure 3.9. For a clear view of the waveforms, 0.25 s of data are shown from 1.50 – 1.75 s into the 12 s long, 3-80 Hz vibroseis chirp. The amplitudes of both ϕ-OTDR cable measurements match well to the amplitudes of the spatially differenced geophone measurements.

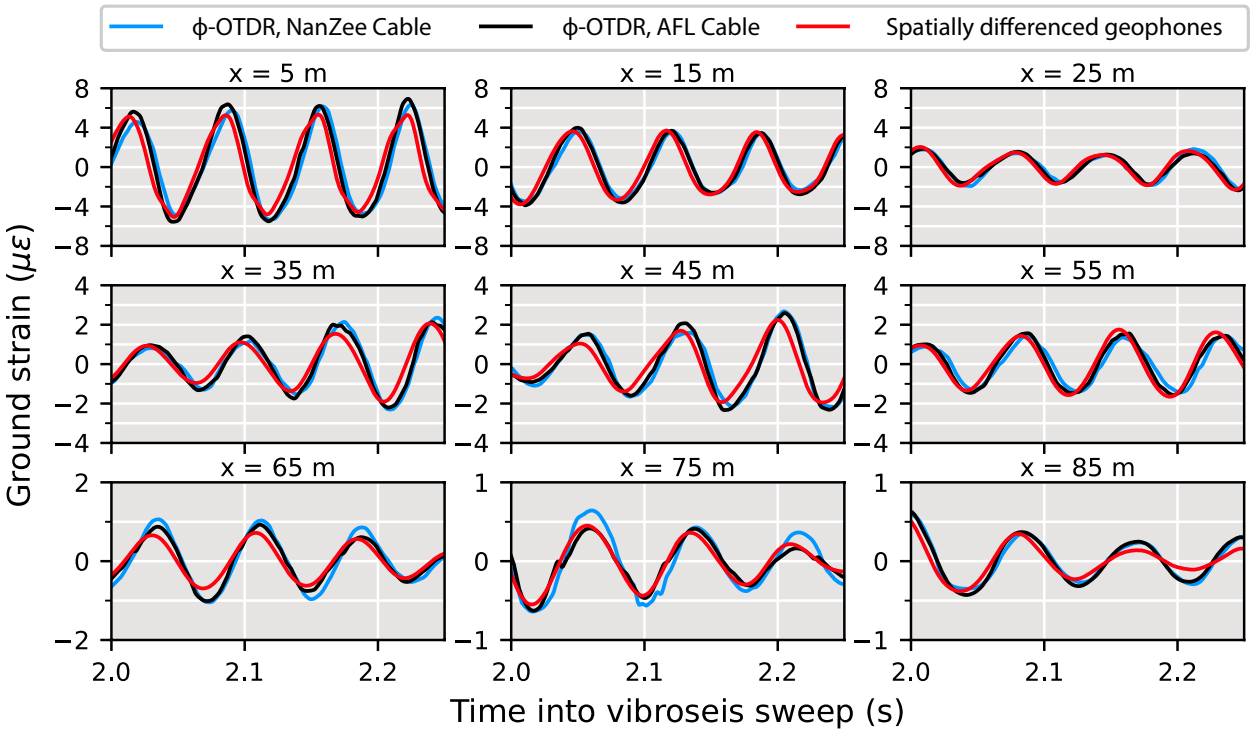

Figure 3.9: Temporal comparison before shifting of average strain measured with ϕ-OTDR on both the NanZee and AFL cables with geophone strain measurements during in-line shaking by T-Rex 40 m from the array in the off-end configuration performing a 12-second, 3-80 Hz chirp. Each geophone used for strain calculation (differencing) was close to the locations of the scattered optical pulses, but not perfect (see Figure 3.10). The position indicated is the point between the two differenced geophones (i.e. 75 m indicates the data from subtracting the geophone at 74 m from the one at 76 m).

There is a slight phase difference (i.e., time shift) between the time series for all locations, as shown in Figure 3.9. This is consistent with the phenomena observed by Wang et al. [109] and Egorov et al. [127]. This phase difference is due to the uncertainty associated with the ϕ-OTDR measurement location relative to the geophone positions. As shown in Figure 3.10, when a ϕ-OTDR system is operated, the sensing fiber is interrogated at a fixed spatiotemporal frequency determined by the digitizer of the ϕ-OTDR system. The measurement channels are evenly spaced but the exact position is hard to determine. Often a 'tap-test' is performed by tapping at a known location and examining what ϕ-OTDR channels respond. However, this is only able to locate the measurement point with a certainty of the gauge length of the ϕ-OTDR system (i.e., +/- one half of a gauge length). Therefore, it is expected that there will be a slight shift in the measurement location between colinear ϕ-OTDR and geophone arrays even when a tap-test is performed.

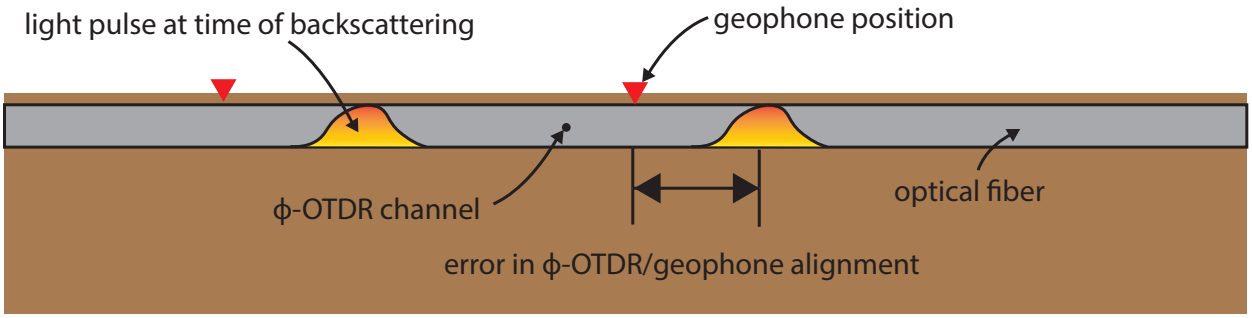

Figure 3.10: Schematic of the spatial uncertainty of the location of ϕ-OTDR channels in relation to a geophone on the ground surface for a linear ϕ-OTDR array. It is not possible to perfectly locate the scattering positions in ϕ-OTDR arrays so there will be error between ϕ-OTDR and geophone positioning.

3.9.2 Correcting Spatial Offset between Geophones and ϕ-OTDR

A method for aligning ϕ-OTDR channels with spatially differenced geophone measurements is proposed here. The method includes spatially up-sampling the ϕ-OTDR data using Fourier method interpolation [23] so that synthetic ϕ-OTDR channels exist every 1 cm along the array. Then, the spatially up-sampled ϕ-OTDR channels are compared to the geophone measurements. This is done by comparing each 1 cm-spaced synthetic ϕ-OTDR channel in the vicinity of a geophone pair with the spatially differenced time-series from that pair. The time series from both ϕ-OTDR and geophones are normalized by their two-norm and then the sum of the square error at each time sample is taken as the misfit m_x. The minimized value achieves relative alignment between the scattering locations used for ϕ-OTDR and the geophones. The misfit is described by:

$$m_x = \Sigma_{j=1}^{\mathbf{n}} \left(\frac{\hat{\varepsilon}_{\phi-OTDR,x}[j]}{\|\hat{\varepsilon}_{\phi-OTDR,x}\|_2} - \frac{\hat{\varepsilon}_{geo}[j]}{\|\hat{\varepsilon}_{geo}\|_2} \right)^2 \tag{3.33}$$

where $\hat{\varepsilon}_{\phi-OTDR,x}$ is the time-series of ϕ-OTDR data at location x of length $\mathbf{n}$ points, $\hat{\varepsilon}_{geo}$ is the time-series defined by a spatially differenced geophone pair, and m_x is the misfit calculated for that ϕ-OTDR time-series and geophone pair.

Figure 3.11(a) shows an example of how this procedure works using the NanZee cable data from the vertical T-Rex shake 40 m from the array in the off-end configuration. The magenta traces are the first 20 ϕ-OTDR traces spaced at 1.02 m which is the default trace separation of the ODH-4 IU. The grey variable density image behind the traces is the interpolated wavefield sampled every 1 cm in space. The red traces are shifted to minimize the misfit described by Equation 3.33 between the ϕ-OTDR and geophone measurements while being constantly spaced at 1.00 m. This process simultaneously corrects for the mismatch in the geophone/ϕ-OTDR channel positions and spacing. Figures 3.11(b) and 3.11(c) show the

minimization result relative to the position of the first ϕ-OTDR trace in the array for 40 ϕ-OTDR traces and geophone pairs. The results show that the estimated locations of the NanZee cable's first ϕ-OTDR trace was offset from the geophone positions by about 77 cm, while the AFL cable's array was offset by about 30 cm. This offset is random, and the AFL cable array just happened to be in better alignment with the geophones. The corresponding new 1.00 m spaced, interpolated ϕ-OTDR channels can be selected to create a shifted ϕ-OTDR array that resolves the phase mismatch with the geophones observed previously (recall Figure 3.9). It is important to note that the spatial interpolation can only be considered valid for wavelengths larger then twice the trace separation, 2.04 m in this case, based on the Nyquist-Shannon sampling theorem.

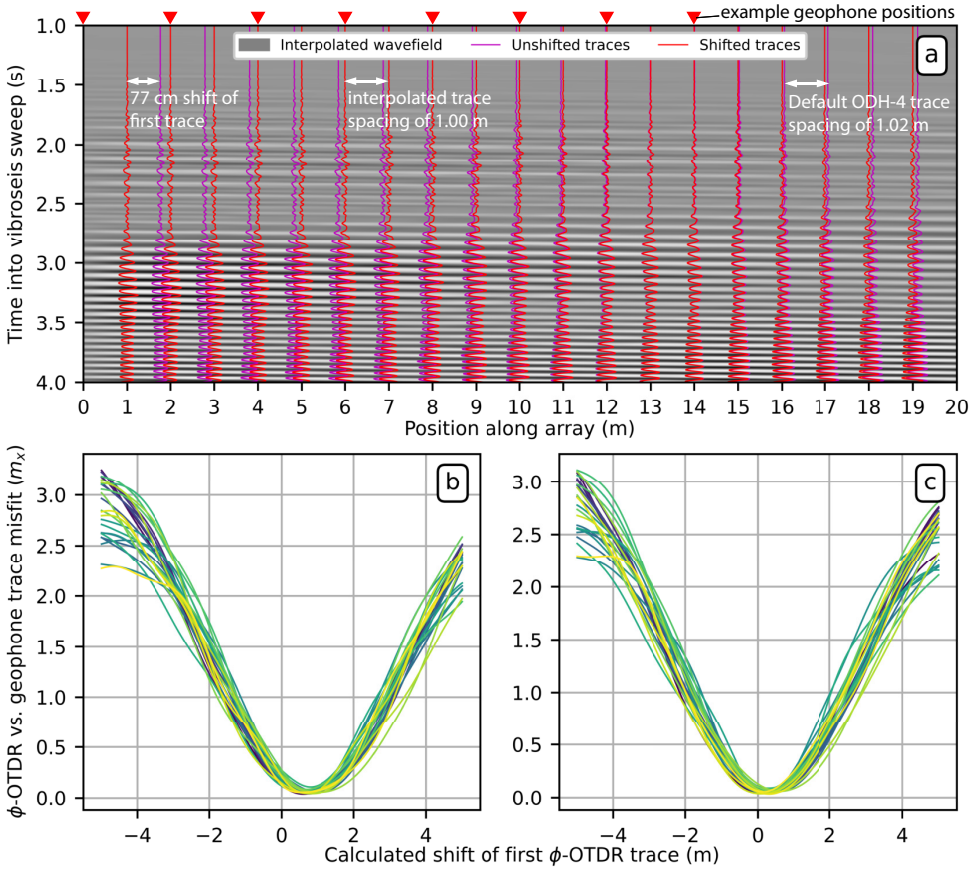

Figure 3.11: (a) Demonstration of the proposed method to align ϕ-OTDR arrays in space with geophones using the NanZee cable array and data from the vertical T-Rex shake 40 m from the array in the off-end configuration. The measured wavefield (magenta traces) is upsampled in space using Fourier interpolation to 1 cm trace separation and shown as the grey variable density background. Each 1 cm-spaced trace is compared to geophone-calculated strain data where the position of the discrete geophones is known. The new 1.00 m spaced set of ϕ-OTDR traces that minimize the misfit between the ϕ-OTDR and geophone measurements are selected (red traces) creating a ϕ-OTDR array where the position of each trace is known. (b) and (c) show the minimization result for the relative position of 40 ϕ-OTDR traces relative to geophone pairs for the NanZee and AFL cables, respectively. The green colors are different ϕ-OTDR trace/geophone measurement comparisons shown relative to the shift of the first ϕ-OTDR trace in the arrays. It is necessary to make comparisons relative to the shift of the first trace because the arrays have different spacing (1.02 m vs. 1.00 m), which is ultimately resolved in the interpolation process.

3.9.3 Vibroseis Truck Shaking

Measurements from the 77 cm shifted NanZee cable and 30 cm shifted AFL cable ϕ-OTDR arrays are compared with the spatially differenced geophones in Figures 3.12 for a T-Rex vibroseis chirp. The figure shows 0.5-6 s from the time the vibration was triggered at various locations along the array. The amplitude and phase measurements made by ϕ-OTDR are consistent with the measurements made by the geophones. The ϕ-OTDR data measured using both cables tends to have slightly higher amplitudes than the geophone records at near offsets.

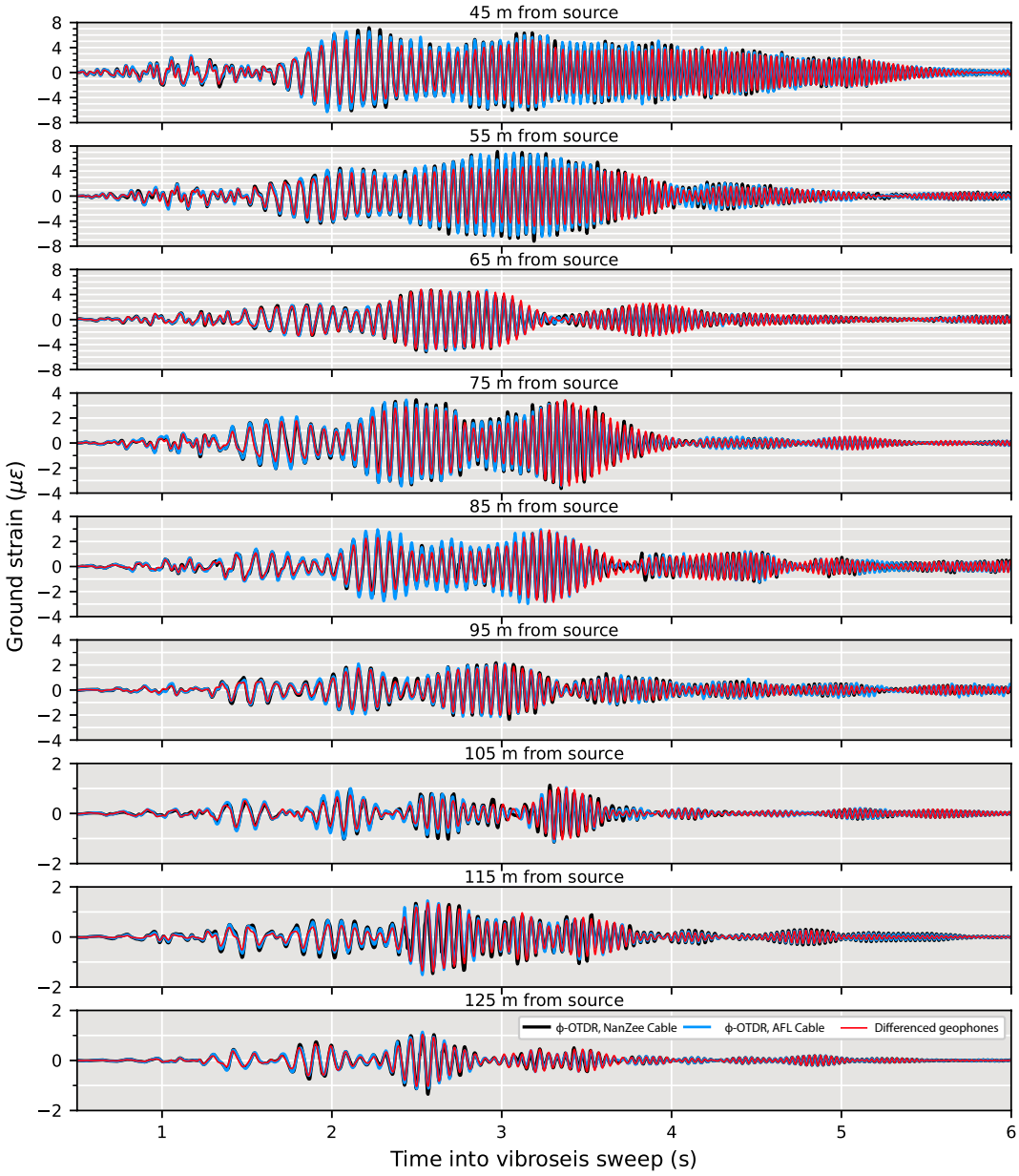

Figure 3.12: Spatially shifted ϕ-OTDR and geophone data comparisons in units of strain during 0.5-6s of vertical shaking by the T-Rex shaker truck at a position of 40 m from the array in the off-end configuration performing a 12-second, 3-80 Hz chirp. The ϕ-OTDR data has been spatially shifted from its positions in Figure 3.9 using the presented Fourier interpolation procedure to match up with the geophone data (77 cm for the NanZee cable and 30 cm for the AFL cable). The distance indicated is the point between the two spatially differenced geophones along the array.

To gain a more comprehensive picture of the comparison, the time series are visualized by their power spectra. The power spectra shown in Figure 3.13 are for the ϕ-OTDR and spatially differenced geophones centered at the same locations, as shown in Figure 3.12 for the frequency range of 3-100 Hz. The noise floor is also displayed for each. The noise floor was determined by taking the power spectrum of the signals during a quiet period when no shaking was happening. The ϕ-OTDR datasets show slightly higher signal power than the geophones across the frequency band, with the ϕ-OTDR showing significantly larger power above 45 Hz. The signal power difference at high frequencies is attributed to phase determination errors and will be explored further later in this section.

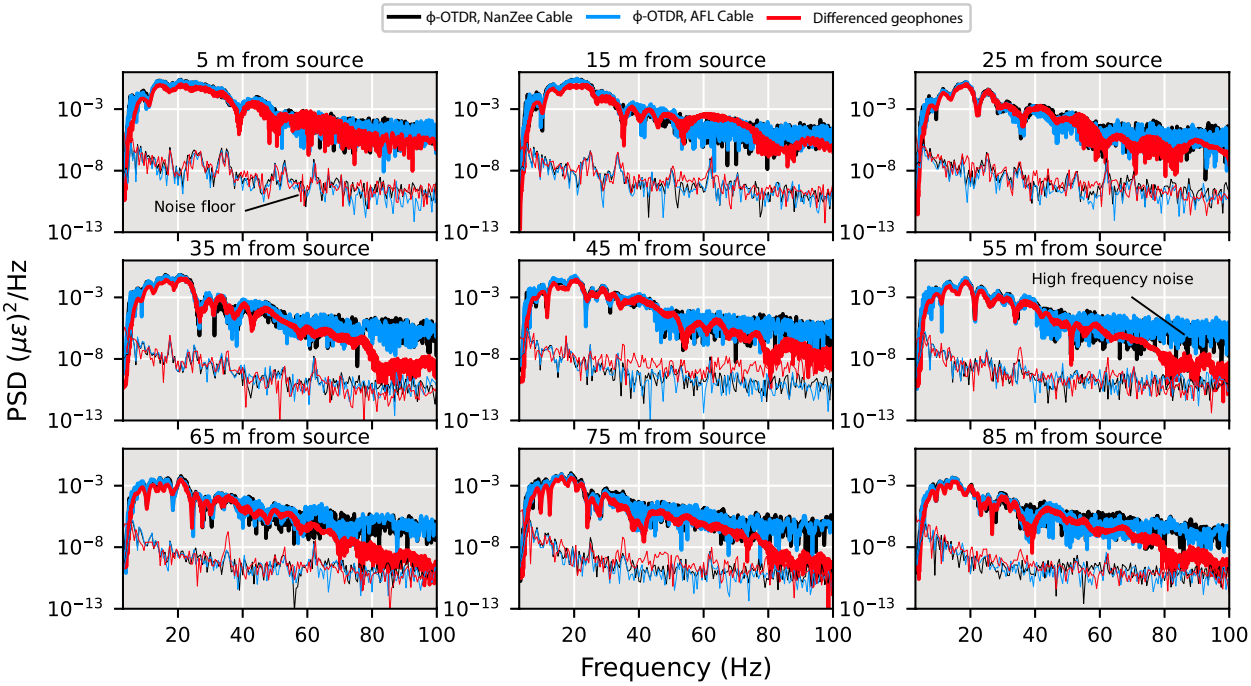

Figure 3.13: Power spectra of ϕ-OTDR and geophone data comparisons during vertical shaking by the T-Rex shaker truck at a position of 40 m from the array in the off-end configuration performing a 12-second, 3-80 Hz chirp. The noise floor for each ϕ-OTDR cable and the geophones has been calculated from 2 s of quiet time following the vibration.

3.9.4 Sledgehammer Shot

The ϕ-OTDR and geophone-measured strain from a vertical sledgehammer striking the ground at 10 m from the arrays is presented in Figure 3.14. The traces in Figure 3.14 have been spatially shifted by the same amount as in Figure 3.12. The measurements are shown for a single sledgehammer strike 0-1 s after impact. The geophone and ϕ-OTDR measurements agree well across the entire array from the hammer strike, indicating that

ϕ-OTDR is a viable tool for not only measuring high amplitude vibroseis induced ground shaking but also the less energetic and more traditionally used sledgehammer.

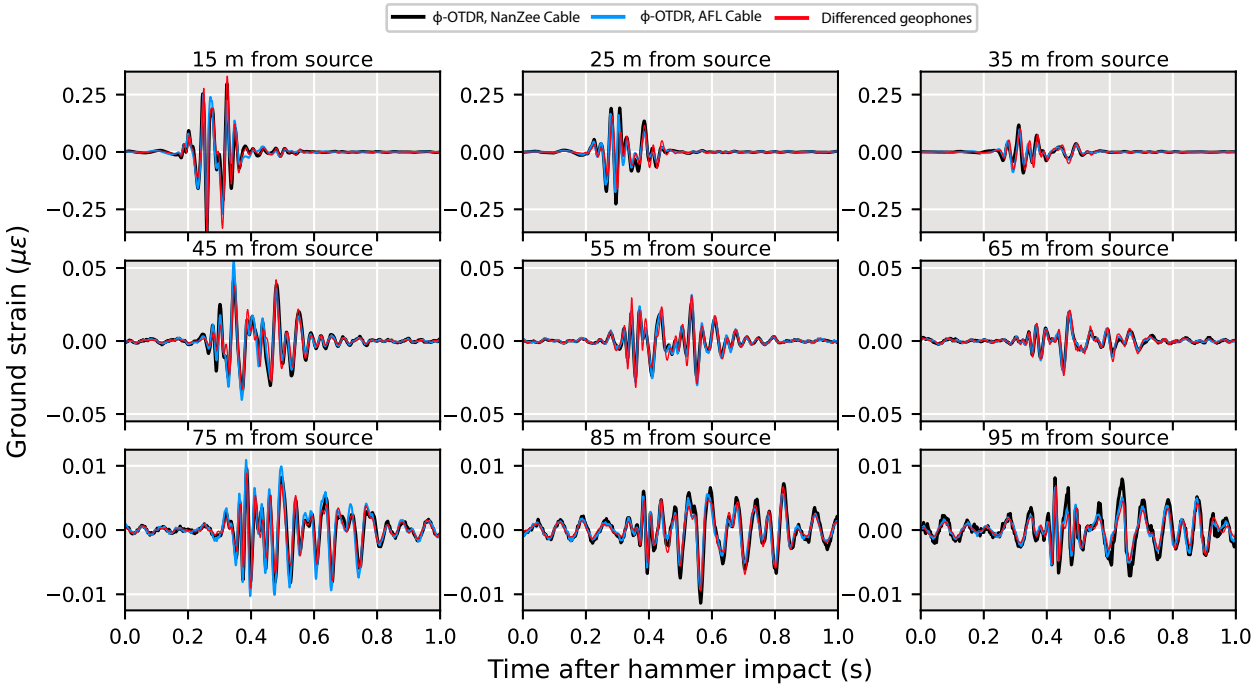

Figure 3.14: Spatially shifted ϕ-OTDR and geophone data comparisons in units of strain during a vertical sledgehammer strike 10 m from the array. The ϕ-OTDR data has been spatially shifted using the procedure shown in Figure 3.11 to align with the geophone data. The distance indicated is the point between the two spatially differenced geophones along the array.

3.9.5 Remarks on Noise in ϕ-OTDR Measurements

Examining the power spectra of the ϕ-OTDR when recording an active source and during quiet time can be a misleading representation of the system's signal to noise ratio. There is an aspect of ϕ-OTDR system noise that is caused by signals that change faster than the phase can be measured, referred to here as phase determination error. This can be thought of as the ϕ-OTDR version of clipping. As introduced in Equation 2.27, the The maximum phase rate ($d\dot{\phi}_{max}$) of a ϕ-OTDR system is determined by the system's ability to unwrap the circular phase measurements. For the ODH-4 there is four-wavelength diversity processing (see Section 2.3.2), so an effective sample happens once every four pulses. Therefore using Equation 2.27 it can be described:

$$d\dot{\phi}_{max} = \pi \frac{f_p}{8} \tag{3.34}$$

where f_p is the pulse rate of the ODH-4. Equation 2.27 is stating that the phase cannot change more than $\frac{\pi}{2}$ radians per sample or the phase measurements cannot be correctly unwrapped. The ODH-4 makes a single phase measurement every four pulse repetitions, so this is reflected in Equation 2.27. This maximum phase rate is equivalent to about 2,000 $\frac{\mu\varepsilon}{s}$ for the pulse rate of 100 kHz. Though this seems high, it can be exceeded with high-amplitude shaking.

The experimental results indicate that this strain rate was exceeded at times throughout the measurements. Figure 3.15 shows an example that occurred 2 s into the off-end vertical vibroseis sweep at a location 75 m along the ϕ-OTDR arrays. The ϕ-OTDR data from both cables shows abrupt jumps, which may be the result of phase determination error (strain rates higher than the system's maximum). The geophone data on the other hand is smooth because it does not have this optical limitation.

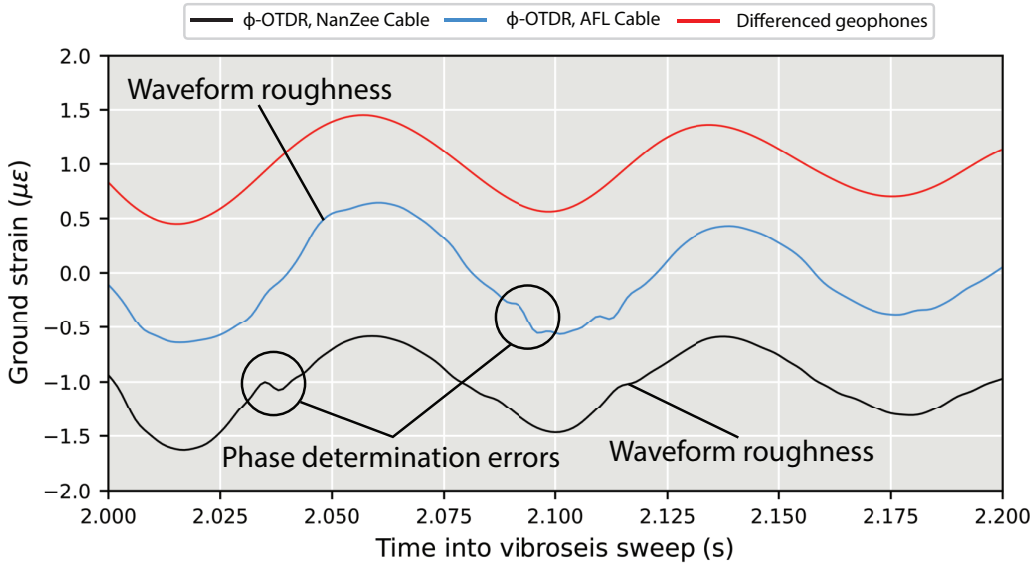

Figure 3.15: Close-up of the phase determination error problem that causes broadband noise in the ϕ-OTDR measurements at high strain-rates. The example shown is during vertical vibration when the vibroseis was located in the off-end source-receiver geometry 40m from the beginning of the arrays. The data shown in 75m along the arrays (115 m from the source). The time-series have been shifted for examination.

The abrupt jumps manifest as broadband noise in the ϕ-OTDR measurements only when vibration is happening. In addition to the abrupt jumps, there is general waveform roughness in the ϕ-OTDR data. This could be caused by uneven deformation of the soil surrounding the cables, the cables deviating from being perfect straight or instrument non-linearity. As mentioned previously, ϕ-OTDR systems behave linearly when the strain only occurs in be-

tween the pulse scattering locations. In the case of a 2.04 m gauge length, the scattering centers are very close together and non-linear behavior may occur. Therefore, the ϕ-OTDR signal power appears to be higher than the geophones at frequencies above about 45 Hz in Figure 3.14 when it is not actually the coherent signal that is higher power. It is possible to better localize the noise in time by examining spectrograms of the records. Figure 3.16 shows spectrograms for both ϕ-OTDR cables and the geophone pair at 75 m into the arrays (115 m from the source) during the vertical vibroseis sweep. The noise that extends to high frequencies is concentrated between 2-4 seconds into the vibroseis sweep which also corresponds to the time of maximum force output by the T-Rex shaker truck. The spectrogram from the geophone measurements does not show this noise source. The 75 m location selected for Figure 3.16 is representative of the entire array because this noise persisted at all offsets as indicated by the high frequency power previously shown in Figure 3.13, though the power of the phase determination error-induced noise diminished with the power of the signal (i.e., remaining relatively constant in SNR).

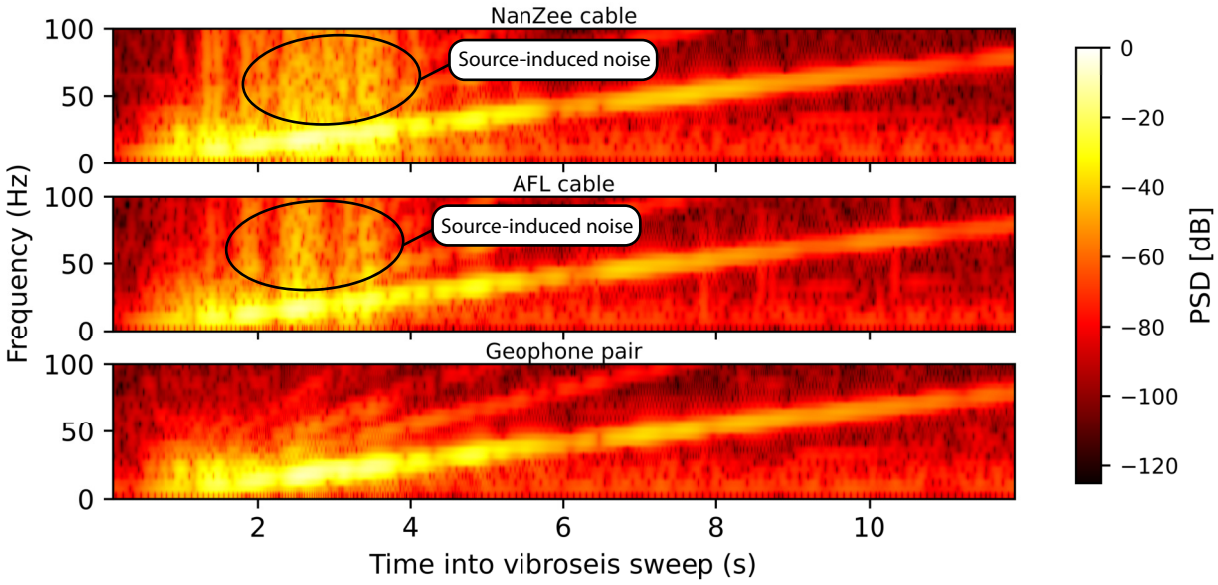

Figure 3.16: Spectrograms of ϕ-OTDR and spatially differenced geophone time-series 75m along the arrays (115 m from the source) during the vertical vibration. The spectrogram employs a 206-point FFT over a Hann window with a 205-point overlap between windows. All signals were processed at 1000 Hz sampling rate.

3.10 Discussion of Signal Amplitude

The signals measured with ϕ-OTDR have a statistically larger amplitude than the geophone measurements. Figure 3.17 shows the comparison of measurement amplitudes made during vibration by the T-Rex source 40 m from the array in the off-end orientation for both cables when the vibration was vertical and horizontal in-line. The vertical shaking resulted in ϕ-OTDR-measured strain values that average 8% higher than the geophone measurements. The horizontal in-line shaking resulted in ϕ-OTDR measurements that average 12% higher than the geophone measurements. The cable choice did not change the results of this amplitude analysis.

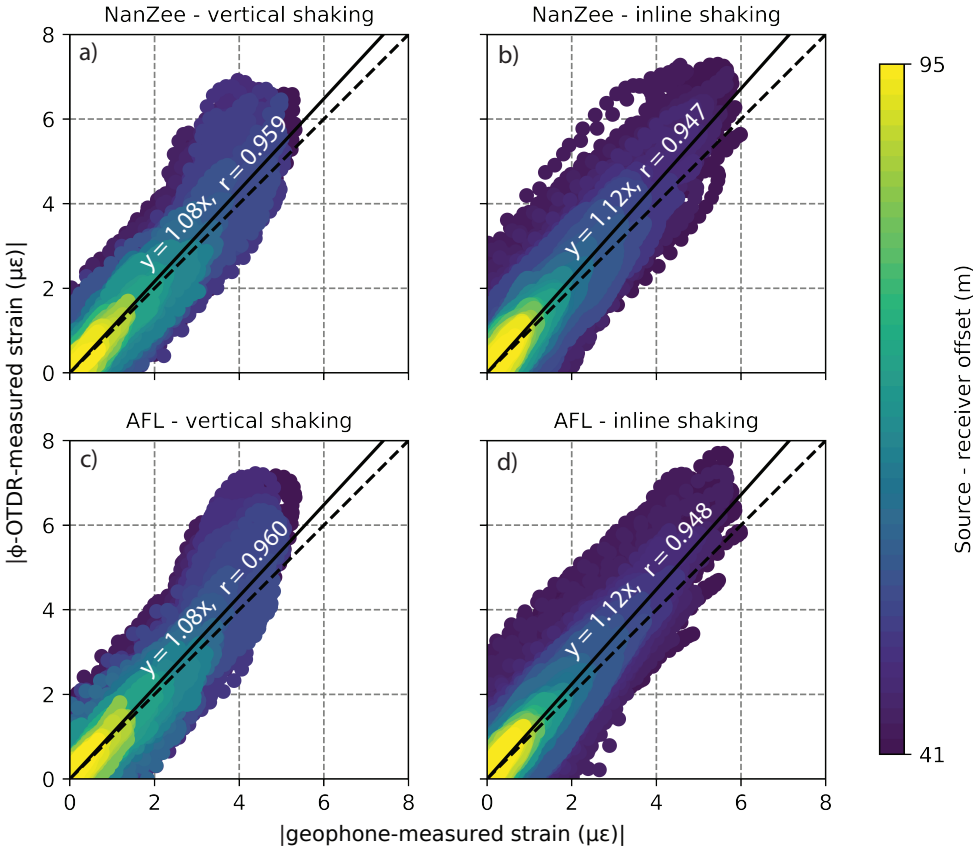

Figure 3.17: Comparison of strain measurement amplitudes made simultaneously with ϕ-OTDR and geophones over the length of the geophone array during T-Rex shaking in the off-end configuration 40 m from the array for: (a) the NanZee cable during vertical shaking, (b) the NanZee cable during in-line shaking, (c) the AFL cable during vertical shaking and (d) the AFL cable during in-line shaking. The dotted black lines have a slope of 1, and the solid lines are the linear best fit with their equations and r-values displayed.

Using the transfer functions for ϕ-OTDR introduced in Section 3.2, the response of the field acquisition to spatial waves is shown in Figure 3.18 as a combination of the gauge length, pulse shape and cable designs (see Equation 3.6). The transfer functions are shown in the wavenumber domain up to the spatial Nyquist frequency determined by the 1.02 m trace separation. The gauge length was 2.04 m, the pulse length h_p was 1.02 m (determined by a 10 ns pulse duration time using Equation 3.14) and the properties of the two cables are shown in Table 3.2. Using these properties the β values as determined by Equation 3.2.3 are 1.4 and 1.3 for the NanZee and AFL cables, respectively.

Table 3.2: Material characteristics of the cables deployed in the field

Cable name	Component	Material	Outer radius (mm)	Young's modulus (GPa)	Poisson's Ratio	shear modulus
NanZee NZS-DSS-C02*	optical fiber	fused silica	0.0625	72.4	0.17	31
	coating	acrylate	0.125	3.3	0.37	1.2
	buffer	hytrel	0.45	1.2	0.39	0.43
	reinforcement	steel	1.35	200	0.28	79.3
	outer jacket	polyethylene	2.5	1.0	0.50	0.33
AFL X3004955180H-RD†	optical fiber	fused silica	0.0625	72.4	0.17	31
	coating	acrylate	0.125	3.3	0.37	1.2
	buffer	-	0.45	1.2	0.39	0.43
	reinforcement	aramid yarn [146]	2.0	124	0.36	41
	outer jacket	polyurethane [147]	2.75	0.50	0.48	0.17

* Materials and geometry confirmed by cable manufacturer
† Geometry and material properties estimated, buffer material name unknown

As shown in Figure 3.18, the gauge length and pulse shape filters dominate the ϕ-OTDR transfer function. The geophone array transfer function for strain measurement is equivalent to the gauge length filter in Figure 3.18. This approach states that the geophone response should be higher across the entire frequency band than the ϕ-OTDR measurements, but this is not the case. The reason for this slight discrepancy is unknown, however it is likely from variability in the geophone temporal transfer function described in Equation 3.20. An advantage of ϕ-OTDR is that the temporal response is flat, requiring no correction. The geophones have a large uncertainty in their correction because it involves damping of a dynamic system D, and scaling factor S. The scaling factor changes with the electrical impedance of the geophones a seismograph. Another source of error in the horizontal geophone measurements is slight vertical coupling. The surface waves that are dominant in the measurements are elliptical in motion, so they have significant vertical energy. Slight orientation of the geophones off of vertical may cause some destructive interference, though this needs to be verified. Considering these sources of uncertainty in the geophone transfer function the data match is quite good. Figure 3.18 also shows that the cable impact on the ϕ-OTDR transfer functions were minimal, and both the AFL and NanZee cables provide adequate coupling for the spatial frequencies measured. This is confirmed by Figure 3.17 which shows no measured difference between the amplitudes measured with each cable.

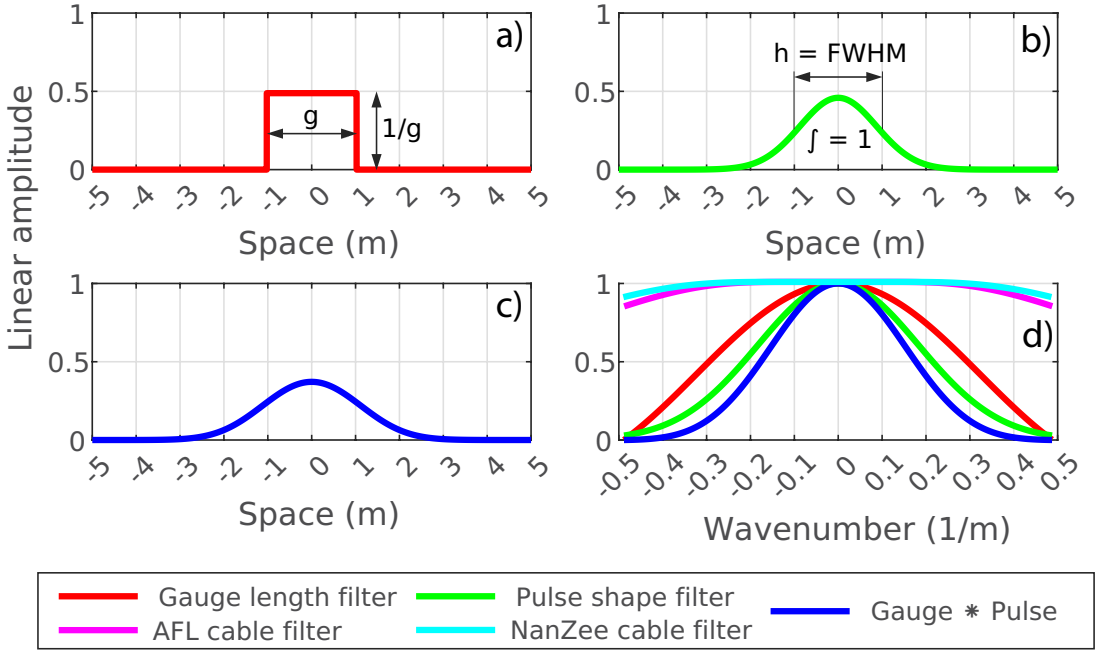

Figure 3.18: The space domain impulse responses of (a) the gauge length filter, (b) the pulse shape filter and (c) the combined gauge length $*$ pulse shape filters, and (d) the transfer functions caused by the gauge length filter, pulse shape filter combined gauge length $*$ pulse shape filters, and the filters for the separate cables.

3.11 Summary of Research Contributions

The potential for using ϕ-OTDR as an engineering tool for applications such as dynamic ground deformation measurement and soil-structure interaction studies, or FWI imaging relies on understanding both the amplitude and phase of the measurements. ϕ-OTDR deployment, quantification, channel positioning, and numerical simulation techniques in this chapter aim to demonstrate ϕ-OTDR as a viable sensing tool for these types of uses.

The transfer function for ϕ-OTDR was developed encompassing the gauge length, pulse shape and cable design assuming linear behavior between the fiber optic cable and the ground. A wavelength versus gauge length relationship was developed for assessing strain measurement made with ϕ-OTDR versus the pointwise strain field. This relationship was demonstrated through the transfer function, theoretical reception patterns and by using 3-D finite-difference simulations of wave propagation in an elastic solid. It was found that the wavelength versus gauge length relationship is critical for fully capturing pointwise strain waveforms, and this relationship must be understood for effective quantitative deployments

where pointwise strain is desired. However, it was demonstrated that strain measured with ϕ-OTDR is easily modeled as a difference of the displacement field over the system's gauge length, allowing for forward-modeled problems to solve for the ϕ-OTDR measurement directly. In the event that pointwise strain is desired, a method for assessing the wavelength-to-gauge length ratio for field data is demonstrated using a field acquisition and ϕ-OTDR measurements acquired with various gauge lengths.

Experimental comparison of measurements made by geophones and ϕ-OTDR using large vibroseis trucks and sledgehammer strikes was presented. It is shown that ϕ-OTDR measures ground deformation quantitatively with both amplitude and phase that agree with measurements made by geophones. The reception characteristics are consistent with the theory and simulation results including predictable zones of zero reception and changes in the sign (phase-flips) of the measured strain.

This chapter demonstrates that certain key steps need to be undertaken to ensure the quality of the ϕ-OTDR measurements and their comparison to geophones. Those key steps are: (1) aligning the ϕ-OTDR channels and geophones using a new method presented in this work, (2) selecting a ϕ-OTDR cable that provides deformation coupling to the internal optical fiber, (3) coupling the cable to the ground through direct burial and compaction, and (4) laser frequency drift mitigation through high pass filtering the ϕ-OTDR measurements. After these steps were taken, the ϕ-OTDR measurements and geophone measurements were shown to be very consistent with each other in both phase and amplitude. Two different suitable cables for direct buried ϕ-OTDR arrays are detailed including a proposed analysis of their transfer functions. A source of broadband noise, phase determination errors, is discussed for its impact on the signal spectra of ϕ-OTDR measurements, but is shown to have limited impacts on the waveform comparisons between ϕ-OTDR and geophones.

Chapter 4

Pavement Deformation Monitoring and Event Detection

This chapter is adapted from an article published in the journal *Structural Control and Health Monitoring* on August 3rd, 2022. The article is available at the following citation [148]:

Peter G. Hubbard et al. "Road Deformation Monitoring and Event Detection using Asphalt-embedded Distributed Acoustic Sensing (DAS)". In: *J Struct Control Health Monit.* e3067. (2022). DOI: 10.1002/stc.3067.

This chapter demonstrates that ϕ–OTDR can be used to monitor road pavements in a continuous fashion with a strain precision not previously possible. The chapter reviews the currently methods for pavement monitoring, and then presents a deployment of fiber optic cables used for ϕ–OTDR into a new pavement system at its time of construction. The strain measurements made by ϕ–OTDR are verified by pavement strain gauges and OFDR over a short length (due to OFDR's limitation). The sensitivity of the ϕ–OTDR installation is tested by measuring the strain induced by a large puckup truck, a cyclist, pedestrian and then a dog moving on the road surface. ϕ–OTDR presents the ability to sense events on the road surface due to mechanical deformation that is unprecedented.

4.1 Background

AC makes up 98% of the paved public road surfaces in the United States [149]. AC is created by mixing coarse and fine aggregates with bituminous binder. The mixture can then be laid and compacted in place to create a low-cost, rapidly constructed road surface that provides a comfortable and quiet ride for vehicles. To construct a road surface, AC is typically placed on top of a base layer of engineered material underlain by the compacted natural subgrade. There may also be a subbase layer added depending on the environment and design purpose

of the pavement system [150].

Pavement systems have been traditionally designed using empirical methods stemming from data measured at the AASHTO test road in late 1950's [151]. Recently, there has been a shift towards using a mechanistic-based method for pavement design. This method is known as mechanistic-empirical (ME) pavement design [152]. ME design is based on the desired performance of the road. Performance parameters include stresses, strains, and deflections that the road is expected to experience during its lifetime. Roadway performance evaluation is an important part of ME pavement design. Instruments like the falling weight deflectometer (FWD) are used to measure the actual behavior of pavements to assess if they need to be remediated or replaced. This performance-based design approach has opened the door for structural health monitoring (SHM) of pavements. SHM in combination with ME design methodologies can be used to validate design parameters and monitor pavement performance over time.

SHM of pavements has been researched extensively over the last three decades. Techniques include visual examination for surface manifestation of damage and mechanical behavior measurement using in-situ sensors. Surface monitoring technologies naturally evolved from the process of visual inspection of pavements to identify types of damage including cracking, rutting and permanent deflections [153]. These technologies include computer vision techniques to examine images and classify damage [154]. On the other hand, in-situ sensors have been tested to measure pressure, strain, temperature, density and moisture inside pavement systems [155].

Of particular interest to this study is previous research on monitoring in-situ mechanical behavior of pavements in the longitudinal road direction under dynamic loading. Since the longitudinal strain at the bottom of the AC layer has been used historically to evaluate pavement design [156], the typical embedment position of sensors is at this level. For example, in Zafir et al. (1994), strain gauges were installed at the bottom of an asphalt layer (depth of 150 mm) to measure strain under the moving load from a semi-tractor-trailer truck [157]. Bayat et al. (2012) also embedded strain gauges at the bottom of an asphalt layer (depth of 185 mm) [158]. Both test results showed that the pavement experienced a compression-tension-compression spatial strain variation in the longitudinal direction under an axle load.

More recent work shows pavement strain data at shallower levels. Gokhale et al. (2009) measured vehicle induced strain at different levels of a pavement system [159]. It was shown that the pavement experienced longitudinal compression close to the surface (at a depth of 127 mm), whereas the strains at a deeper level (for example, 381 mm) were in tension. Kara De Maeijer et al. (2018) measured the strain response of pavement at 30-, 70-, and 120-mm depths under loading from a paving machine [160]. The test results showed that the pavement exhibited a tension-compression-tension strain variation in the longitudinal direction at the 30- and 70-mm depths, whereas a compression-tension-compression signature was seen at the 120-mm depth. The magnitude of compression observed at the 70-mm depth was smaller than that at the 30-mm depth, indicating that the pavement system is expected to exhibit a maximum longitudinal compressive strain toward the top surface right under the applied

load.

Mustafa et al. (2021) was the first to demonstrate the feasibility of a distributed fiber optic sensing technology called optical frequency-domain reflectometry (OFDR) to measure longitudinal strains when embedded within pavements [161]. Fiber optic sensing cables were installed at 10-, 20- and 40-mm depths within AC. Results showed that the 10-mm embedment depth was preferred for maximum sensitivity to a tension-compression-tension spatial strain variation under localized surface loading. Although OFDR can measure strain at high spatial resolution, the coverage length is less than 50 m. Therefore, at present, OFDR technology is not suitable for practical road application. In this study, however, a short-range ODFR data set was used as a verification tool for the longer range, and more sensitive ϕ–OTDR measurements.

4.2 Experimental Configuration

The NZS-DSS-C02 fiber optic strain sensing cable that was first introduced in Chapter 3 (see Figure 3.6(d)) was installed in a roadway at UC Berkeley's Richmond field station. Embedding fiber optic sensing cables into Portland cement concrete (PCC) has been demonstrated successfully for monitoring several different types of structures [162, 163]. AC is a composite material that is made from aggregates and binder, similarly to PCC. In the case of PCC, the binder is Portland cement, while in AC the binder is bitumen. AC is usually manufactured using the hot-mix technique where the binder is heated to a high temperature before mixing in the aggregates. This is referred to as hot-mix-asphalt (HMA). HMA is mixed at a temperatures above 120°C and placed shortly after manufacturing. The low-density polyethylene used to make the NZS-DSS-C02 cable's sheath melts at approximately 110°C. This is expected to increase coupling with the cable and AC by allowing the cable to be melted in place. The largest construction concern for embedding sensing cables into the road is that AC is constructed in thin layers that are compacted significantly with industrial equipment. The compaction process poses the largest risk to the cables, so in this study a method of protecting the cables for paving was important. In addition to the fiber optic cables, Wheatstone bridge resistance strain gauges (PMFLS-60-50-10LTSC) manufactured by Tokyo Measuring Instruments Lab Co. were installed to verify the fiber optic measurements. The strain gauges were designed specifically for embedment into pavement.

The installation site was an existing road originally paved in 2004 and resurfaced in 2007. Figure 4.1 (top) shows aerial photographs of the road site after the fiber optic cables and pavement strain gauges were installed on the existing surface and the road after paving, whereas Figure 4.1 (bottom) shows two schematic drawings showing the horizontal and vertical locations of the fiber optic cables and typical strain gauges within the completed pavement. The road was moderately degraded at the beginning of the study, with longitudinal fatigue cracking having occurred over the length. The cracking was caused by AC fatigue of the existing overlay. The road was constructed of 200 mm of fine-grained subgrade, 395 mm of aggregate base (AB) class II, and 51 mm of AC, as shown in Figure 4.1 (bottom).

A new overlay was to be placed over top of the existing road surface, and an installation of fiber optic cables below the new overlay was designed. The new overlay was 31.75 mm of AC placed directly on top of the existing 51 mm thick AC.

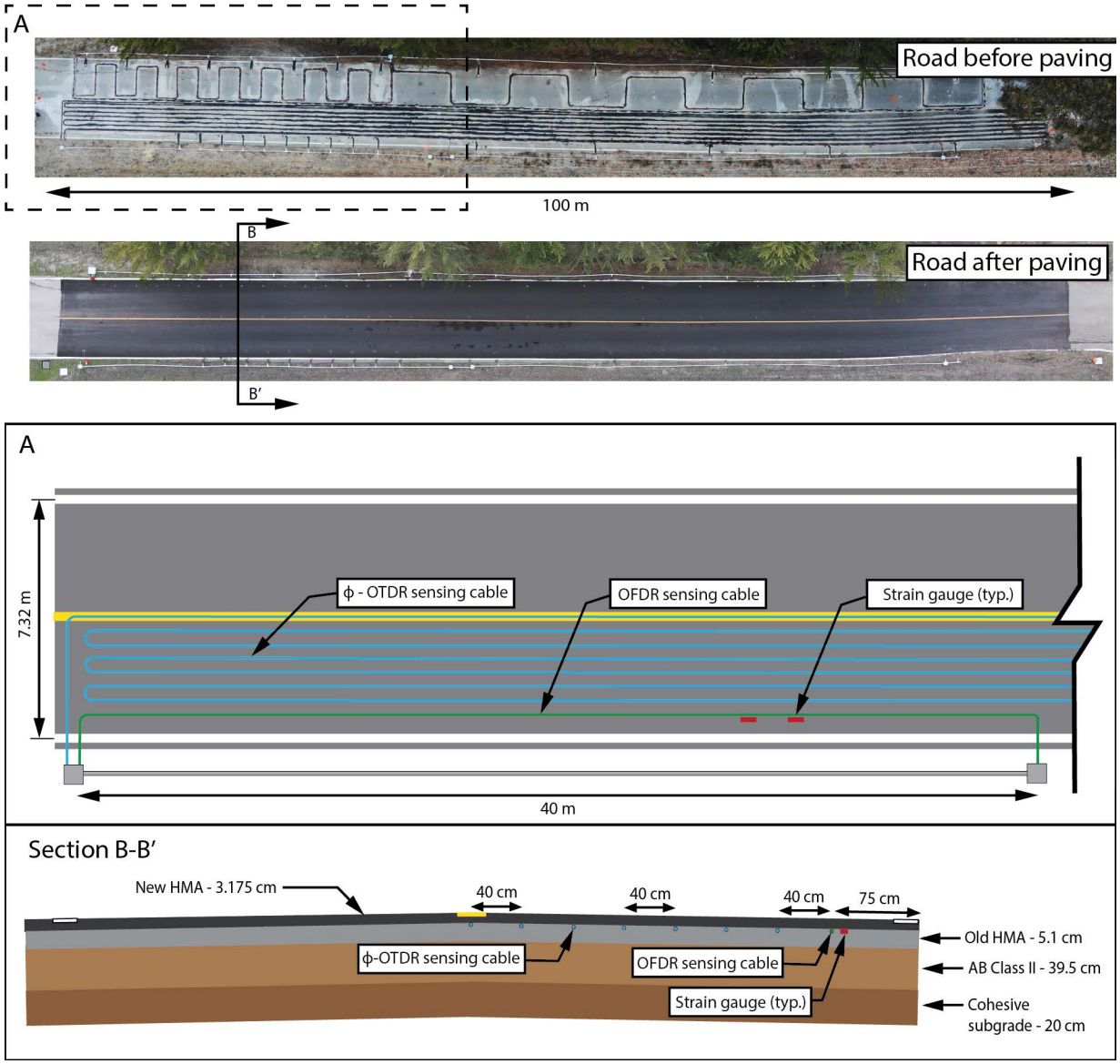

Figure 4.1: Aerial photographs of the road before and after paving with schematic diagrams of the fiber optic cable locations. Two lengths of NZS-DSS-C02 cable were installed into the pavement for this study. 40 m of cable was used for OFDR, while approximately 700 m was used for ϕ–OTDR due the difference in sensing range between the technologies. The ϕ–OTDR cable snaked back and forth along the length of the test road with each longitudinal line being 40 cm apart. Resistance strain gauges (PMFLS-60-50-10LTSC) were installed approximately 5 cm from the OFDR cable. After the cables were attached to the road surface the road was paved over to fully encase the cables and strain gauges into the road.

Figure 4.2(a-f) shows the multi-step process of how the fiber optic strain sensing cables were installed into the roadway. First (Figure 4.2(a)) the location of where the cables would go was marked on the road using marking paint. Next (Figure 4.2(b)), 5 mm deep grooves were cut into the surface using a pavement saw. The fiber optic sensing cables were laid into the grooves and secured using tape (Figure 4.2(c)). Using a mixture of asphalt emulsion and sand, the groves containing the cables were covered for protection during paving (Figure 4.2(d)). A tack-coat was applied to the surface (Figure 4.2(e)), and the road was paved using standard procedures which included placement of asphalt and vibro-compaction of the new surface (Figure 4.2(f)). The strain gauges were installed by placing them within a rectangular cutout of the existing road surface and surrounding them with a mixture of asphalt emulsion and sand to make them lay flat on the road and protect them during paving. The strain gauges had a larger amount of the asphalt emulsion and sand both underneath and on top of them than the fiber optic cables due to their size and shape. This produced a slightly different coupling which will be discussed later. They can be seen to the left of the fiber optic cables in Figure 4.2(d).

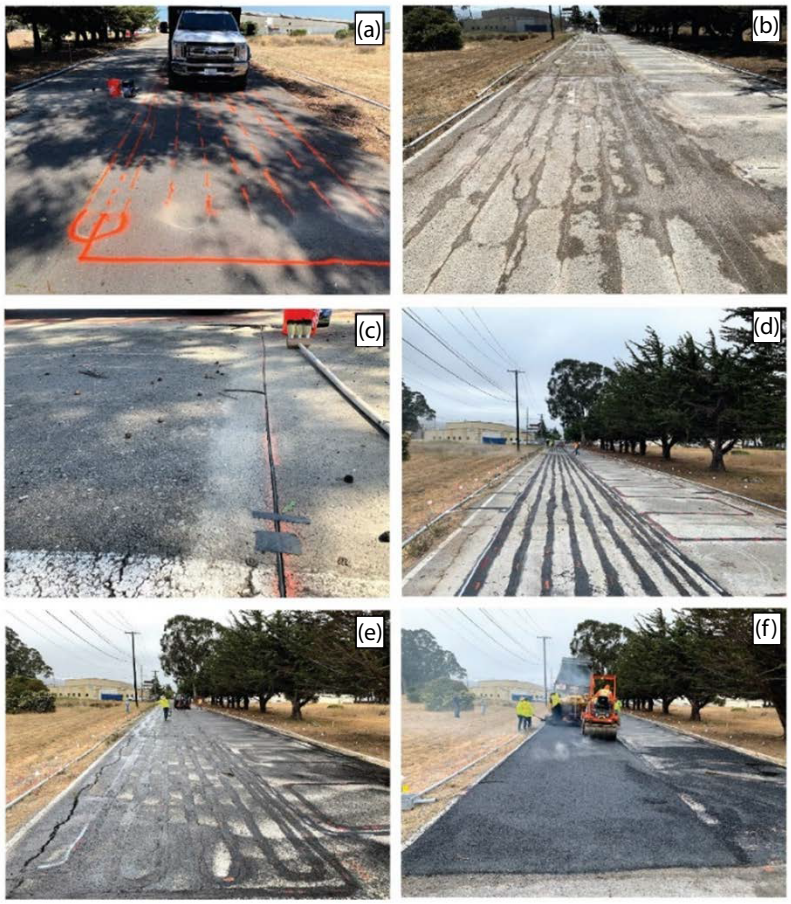

Figure 4.2: The fiber optic sensing cable installation procedure consisted of (a) marking the locations of the cables on the existing road surface with marking paint, (b) cutting grooves into the pavement surface 5 mm deep with a pavement saw, (c) laying the NZS-DSS-C02 strain sensing cable into the grooves and securing temporarily with tape, (d) applying a mixture of asphalt emulsion and sand to the top of the grooves to protect the cables, (e) applying a tack coat to the entire road surface and (f) paving the surface using the standard procedure including placing the HMA with a paving machine and vibro-compacting it.

In this study, two dynamic, distributed fiber optic strain measurement systems (OFDR and ϕ–OTDR) were used. For the OFDR, a Luna Innovations ODiSI 6000 with a spatial resolution of 2.6 mm, an acquisition rate of 10 Hz and a sensing distance of 40 m was used. This OFDR system's maximum sensing length is 50 m. The ϕ–OTDR system was an Optasense ODH-4 with a gauge length of 2.04 m, an acquisition rate of 32 kHz and a sensing distance of 700 m.

Although the same fiber optic cable can be used interchangeably with different DDFOS technologies, separate cables were installed so that simultaneous readings made by different

technologies could be compared. As previously mentioned, OFDR can only operate over a limited length. A 40 m cable was installed specifically for this purpose and is shown in green in Figure 4.1. ϕ–OTDR can operate over a much longer distance, so it used a cable that is continuous over 700 m snaking back and forth in one lane. The specifics of the box-shaped installations in the right lane of Figure 4.2(d) are not discussed in this work.

The paving process was observed in real-time using the ϕ–OTDR system. The data presented in Figure 4.3 is the frequency band extracted (FBE) power in the 17-100 Hz range during the paving process. This type of FBE data display is common for DAS and referred to as a waterfall diagram. It is generated by taking the short-time Fourier transform of each readout channel and plotting the power in a specific frequency range as a pixel color. Figure 4.3 shows a mirrored repetition of similar data 7 times. Each repetition corresponds to a length of fiber optic cable stretching the length of the road as shown in Figures 4.1 and 4.2(d). Two distinct construction phases are shown at the top of Figure 4.3. In the first phase, the paving machine just completed paving the very beginning of the road, while an asphalt truck is backing down the road to refill the paving machine. The second phase is the paving machine and asphalt truck moving together as the paving progresses while a vibratory compactor moves forward and backwards compacting the asphalt. The events can clearly be observed by examining the waterfall plots generated from the ϕ–OTDR data. In addition to the movement and location of the construction vehicles on the surface, the activities of the vibratory compactor can be seen in detail. Large power is exhibited in the FBE data when the vibration is on. Visualizing data in both space and time is important for the later parts of this work and this data is displayed as an introduction. Figure 4.3 shows data in terms of frequency band power, but the pixels can be other information such as strain, which is explored in the next sections.

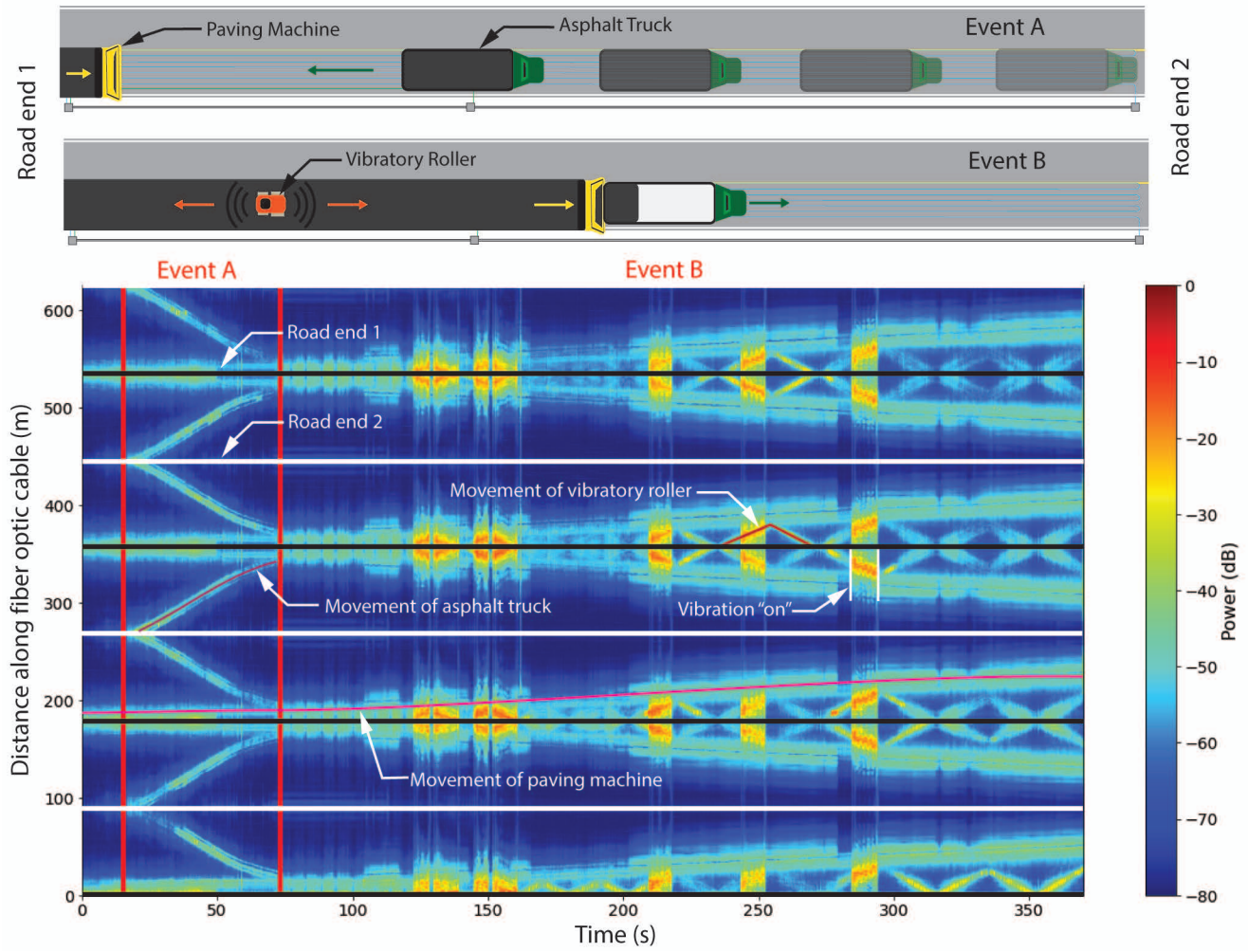

Figure 4.3: Schematic diagrams of the paving phases and corresponding ϕ–OTDR 17-100 Hz frequency band extracted data. The different events that occurred on the road are labeled on the FBE plot including movement of the vibratory roller, movement of the asphalt truck and movement of the paving machine.

4.3 Precision Error Evaluation of OFDR and ϕ-OTDR

OFDR Instrumentation

A typical time-series and power spectral density (PSD) of the OFDR data produced by the road instrumentation when no objects are on the road surface is shown in Figure 4.4. The data exhibits a statistical repeatability, as quantified by the standard deviation of 30 s of

time measurements acquired at 10 Hz of ± 2 $\mu\varepsilon$. The average noise floor shown in the PSD plot is 0.3 $\frac{\mu\varepsilon}{\sqrt{\text{Hz}}}$. A time series of the sort shown in Figure 4.4 is generated every 2.6 mm along the sensing cable within the road. This creates a matrix of data where one dimension is indexed by the time interval of 0.1 s, and the other dimension is indexed by the physical spacing. Although OFDR has a relatively high noise floor as compared to ϕ–OTDR (see the next section), its naturally flat frequency response (requiring no post-processing) and high spatial resolution make it a useful technology for verifying measurements made with ϕ–OTDR.

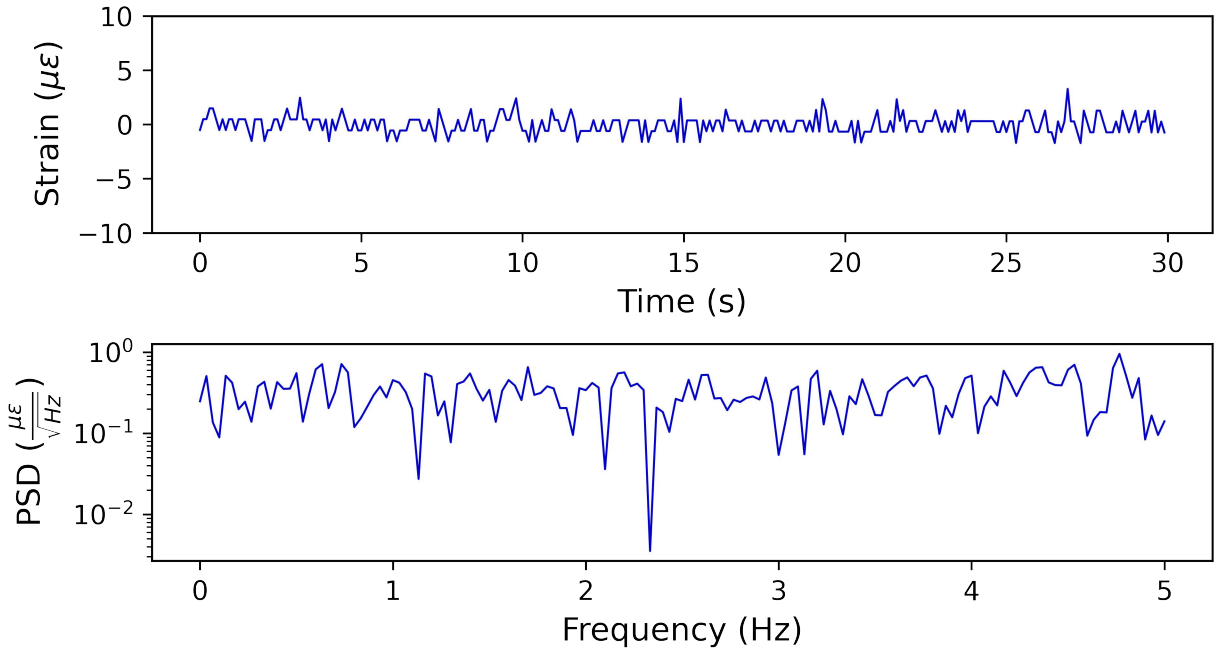

Figure 4.4: Time-series and power spectral density plots of 30 seconds of OFDR data acquired from within the pavement at the sampling rate of 10 Hz when nothing is happening on the road surface.

ϕ-OTDR Instrumentation

As discussed previously, a large challenge of making quantitative strain measurements with ϕ–OTDR is its inherent drift at low frequencies caused by laser phase drift and temperature-induced strain of the sensing fiber. For roadway monitoring, vehicles move, and events happen dynamically, allowing for the low-frequency noise to be effectively filtered out without damaging the measurements of interest.

Figure 4.5 shows strain measurements and the associated PSD made by ϕ–OTDR when no objects are on the road surface. This can be considered a measure of the environmental

and systemic noise characteristics of the configuration. The low frequency noise manifests as a drifting of the strain measurements. In this case, the measured strain drifts by 0.08 $\mu\varepsilon$ (80 nε) over 30 s.

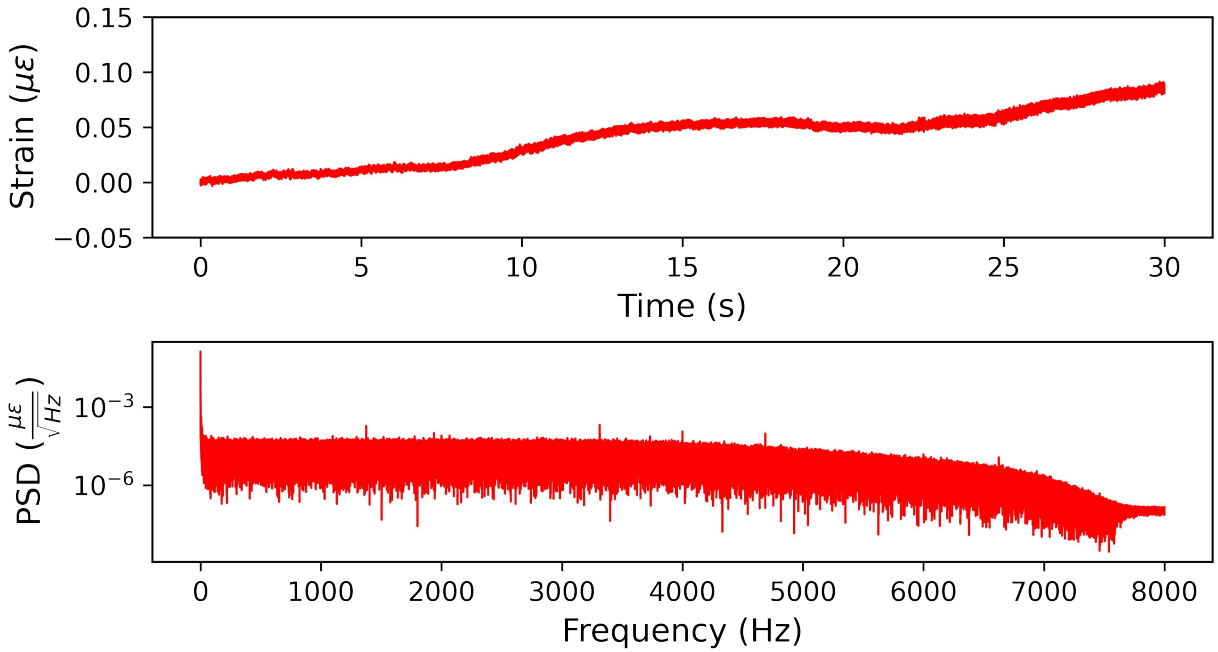

Figure 4.5: Unprocessed time-series and power spectral density plots of 30 s of ϕ–OTDR data acquired from within the pavement at the sampling rate of 32 kHz when no object is on the road surface.

The ϕ–OTDR data are post-processed using two steps. First, they are decimated. This process includes the application of an antialiasing filter and then down sampling to a rate of 40 Hz. A Butterworth digital high-pass filter is applied in post-processing to the measurements with a -3 dB point of 0.08 Hz. The Butterworth filter was chosen because of its minimal ripple characteristic in the passband. The strain measurements made are therefore minimally affected by the application of this filter if their frequency components are within the passband of the filter. Figure 4.6 shows the data after the decimation and filtering process. The strain scale for the time-series plot is ± 0.05 $\mu\varepsilon$ (50 nε). The associated standard deviation of this data and statistical repeatability of the strain measurements is ± 0.002 $\mu\varepsilon$ (2 nε). This is three orders of magnitude less than the reported value for the commercial OFDR system, as described in the previous section. The dynamic noise floor is shown as 10^{-3} $\frac{\mu\varepsilon}{\sqrt{\text{Hz}}}$ for signals near DC, and 10^{-4} $\frac{\mu\varepsilon}{\sqrt{\text{Hz}}}$ for signals at 10 Hz.

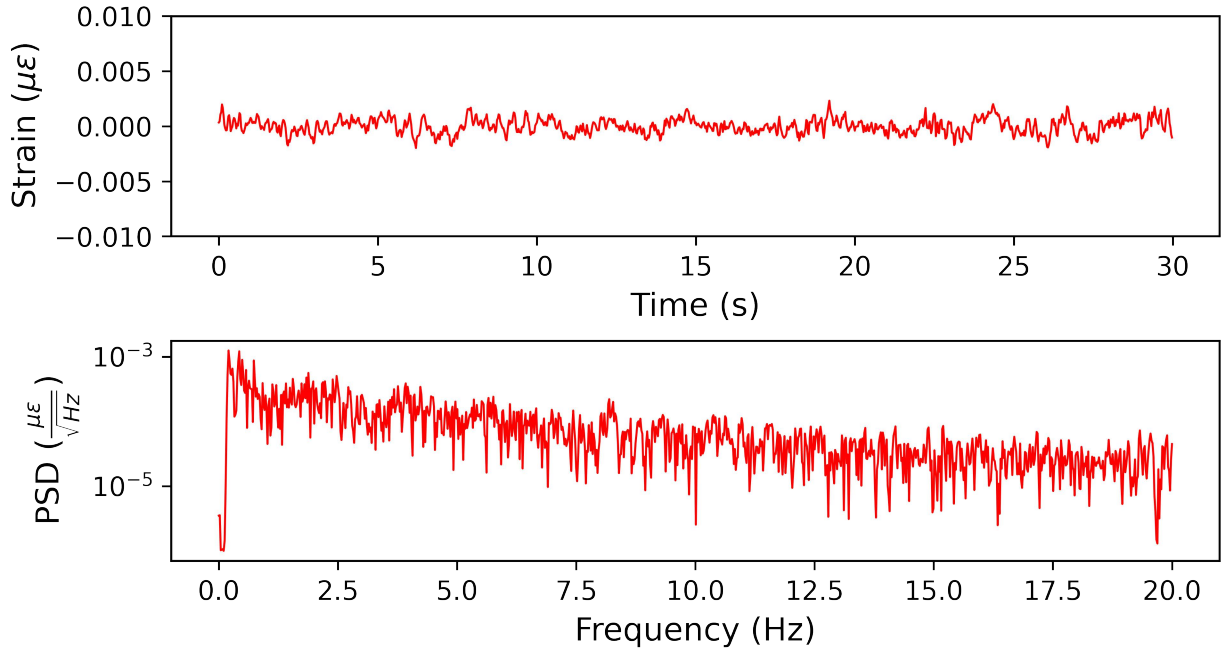

Figure 4.6: Time-series and power spectral density plots of 30 seconds of ϕ–OTDR data acquired from within the pavement that has been post-processed by decimating the data to a new sampling rate of 80 Hz and high-pass filtering the data using a digital Butterworth filter with a -3 dB point of 0.08 Hz.

4.4 Validation of OFDR Measurements using Strain Gauges

Since OFDR measures strain over a very short distance (2.6 mm in this study), it can be compared with traditional strain gauges. The strain gauges that were installed into the pavement were oriented in the same direction as the fiber optic cable. Figure 4.7 shows an example of the measurement consistency between strain gauges and OFDR. In this case, a sedan with a mass of 1,252 kg was parked with its front wheel over the location of a strain gauge and OFDR channel in the test road. After being parked for 250 s, the sedan moved its wheel 1 m away from the strain gauge for 150 s, before returning to its initial position. The OFDR measurements match well with the strain gauge measurements for both the loaded and unloaded condition, as well as the rebound between phases. The strain gauge data exhibits more hysteresis than the OFDR data evidenced by its time-lag to return to zero strain after the wheel is removed. This may be due to the difference in installation between the strain gauge and the fiber optic cable. As previously discussed, the strain gauge was placed in a rectangular cut-out of the previous road surface and surrounded with a mixture

of asphalt emulsion and sand before the new pavement was overlain on top of it. This may have contributed to the strain gauge exhibiting a more viscous response than the fiber optic cable which was directly in contact with the lower layer of AC and then melted in place during paving.

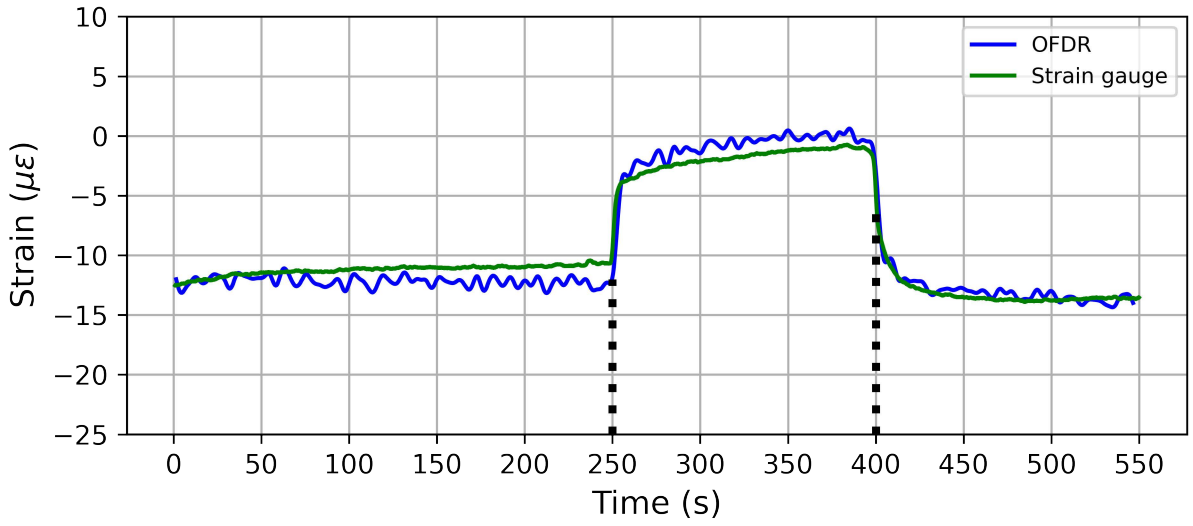

Figure 4.7: Comparison of Wheatstone bridge strain gauge measurements with OFDR measurements while a sedan's front wheel was parked on top of the collocated strain gauge and OFDR channel, removed for 150 s and then replaced. The black dotted lines indicate the time period where the wheel was removed from the strain gauge and OFDR channel position.

Since strain gauges are discrete measurements points, they are not effective for comparison with a spatial measurement technology like ϕ–OTDR. Since ϕ–OTDR measures average strain over 2.04 m, other mechanisms such as transitions from compression to tension away from wheels influence the measurements. For this reason, strain gauges were used to validate OFDR, and in turn OFDR was used to compare with ϕ–OTDR in the next section.

4.5 ϕ-OTDR Measurement Validation during Truck Loading using Finite Element Analysis and Comparison to OFDR

One length of ϕ–OTDR cable is used in the following sections. It is the length located 400 mm from the OFDR cable as indicated in Figure 4.8. To verify the ϕ–OTDR measurements, comparisons with OFDR measurements were conducted for the case when a Ford F-350

pickup truck with a mass of 2,830 kgs moved on the road surface. The first test was the truck performing a repeated stop-and-go every 2 m along the road. The second test was the truck moving at approximately 0.5 m/s. The truck's front, road shoulder-side wheel was centered at approximately 750 mm from the edge of the road, which is the OFDR sensing cable location. The longitudinal location of the truck and its axles during the stop-and-go test, as well as the lateral spacing during both tests are shown in Figure 4.8.

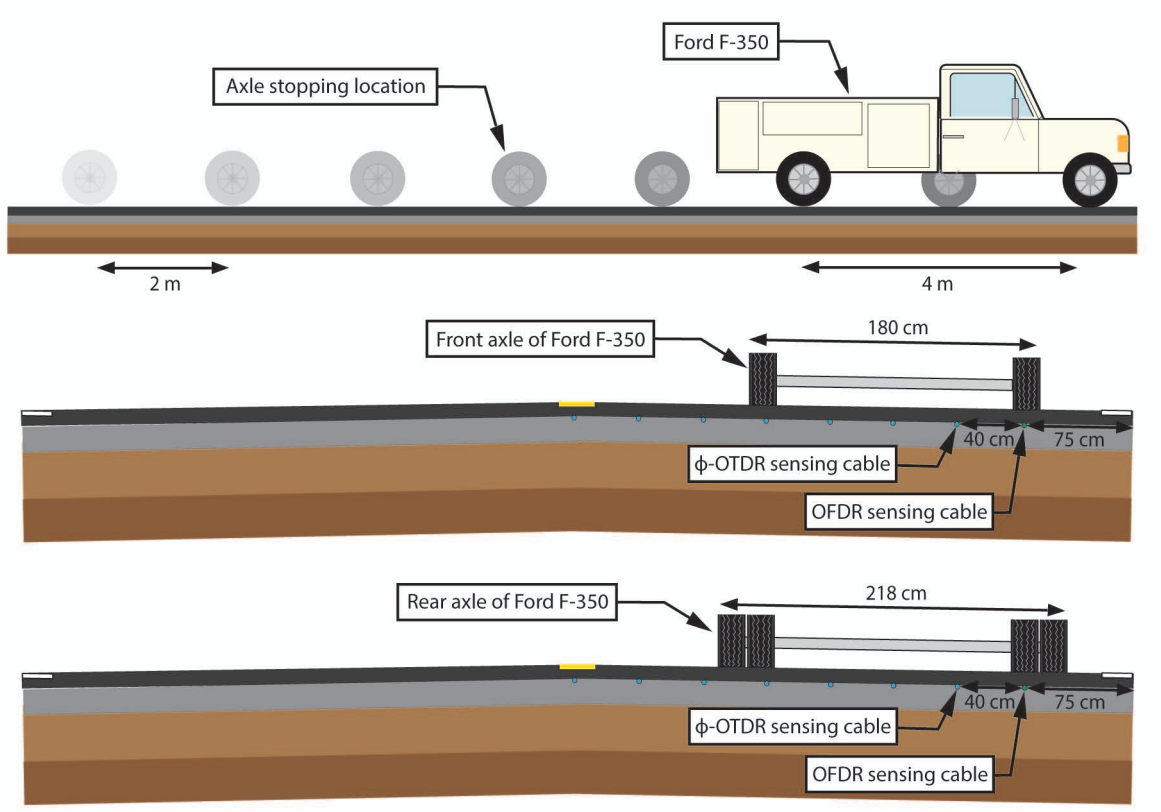

Figure 4.8: The location of the Ford F-350 pickup truck's axles on the test road relative to the sensing cable locations within the pavement. During the stop-and-go test, the truck was advanced down the road 2 m at a time and then stopped for 10 s. The OFDR cable was located 75 cm from the road shoulder while the ϕ–OTDR cable was located 115 cm from the shoulder. The F-350 had a dual rear axle, so the configuration is shown for both axles.

The truck was advanced down the road 2 m at a time, sitting for 10 s at each location. This allowed for the ϕ–OTDR data to be processed using the decimation and high pass filtering explained previously because the strain is dynamic, albeit at very low frequency. The measured strain values ($\varepsilon = \frac{\Delta L}{L}$) vary with the gauge length (L) of the two systems. In the case of the OFDR system, L is 2.6 mm, while for ϕ–OTDR it is 2.04 m. Therefore,

measurements are expected to be much lower for the ϕ–OTDR system when subject to the same deformation.

As shown in Figure 4.8, the location of the cable for ϕ–OTDR measurement was different from that for OFDR measurement. To make a meaningful comparison, the pseudo static ϕ–OTDR and OFDR measurements were compared with 3-D finite element (FE) modeling results when the F-350 pickup truck stopped along the road. The loading case was modeled using Abaqus finite element software. The roadway and underlying soils were modeled as 3-D stress elements of type C3-D8RH; an 8-node linear brick with hybrid formulation, constant pressure, reduced integration, and hourglass control. Figure 4.9(a) shows the plan view of the top surface of the FE model indicating the locations of the ϕ–OTDR and OFDR cables relative to the truck wheel positions. The wheel positions are indicated by contours of longitudinal strain in the road under the truck's static load. Figure 4.9(b) shows an isometric view of the full 3-D FE model. The model was a cuboid 40 m long, 7.32 m wide and 15.68 m deep with six layers. The modeled layers consisted of the four layers as shown in Figure 4.1 (Section B-B') and an additional two layers of clay. The pavement's material properties were determined through consultation with a designing pavement engineer. The material properties and geometry of the saturated clay layers were determined from geotechnical exploration near the test site. The fully saturated clay was modeled in an undrained, constant volume condition (i.e., total stress analysis) because the testing was done relatively fast with negligible excess pore pressure dissipation. The model's material parameters are shown in Table 4.1. Loading from the truck was applied on the model statically using four area loads: 0.0625 m^2 for each front wheel and 0.1225 m^2 for each double back wheel. Each wheel location was loaded with 6.33 kN. The mesh of the model was refined at the simulated truck locations to capture the localized deformation. The total number of elements was 917,280.

Material	Tickness (m)	Young's Modulus (MPa)	Poisson's Ratio
New HMA	0.03175	4500	0.33
Old HMA	0.051	4700	0.33
AB Class 2	0.395	550	0.35
Cohesive Subgrade	0.2	95	0.35
Clay-1	4.32	200	0.499
Clay-2	10.68	250	0.499

Table 4.1: Material properties used for the elastic finite element analysis of the roadway

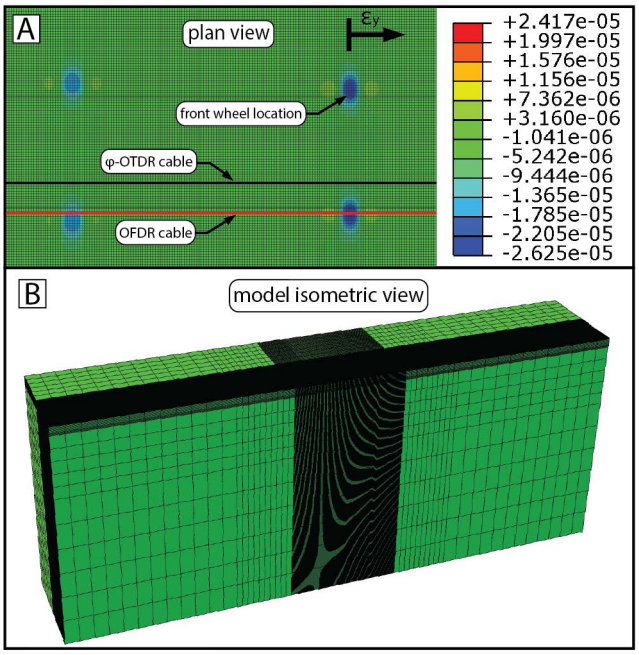

Figure 4.9: (a) Plan view of the 3-D Abaqus FE model with contours of longitudinal strain in the road. The model was made of 917,280 C3D8RH stress elements and refined below the location statically loaded by the truck's weight. The ϕ–OTDR cable was 40 cm towards the center of the road relative to the OFDR cable, which was centered under the front wheel of the truck. (b) Isometric view of the 40 m x 7.32 m x 15.68 m cuboid FE model.

The FE derived results are shown in Figure 4.10 compared with actual measurements from the first stop-and-go test. Since the FE mesh was coarser than the 2.6 mm length over which OFDR measurements were taken, the OFDR measurements and nodal strains are compared directly in Figure 4.10(top). Due to the high spatial readout of OFDR, the OFDR data appears as solid lines. There are compressive strains underneath each axle which transition to tensile strains on either side of the axles in both measured and simulated data. The spatial distribution of compressive strain is wider in the actual measured case using OFDR than in the simulation. This could be an effect of the steel-reinforced cable distributing strain along itself over a longer length than experienced by the pavement without the cables. The ϕ–OTDR measurements were compared by performing moving average of the calculated FE strain over the 2.04 m gauge length, as shown in Fig 11(bottom). The ϕ–OTDR data has a spatial readout of every 1.02 m, so it appears as discrete points. The ϕ–OTDR measurements and spatially averaged FE strain calculations match well.

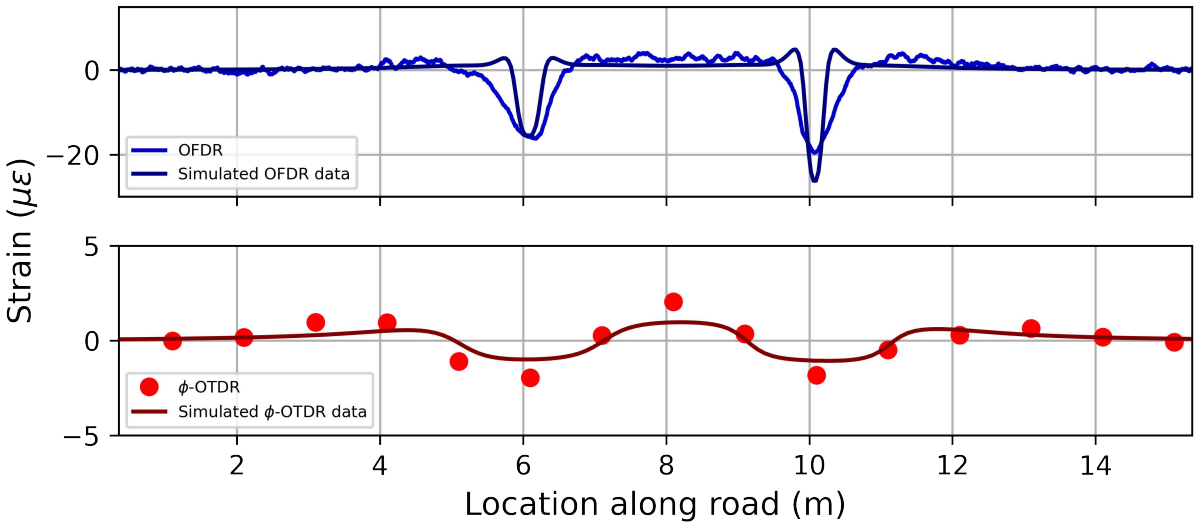

Figure 4.10: Results from the pseudo static verification test where the F-350 truck was stopped on the road for 10 s. Strain was measured using both OFDR and ϕ–OTDR and compared with the 3-D elastic FE analysis for the same cable locations. The ϕ–OTDR gauge length is simulated by averaging the FE analysis strain over 2.04 m.

Although the cable locations are different, the OFDR and ϕ–OTDR measurements can be compared more directly by spatially averaging the OFDR measurements over the longer gauge length of 2.04 m such that:

$$\varepsilon_{\phi-OTDR}(x) \cong \frac{1}{m+1} \sum_{n=-m/2}^{m/2} \varepsilon_{OFDR}(x + nL_{OFDR}) \tag{4.1}$$

where $\varepsilon_{\phi-\mathrm{OTDR}}$ is the strain measured with ϕ–OTDR, ε_{OFDR} is the strain measured with OFDR, m+1 is the number of OFDR measurements within one ϕ–OTDR measurement, and L_{OFDR} is the length over which one OFDR measurement is made. This is a centered spatial moving average of the OFDR data at the gauge length of the ϕ–OTDR system. This relationship is shown in Figure 4.11 for the case of the truck driving at 0.5 m/s down the road. A discrete moment in time is shown when the truck's axles are at approximately 6- and 10 m along the road.

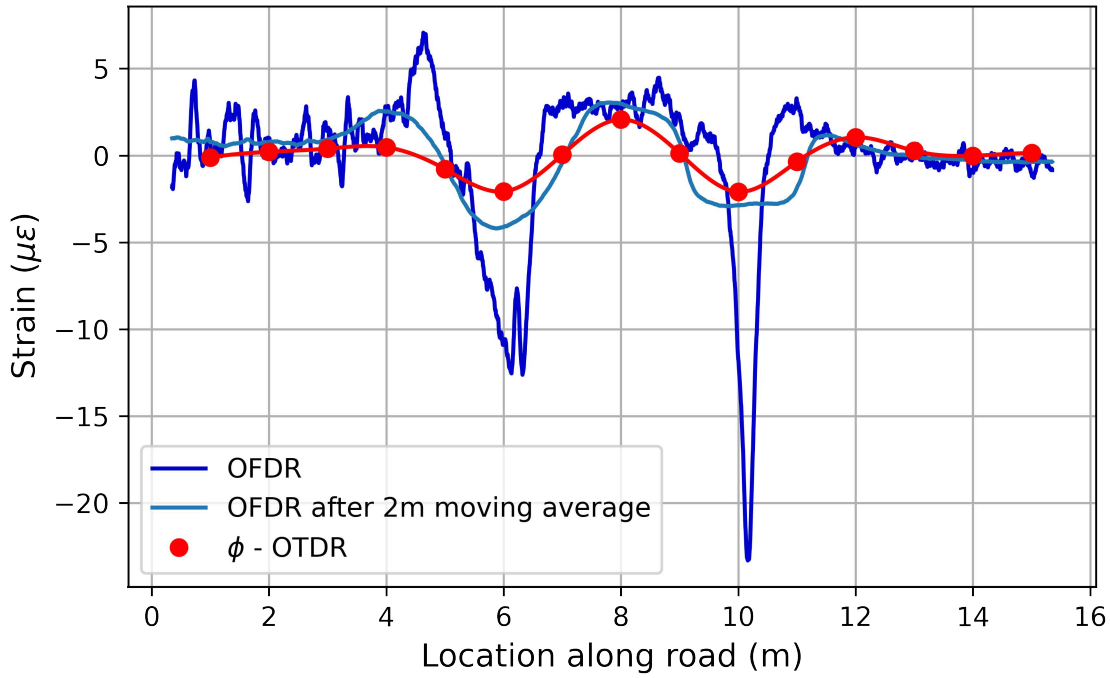

Figure 4.11: Results from the verification test where the F-350 truck was advanced down the road at 0.5 m/s. Strain was measured using both OFDR and ϕ–OTDR and the OFDR measurements were converted to equivalent ϕ–OTDR measurements using Eq 2. The cables were not at exactly the same location in the pavement (see Fig. 8), which is what the slight magnitude difference is attributed to.

The comparisons within Figure 4.12 also show that the value of the strain measurements made by OFDR are in good agreement with the ϕ–OTDR measurements. Once again, the magnitude of strain measured by OFDR is slightly higher due to its positioning directly under the wheel. The maximum compressive strain locations indicate the location of the axles. The value of this strain is typically 2.0 $\mu\varepsilon$ for ϕ–OTDR and 3.5 $\mu\varepsilon$ for OFDR. The regions of tensile strain in front of the truck, behind the truck and between the axles can be observed in both datasets. The resolution of the image created from the ϕ–OTDR data is less in the vertical direction because the spatial sampling of this data is one measurement every 1.02 m. For this small-scale example the spatial sampling appears very coarse in comparison to the OFDR image, however this sampling in space proves effective for localizing the strain from the truck axles.

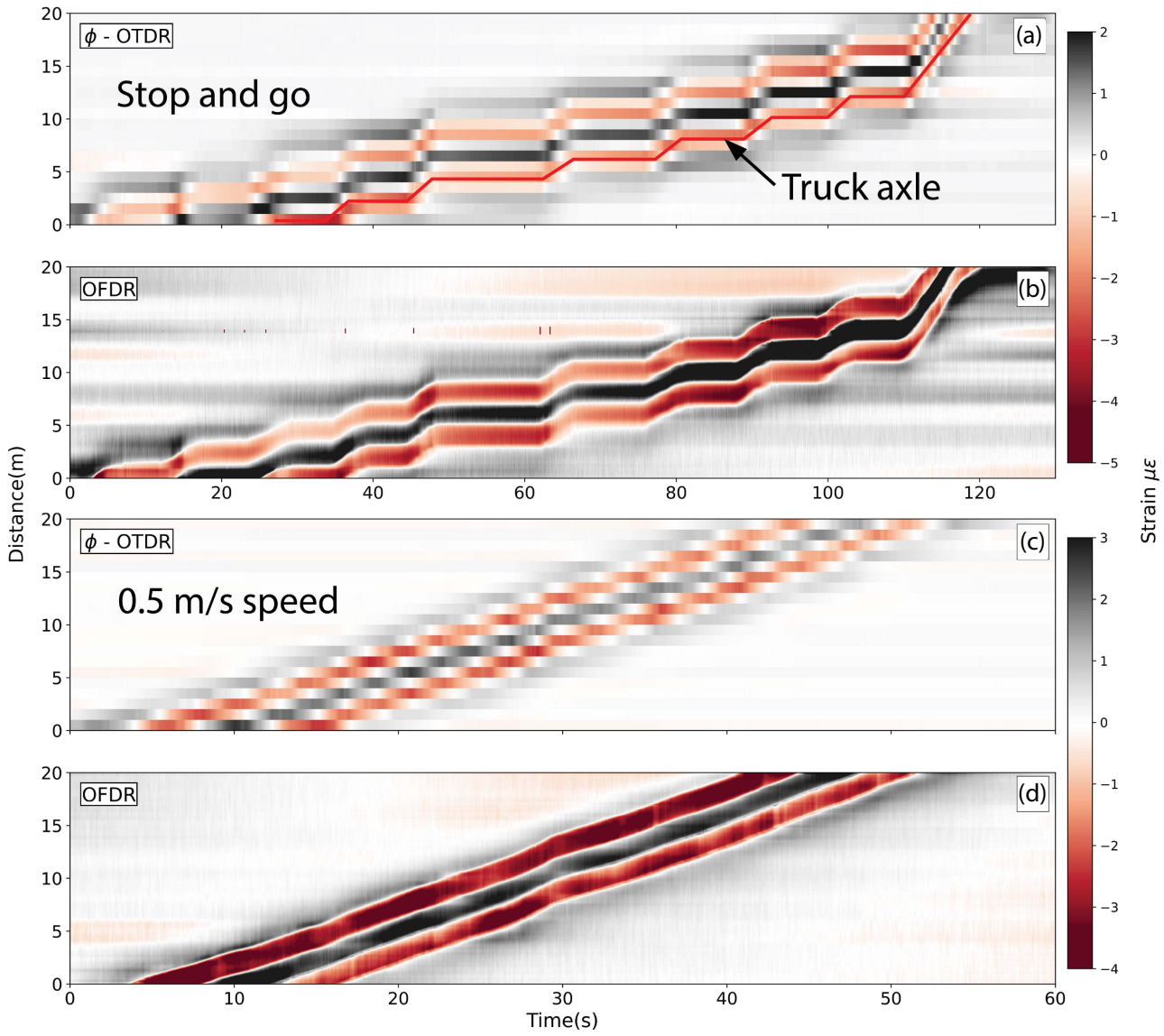

Figure 4.12: Strain amplitude images for both technologies during the verification tests. The sensing cables used are 75 and 115 cm from the road's shoulder for OFDR and ϕ–OTDR, respectively and embedded beneath 3.175 cm of AC. The truck's wheels were placed over the OFDR cable's location.

4.6 Test Cases of ϕ-OTDR Sensitivity

In the previous section, ϕ–OTDR has been demonstrated as capable of measuring longitudinal strain within pavement while a relatively large vehicle moved along the surface. The

results shown in this section demonstrate the sensitivity of the embedded ϕ–OTDR installation to events of much smaller influence on the pavement. The strain measurement results are shown for a runner, pedestrian, bicyclist and finally a medium sized dog moving along the road. The measurements made by ϕ–OTDR for these test cases are shown in Figure 4.13. No attempt was made to simulate these cases by a numerical model due to complex dynamic pavement-load interactions, which requires further study.

The runner induced a longitudinal compressive strain of -0.4 $\mu\varepsilon$ on the pavement over the 2.04 m gauge length of the ϕ–OTDR system. The footfall of the runner is clearly discernable as a train of impulses acting on the pavement. There is a short time when there is no contact between the runner and the pavement, which is evident in the strain measurements. The pedestrian was aways in contact with the pavement, which is why these breaks seen in the runner data do not exist for the pedestrian. The pedestrian also causes a smaller typical strain value of -0.25 $\mu\varepsilon$. This makes sense because the pedestrian does not impact the pavement with the same amount of vertical kinetic energy that the runner does. The cyclist induces a similar value of compressive strain to the pedestrian, about -0.25 $\mu\varepsilon$. However, unlike the truck case shown in Figure 4.12, both axles are not seen with bicycle because of the gauge length of the ϕ–OTDR system. The strain is measured over 2.04 m while the wheel spacing of the bicycle was 1.06 m. Therefore, the location of both axles was always within one gauge length, making it impossible to see a region of decreased strain between them. Finally, the running dog demonstrates the fine sensitivity of ϕ–OTDR to measure small strains within pavement. The dog ran along the pavement inducing a typical compressive strain of -0.02 $\mu\varepsilon$ (-20 nε) on the sensing fiber within the pavement.

This sensitivity study shows how ϕ–OTDR can be used to monitor the material response in pavement at exceedingly small strains and even possibly be used to detect and track events as small as an animal walking on the road. None of these events are below the noise floor of 2 nε demonstrated by Figure 4.6. Even the case of the running dog exhibits a signal to noise ratio (SNR) of 17 dB defined as:

$$SNR = 10 \log \left(\left(\frac{A_{signal}}{A_{noise}} \right)^2 \right) \tag{4.2}$$

where A_{signal} is the root-mean-square amplitude of the signal (14.1 nε for the dog) and A_{noise} is the root-mean-square amplitude of the noise (2 nε for the ϕ–OTDR system). This indicates that even much smaller strain events than the dog running can be reliably measured with ϕ–OTDR

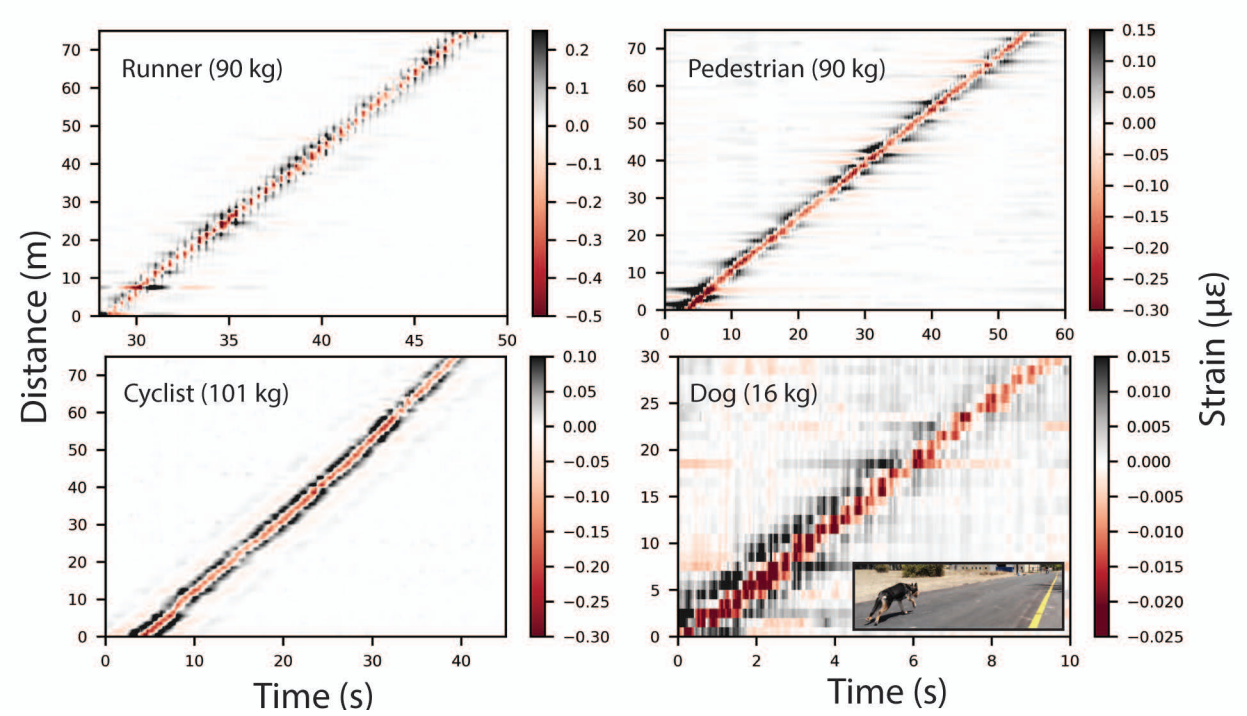

Figure 4.13: Strain amplitude images of the ϕ–OTDR measurements made on the test road when a runner, pedestrian, cyclist, and dog moved along the road.

4.7 Applications of ϕ–OTDR for monitoring roadways

This study has demonstrated that ϕ–OTDR is capable of measuring strains within pavement systems when the sensing fiber is coupled to the system of interest. This application of using ϕ–OTDR to monitor an asphalt pavement system opens the possibilities for assessing the condition of pavements and in-turn informing its design and management. Mechanistic-empirical pavement design relies on performance indicators which for asphalt pavements include rutting, alligator-, longitudinal-, and transverse-cracking, and smoothness [151]. The deformation-based performance indicators, such as rutting and cracking, may be possible to quantify using pavement-embedded ϕ–OTDR by examining the changes in strain levels that are caused by vehicles as a pavement system ages. Furthermore, due to its high acquisition rates and sensitivity, ϕ–OTDR has been shown in the literature as being able to measure road noise [164, 165]. The tandem capabilities of dynamic strain measurement and high frequency noise quantification make ϕ–OTDR an attractive tool for measuring both deformation and smoothness characteristics of pavement systems over long distances. More studies need to be done to explore these possibilities under controlled road deterioration conditions.

In addition to monitoring a pavement system for its health, ϕ–OTDR can detect ex-

tremely small strain events on a road surface that may be too small for making any conclusions about the mechanical condition of the road. However, such information can be leveraged in intelligent transportation systems to track and characterize objects on road surfaces. It has been shown that strain from a pedestrian, cyclist and small animal can be measured with the presented approach. The FHWA reports that in 2019 over 7,000 pedestrians and cyclists were killed by vehicle strikes in the United States [166]. In addition, it estimates that animal strikes on American roads cost more than $8 billion annually [167]. Techniques may be developed for characterizing the strain signatures of people and animals on roads using ϕ–OTDR to develop warning systems or inform the transportation systems of the future. This is an intriguing area for future research.

4.8 Summary of Research Contributions

DDFOS technologies provide the possibility to turn currently passive roadway systems into interactive surfaces much like the touchscreens on smartphones and tablets. The deployment of DDFOS in roadways, and particularly ϕ–OTDR depends on effective installation and mechanical understanding of the roadway systems being monitored. This chapter presents an effective installation strategy for DDFOS at the time of asphalt concrete pavement resurfacing. A processing scheme that reduced the low frequency noise in ϕ–OTDR is presented. The ϕ–OTDR measurements are verified through comparisons with pavement strain gauges and OFDR. The low noise floor and extreme sensitivity of ϕ–OTDR is demonstrated by monitoring strain in the pavement caused pavement-load interaction including a runner, pedestrian, cyclist, and dog moving along the road. ϕ–OTDR is proven as a viable technique for monitoring very small strain in pavements that can be used to inform the understanding of pavement materials and monitor events that happen on asphalt surfaced roads. In addition, due to the known distance range of ϕ–OTDR which can exceed 100 km [168], ϕ–OTDR can potentially monitor long stretches of roadway at extreme sensitivity.

Chapter 5

Superstructure Health Monitoring

This chapter is adapted from an article published in the *Journal of Civil Structural Health Monitoring* on May 5th, 2021.That article is available open-access at the following citation [169]:

Peter G. Hubbard et al. "Dynamic structural health monitoring of a model wind turbine tower using distributed acoustic sensing (DAS)". In: *J Civil Struct Health Monit.* 11. (2021), pp.833-849. DOI: 10.1007/s13349-021-00483-y.

Though ϕ–OTDR had been conceived in-part as a technique for SHM [121], it had not been deployed in civil engineering for this purpose. This chapter demonstrates that ϕ-OTDR is effective for measuring strain in civil infrastructure if its low-frequency noise sources are considered. ϕ-OTDR is validated with OFDR for monitoring dynamic behavior in a model wind turbine subject to dynamic loading in the context of a real-world test case. Enel group, a major power producer, sought to identify distributed technologies for detecting and localizing damage in wind turbine towers. ϕ-OTDR is shown in this chapter to be an effective technology for this purpose being able to both detect changes in global dynamic behavior and localize damage. The installation method of the fiber optic cables is detailed, and the amplitude of the strain measurements is verified using OFDR, which is an impractical tool due to its limited measurement distance. ϕ-OTDR presents the capability of monitoring many structures distributed over a large area from a single centralized IU.

5.1 Background

Wind energy generation capacity worldwide increased from 24 GW in 2001 to 568 GW by the end of 2018 [170]. Over that same timeframe, wind power was responsible for 15% of the increase in electricity generating capability globally [171, 172]. Simultaneously, O&M costs for land-based wind turbines fell by nearly 50% [173]. Procedure improvement and technology advancements have been the main cause for these cost decreases, and in turn have

helped the growth of investments in wind energy. Trends suggest that this will continue, with Denmark's Energinet projecting that fixed O&M costs for onshore wind power will fall 17% between 2020 and 2040 [174]. Currently, manual bolt tensioning is conducted for all bolts yearly on Enel Group's wind turbine towers. This effort accounts for up to 10% of the operational expenditure. Decreasing the necessity for manual bolt inspection and tightening by assessing the structural health remotely is desired to lower this cost. The purpose of this study is to test a novel structural health monitoring technique to detect loose bolts and tower damage. The technique being evaluated is based on distributed acoustic sensing (DAS), a method commonly used to monitor long linear assets such as pipelines for acoustic signals caused by leaks or third party intrusion. The acoustic signals are proportional to dynamic strain in the optical fiber sensing element, making structural health monitoring (SHM) a possibility [19]. The driving factor behind testing this technology for SHM is its large maximum sensing distance of 10km. This may be a solution for monitoring several wind turbines networked together along a single continuous fiber optic cable.

5.2 Structural Health Monitoring of Wind Turbine Towers

Structural health monitoring for wind turbine tower structures has heavily focused on modal analysis, usually from accelerometer data and using widely varying data analytic methods [175–179]. These methods quantify the dynamic structural properties of the towers based on their observed vibrational characteristics. Many studies have been conducted on detecting damage based upon changes in these dynamic properties, which have been met with generally good results [177–181]. Vibration-based techniques evaluate the global structural behavior and can identify changes that indicate damage. They cannot localize where the damage occurs or make observations about the cause, be it bolt loosening or something else. In fact, studies have been done to evaluate modal analysis for its ability to detect loose bolts specifically [182, 183]. These studies found that the first-mode fundamental frequency of large turbine towers can be minimally affected by bolt loosening, making detection difficult. When detection succeeds, localization is still difficult. Practically, there is little value in detecting loose bolts in a turbine tower structure if localization is not possible. This is because the entire tower where a loose bolt is detected would need to be manually inspected. If, however, both detection and localization are possible, engineers would be able to make informed decisions about the importance of addressing bolt tightness on a tower by tower, joint by joint basis. This would provide significant value by reducing O&M costs because currently each bolt is manually tightened yearly regardless of if it is loose or not.

More recently, dynamic measurements of material strain have been made to quantify the behavior of towers and detect damage. Changes in both the strain fields and dynamic properties have been examined for their damage identification abilities. The main challenge of the methods that have been investigated is that material strain has been measured at discrete

locations, again making localization of damage difficult. This has required researchers to make assumptions about the strain fields and use indirect methods for quantifying if damage has occurred between two points. These measurement technologies have included foil strain gauges and Fiber Bragg Grating (FBG) fiber optic sensing [184, 185]. FBG based fiber optic sensing is considered quasi-continuous because it makes measurements at discrete locations along an optical fiber. FBGs are periodic changes in the refractive index of an optical fiber spanning about 50 mm of the optical fiber that are created during the manufacturing process [4]. Strain is measured at the specific location of the FBG.

This study investigates DDFOS for monitoring wind turbine towers. In the case of wind turbine towers, the geometry leads perfectly to this type of sensing. A tower can be measured with vertical sensing lines that are directly adhered to the extreme axis extents of the tower. When distributed strain measurements are made at sufficiently high rates that the natural vibrational frequencies of the structure can be measured without time-aliasing, a comprehensive observation set of the structure can be made. These observations fully resolve the 3-D dynamic structural behavior including vibrational modes and magnitudes, while giving the added benefit of being able to localize strain concentrations caused by damage or bolt loosening over the tower length.

5.3 Experimental Configuration

A model wind turbine tower was constructed to emulate the behavior of a full-scale tower. Flanged pipe sections were chosen due to their low thickness-diameter ratio. The cross section of the flanged pipe was chosen to have an inner diameter of 30.810 cm, a thickness of 0.365 cm (10 gage), and an outer flange diameter of 38.43 cm. The bolt pattern on the flanges consisted of 8 bolt holes equally radially spaced on the flanges with a bolt centerline diameter of 35.56 cm. Six pipe sections, 1.22 m long each, were used to construct the 7.32 m tower. Each flange had slots cut 90° apart up against the pipe body to allow the fiber optic sensing cables to be threaded through the joints while remaining attached to the tower. The flanges were continuously welded on the inside of the pipe and tack welded on the outside of the pipe. The pipe sections were connected to each other with 0.794 cm bolts using a torque gun.

The fully constructed tower is shown in Figure 5.1. The tower was welded at the top and bottom to steel plates. The top plate was used to mount a vibration generator and the bottom plate was used to bolt the tower to a strong floor. The vibration generator was bolted to the top plate using 2.54 cm bolts tightened with a torque gun. To ensure proper load transfer, steel gusset stiffeners were attached to the base and first flange above the base. 10 steel stiffeners were attached to the base of the tower. They were placed asymmetrically, with 5 clustered at the north and south extent of the tower. Similarly, the first flange was asymmetrically stiffened, with 6 stiffeners clustered at each the north and south extent. These orientations stiffened the north-south axis more than the east-west direction. The vibration generator was configured to create a 1-D sinusoidal force in the

north-south direction. The stiffeners were placed for safety to prevent tower collapse caused by local yielding where the maximum bending moment would be experienced during forced vibration.

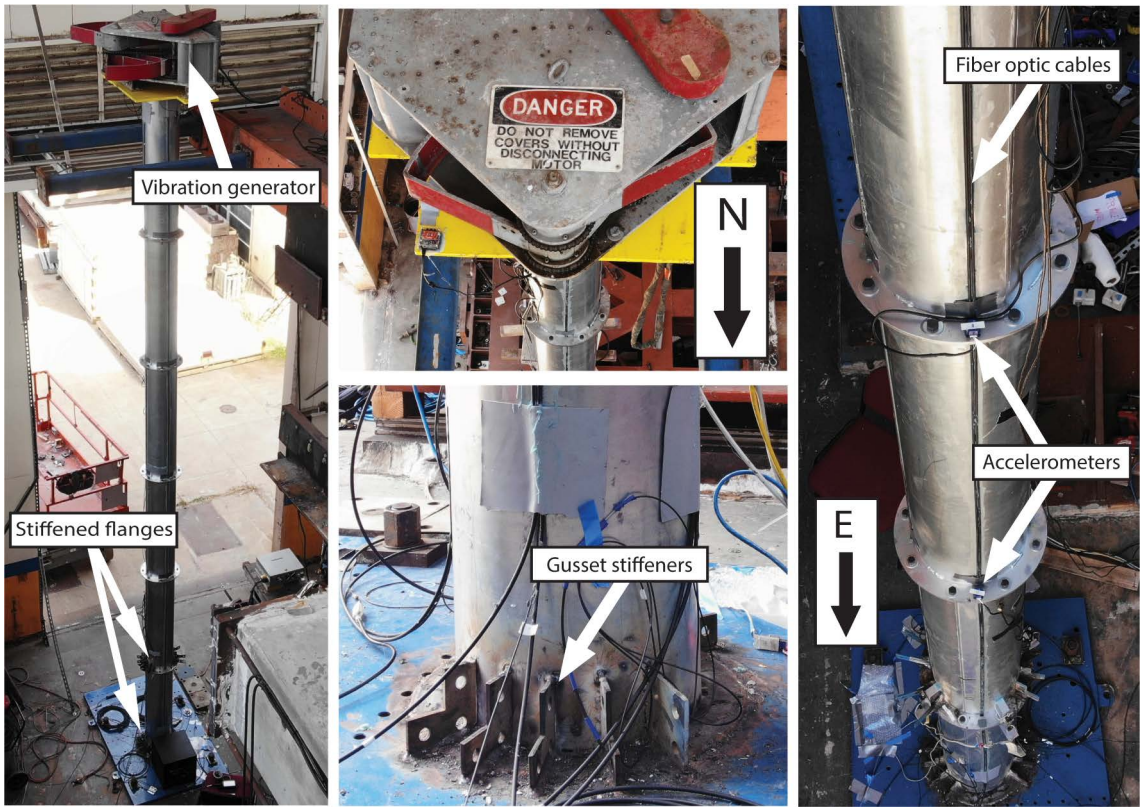

Figure 5.1: Photographs of the experimental configuration including the location of the vibration generator, stiffened flanges, fiber optic cables and accelerometers.

The vibration generator consisted of two steel baskets that spin opposite one another in the horizontal plane. This specific machine was designed for testing full-scale structures under dynamic loads and its design is detailed in [186]. The rotation of the two baskets generates a 1-D sinusoidal force. The maximum output inertial force exerted by this type of vibration generator is a function of the mass and speed of rotation of the baskets. The mass of the vibration generator and top plate were measured to be 245 kg and 150 kg, respectively.

This vibration generator was used because the configuration mimics the mass distribution of a wind turbine and true dynamic loading could be created to resonate the structure, as opposed to controlled displacement. The mass of the vibration generator and mounting plate simulates the mass of the nacelle, gearbox, generator, rotor hub and rotors of a full-scale wind turbine. When the vibration generator is off, free vibration tests were conducted by displacing the top of the tower to directly excite the first-mode natural frequency. The

vibration generator was only turned on to resonate the structure and cause damage to be detected by the employed sensing system, so the forcing magnitudes produced were not meant to simulate typical wind loading. NanZee Sensing NZS-DSS-C02 single mode, tightly buffered fiber optic cables were used for OFDR and ϕ-OTDR measurement. The cross-section of this cable is shown in Figure 3.6 and was previously introduced in Chapter 3.

The cables were epoxied continuously to the tower on north, south, east, and west axes using 3M DP8010 plastic structural adhesive. The sensing cables were threaded through slots in the flanges and were unbonded 1.25 cm above and below each flange. The slots were directly against the tower body, so the cables remained flush against the structure continuously. Epson M-A351 accelerometers were adhered to the flanges and the top plate using an industrial adhesive tape, 7 in total were used. The accelerometers were placed on the top of the flange at each joint along the east axis. Figure 5.2 shows instrumentation plan of the tower as viewed from the east.

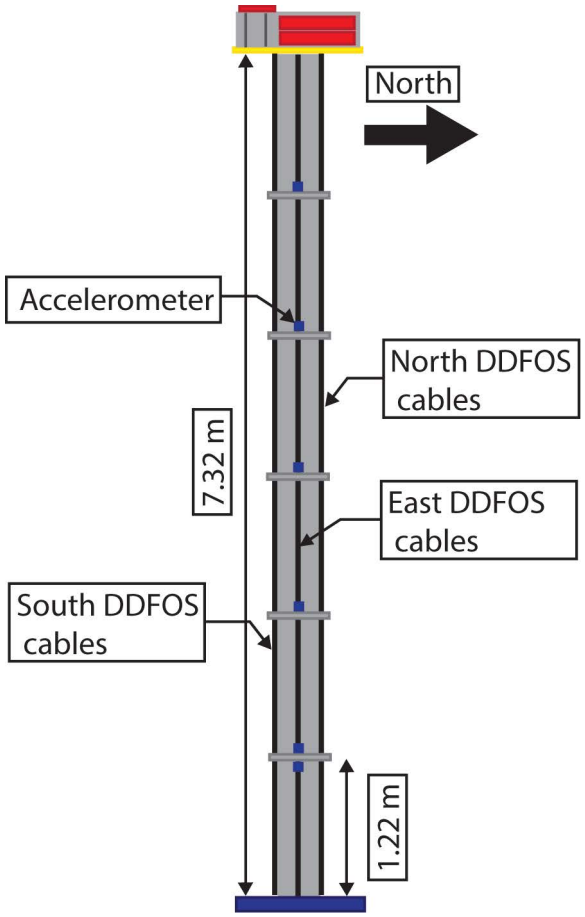

Figure 5.2: Instrumentation plan of the model tower showing a schematic of the 7.32 m-tall tower from East. The instrumentation included longitudinal NZS-DSS-C02 fiber optic cables at each of the four cardinal directions and M-A351 accelerometers located above each flange as well as below the lowest flange. The vibration generator was oriented such that the tower would be excited in the North-South direction.

First, the tower was manually displaced at the top towards the north by 15 cm and allowed to vibrate freely. This test was completed when all bolts were tightened, when one bolt was loosened, and when two bolts were loosened. The bolts that were loosened are indicated in Figure 5.3.

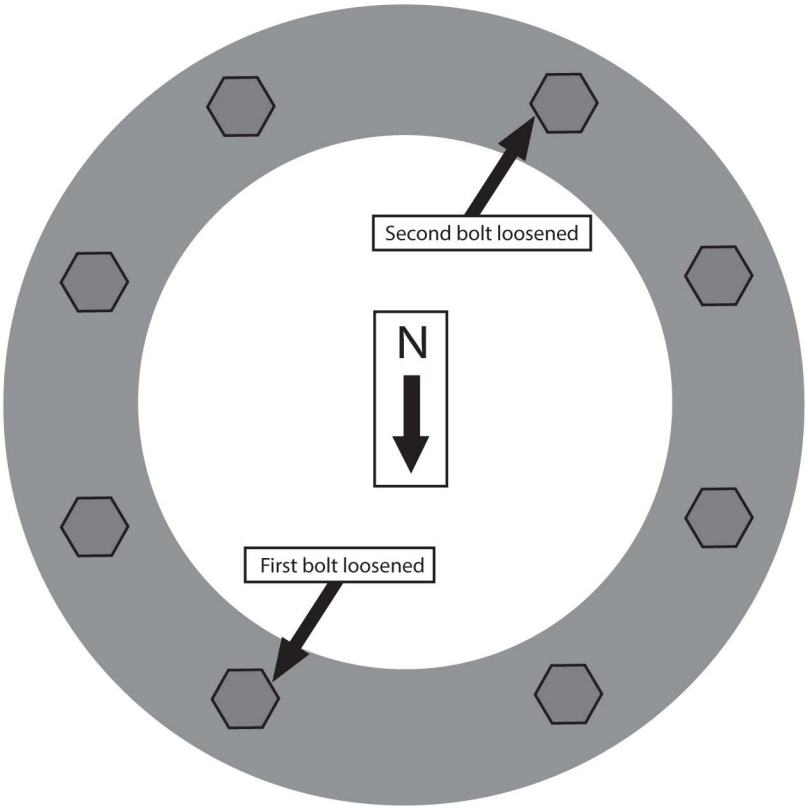

Figure 5.3: Schematic diagram of the locations of the bolts loosened during testing.

After the sequence of free vibration tests, the bolts were all re-tightened and the tower was vibrated using the vibration generator. The generator was ramped from approximately 0.3 Hz, its idle speed, to approximately 3 Hz. The first mode natural frequencies of the north-south and east-west axes were both less than 3 Hz, so the tower briefly was excited at its resonant frequency during each ramp. The ramping took approximately 45 seconds each, and the generator was immediately shut off when it finished speeding up. This process was repeated three times. To compare the DFOS results with the industry accepted modal analysis methods, the dynamic properties of the tower were first calculated using the accelerometer data for each test. The damping ratios were calculated using the log-decrement method, which is valid for small damping ratios. Also, when the damping ratio is sufficiently small, the damped and undamped natural frequencies can be considered equal. The natural frequencies can then be determined using the accelerometer data by calculating the power spectrum as:

$$PS[m] = \Sigma_{n=0}^{N} r_{xx}[n] e^{-\frac{j2\pi mn}{N}}, \quad m = 0, 1, 2, 3...N \tag{5.1}$$

Testing condition	East-West Natural Frequency (Hz)	North-South Natural Frequency (Hz)	Damping Ratio %
Bolted Tower	1.21	1.41	0.49
One Bolt Loosened	1.17	1.39	0.44
One Bolt Loosened	1.16	1.38	0.46

Table 5.1: Natural frequencies determined by accelerometers during the free vibration tests

where r_{xx} is the autocorrelation of the time series. It was observed that the tower possessed two clear first mode natural frequencies because of the asymmetrically stiffened base and first flange. The north-south axis possessed a natural frequency slightly higher than the east-west axis. Each natural frequency and damping ratio as measured with the Epson M-A351 accelerometers during the free vibration tests are shown in Table 5.3. The damping of tower is not significantly changed by bolt loosening. The variability of the calculated damping ratios is considered within the repeatability of the test setup.

5.4 Interpretation of Free-Vibration Datasets

5.4.1 OFDR

OFDR can measure strain with high spatial resolution, but limited range, making it ideal for laboratory-scale experiments. An example strain profile from the north side of the tower at a discrete time during the free vibration test is shown in Figure 5.4. During this test, the tower was displaced in the north direction at the top by 15 cm and allowed to vibrate freely. All bolts were tight during this example. The strain profile reveals localized details of the strain distribution. The strain peaks are located at the flange connections of the tower. Strain localizes at these connections, reaching values over 400 $\mu\varepsilon$ for this test, and is less than 50 $\mu\varepsilon$ elsewhere. The peaks in the strain stretch over 0.25 m for the lowest three flanges and 0.1 m for the top two flanges. This indicates that not only do the lower flanges exhibit more strain, but the deformation is exhibited over a larger distance.

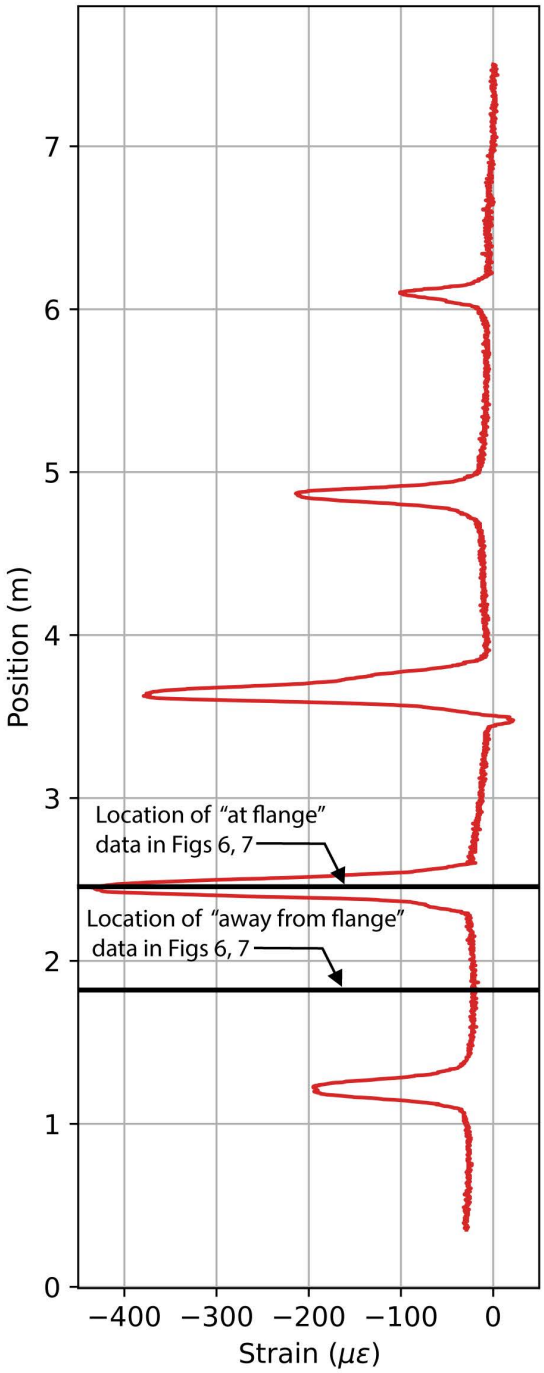

Figure 5.4: OFDR strain profile of tower under free vibration with all bolts tight. The data shown are from approximately 0.5 s after the tower was displaced to the north and allowed to oscillate. The locations of subsequent time series shown in Figures 5.5 and 5.6 are indicated.

Time series measurements can also be evaluated at specific locations, or channels, within the OFDR data. Figure 5.5 shows two of these time series for channels located at the flange and away from the flange, the exact locations are shown as black lines in Figure 5.4. These time series are from the north side of the tower during free vibration. As shown, the signals are different in composition. The time series located away from the flange experiences double the amount of compression as it does tension, while the data from the flange location has a higher amplitude on the tension side. So, it can be observed directly that most of the extension associated with the tower deflecting towards the south is accommodated at the flanges, while the tower body away from the flange experienced compression when the tower deflects towards the north.

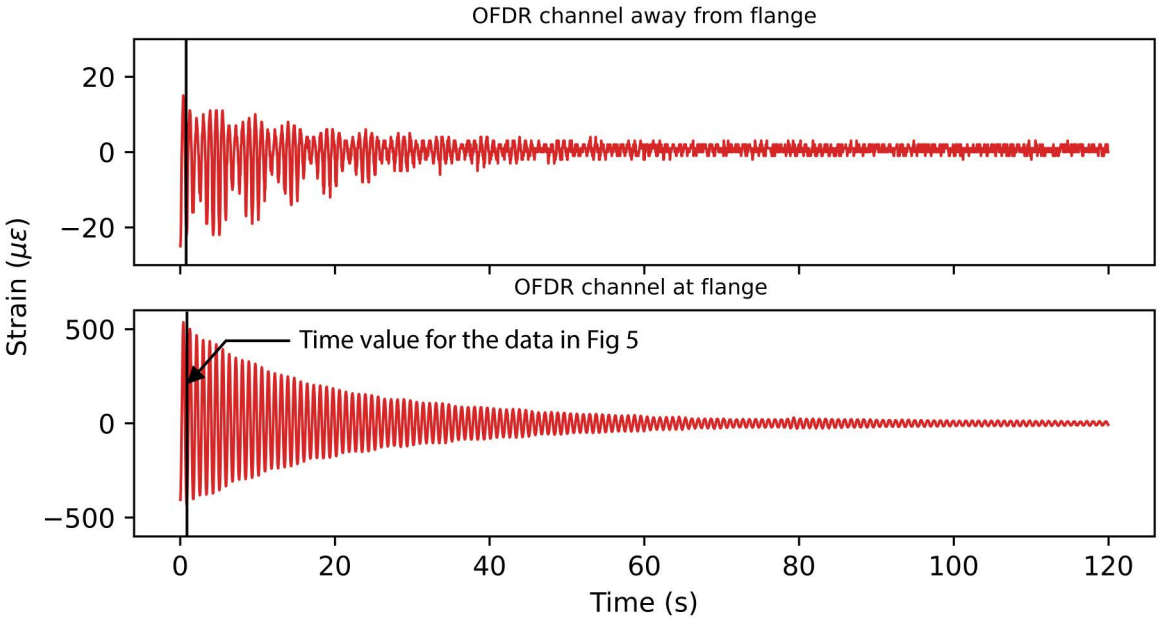

Figure 5.5: OFDR time series from the north side of the tower at the locations shown in Figure 5.4 during 120 s of free vibration after the top of the tower was displaced towards the North. The time point that the data in Figure 5.4 are from is indicated.

A frequency domain analysis can be conducted to evaluate the natural frequencies of the structure. Figure 5.6 shows the power spectrums for channels at and away from a flange. Both dominant frequencies can be clearly seen in these representations which match the accelerometer data with values of 1.21 and 1.41 Hz. The signal to noise ratio (SNR) can also be examined for both channel locations. Away from the flange, the SNRs are 31.3 dB, and 24.3 dB for the two respective frequencies, and at the flange they are 52.6 dB and 27.4 dB. In each case, the strength of the signal is adequate to determine the natural frequencies of the structure.

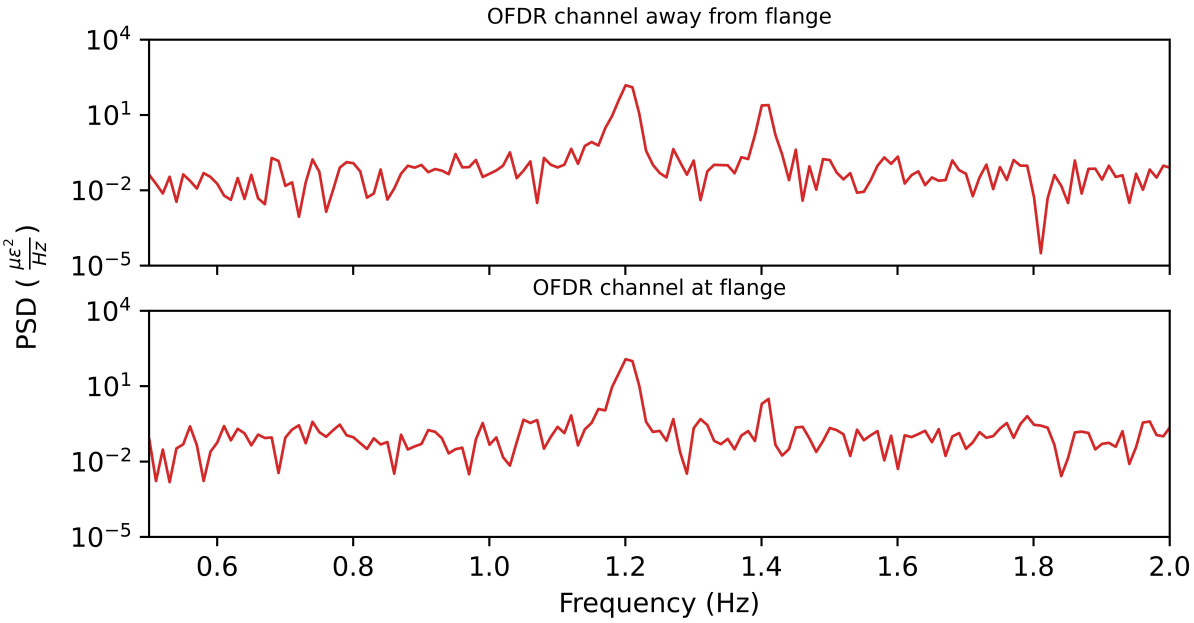

Figure 5.6: Power spectra of the OFDR time-series data shown in Figure 5.5 at the spatial locations shown in Figure 5.4 taken from 120 s of free vibration after the top of the tower was displaced to the North.

5.4.2 ϕ-OTDR

Typical ϕ-OTDR strain time-histories are shown in Figure 5.7 for readout channels located on the north and south sides of the tower during the same free vibration test used for Figs 5, 6 and 7. To mitigate the optical and thermal noise at low frequencies, a Butterworth digital high-pass filter with a cutoff frequency of 0.5 Hz was used. As expected, the north and south sides are 180° out of phase with each other and have similar amplitude and damping behavior.

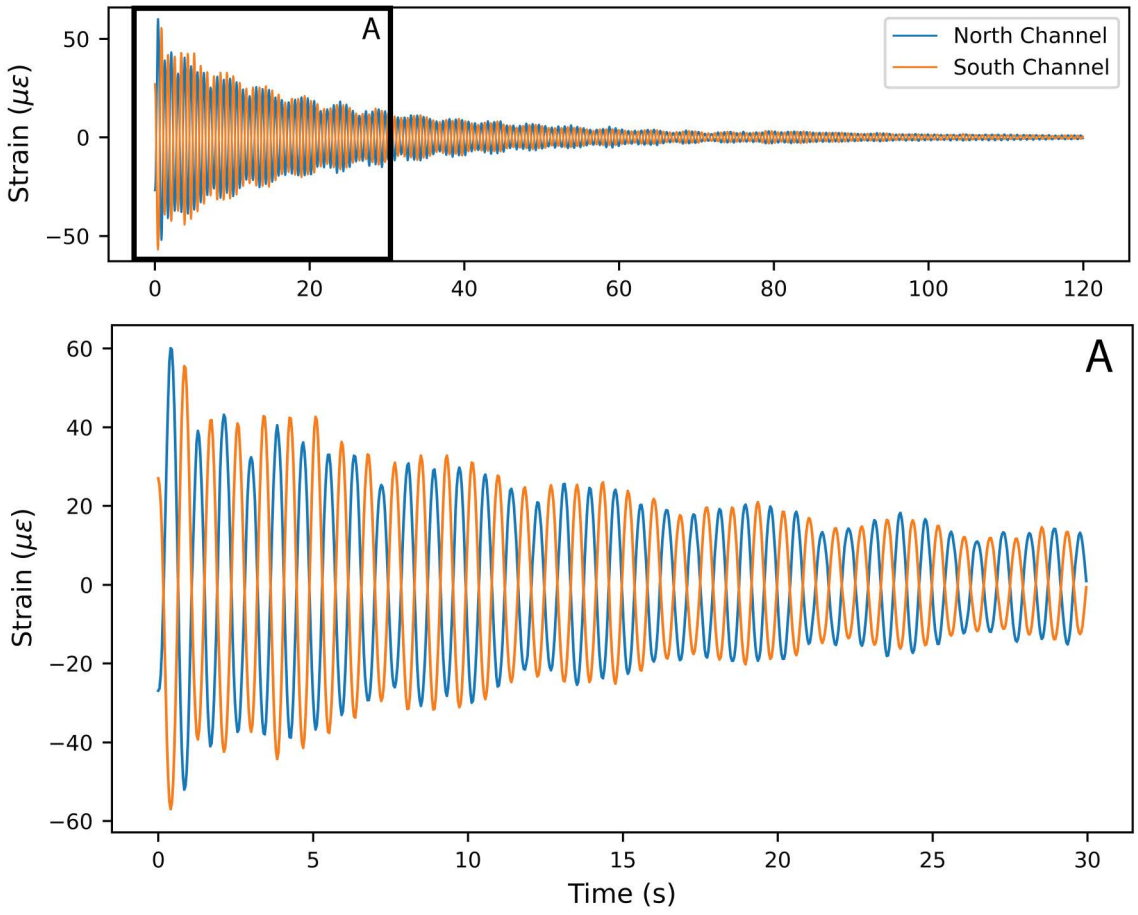

Figure 5.7: Strain time-series from opposite North/South ϕ–OTDR channel locations during the free vibration test when the top of the tower was displaced and the tower was allowed to oscillate. (A) shows with a closeup of the two time-series to clearly display the 180^o phase difference between them and matching amplitude.

The time series can be evaluated for damping behavior and natural frequencies present in the same way as the accelerometer and OFDR data. This result is shown in Figure 5.8. When the power spectrum is examined, there are two prominent peaks visible at 1.21 and 1.41 Hz. The SNR of these peaks are 47.5 and 30 dB, respectively.

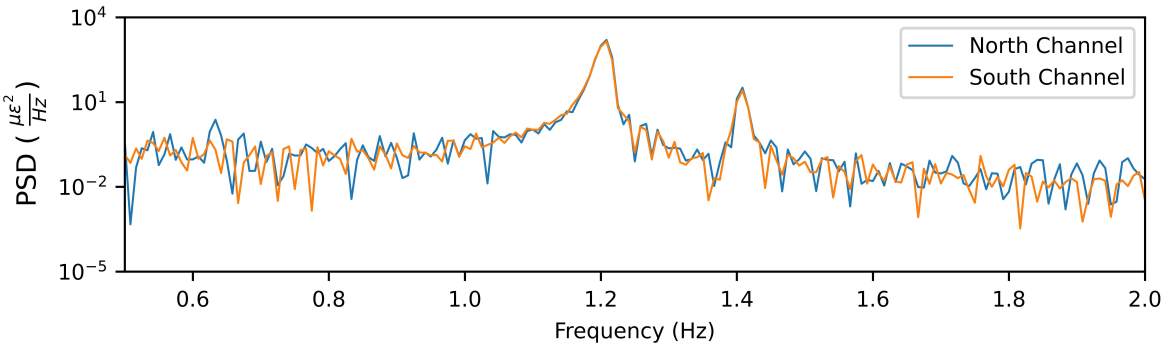

Figure 5.8: Power spectra of the time-series shown in Figure 5.7 from opposite North/South ϕ–OTDR channel locations from 120 s of free vibration after the top of the tower was displaced to the North.

5.5 Loose Bolt and Damage Detection

The DDFOS technologies have been evaluated for their ability to detect damage both directly and through a shift in the natural frequencies of the structure.

5.5.1 Direct Detection of Loose Bolts

Directly identifying opening at the flanges on the lab specimen is straight forward for OFDR because of its fine spatial resolution. ϕ-OTDR, on the other hand, has a spatial resolution close to its gauge length of 2.04 m. This makes localization of phenomena on a laboratory specimen challenging. Only a few independent readouts are possible on the length of tower examined in this study. Nonetheless, localized changes can be determined but must be visualized on a channel-by channel basis. The location of readout channels is especially important for ϕ-OTDR because each channel represents the total strain from $\pm$g/2 from that location.

OFDR

OFDR is capable of detecting strain at flanges with loose bolts directly. Figure 5.9 shows the directly measured strain during the free vibration tests with conditions of no loose bolts, one loose bolt and two loose bolts. Both the north and south strain profiles are shown for the same time indicated in Figer 5.5, which corresponds to one period of vibration from the time of release. Due to the difficulty in controlling the vibrational mode and manually applying the displacement, Figure 5.9 also shows the strain distribution normalized by its integral. This plot gives an important representation of the change in deformation mechanism between the three conditions.

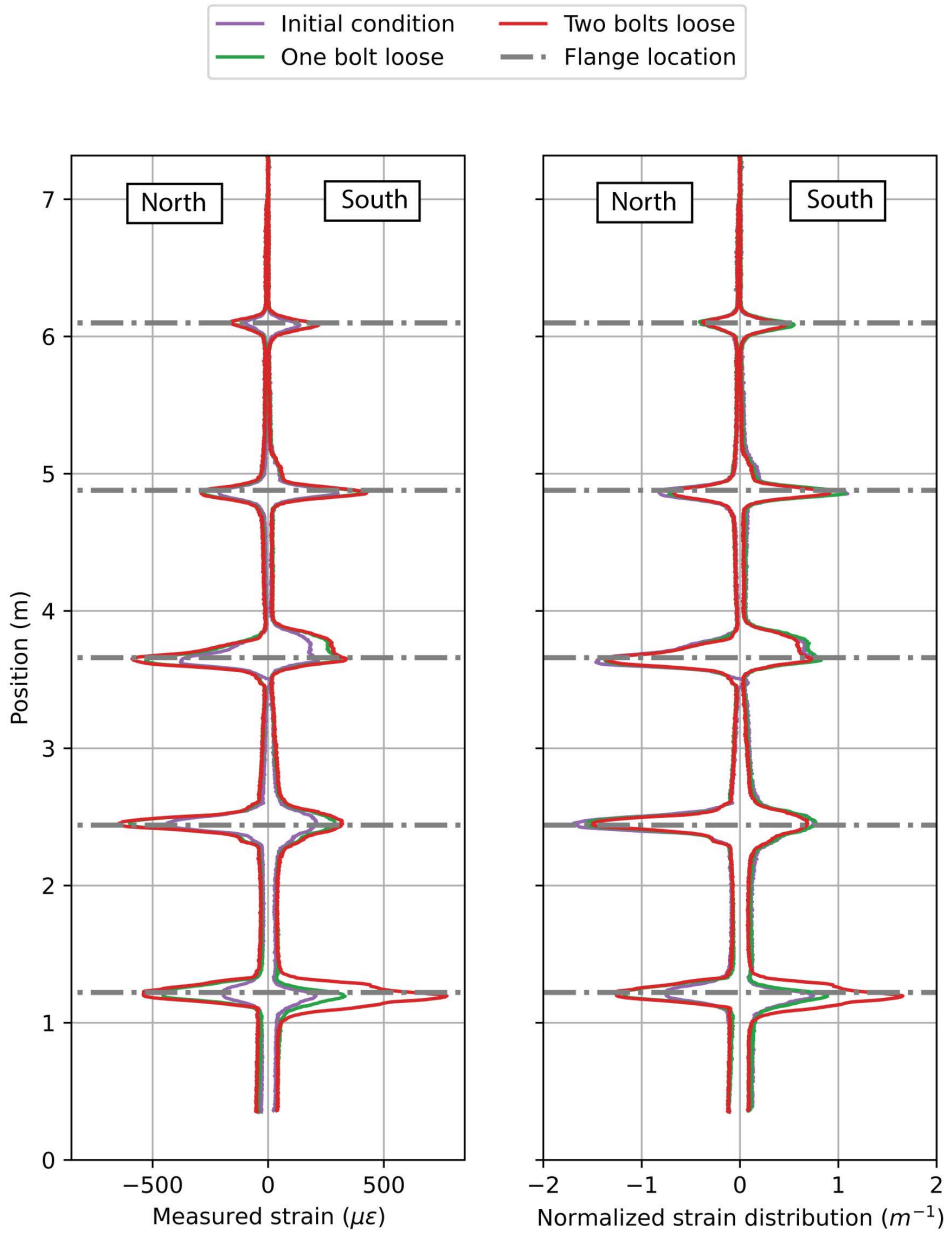

Figure 5.9: Normalized strain profiles measured with OFDR from free vibration tests when zero, one and two bolts were loosened and the same test was repeated. The profiles were created by taking the same approximate measurement time point indicated in Figure 5.5 which corresponds to the peak (on the South) or trough (on the North) after one period of vibration. Due to variability in the magnitude of the applied displacement before vibration, each profile is normalized by its integral so that relative differences can be examined.

As expected, there are large strains exhibited at the first flange where the bolts were loosened. The strain is largest on the north side of the tower when the first bolt is loosened. When the second bolt is loosened the south strain increases at the first flange. The percentage of total deformation accounted for by the first flange increases as well. The flanges where bolts were not loosened account for larger proportions of the total deformation when there is no damage. This proportion decreases as the strain is focused at the first flange.

The spatial strain data can be numerically integrated in space to calculate the cumulative displacement. This is be done for the regions surrounding the flanges to determine flange opening. Figure 5.10 shows the flange opening computed in this way, normalized by the sum of all flange openings. Like Figure 5.8, the opening at flange 1 contains a larger proportion of the total flange openings as bolts are loosened. The very small magnitude of these openings should be noted. The smallest measured opening was at flange 5 and measured 15µm, while the largest was at flange 1 and measured 138µm.

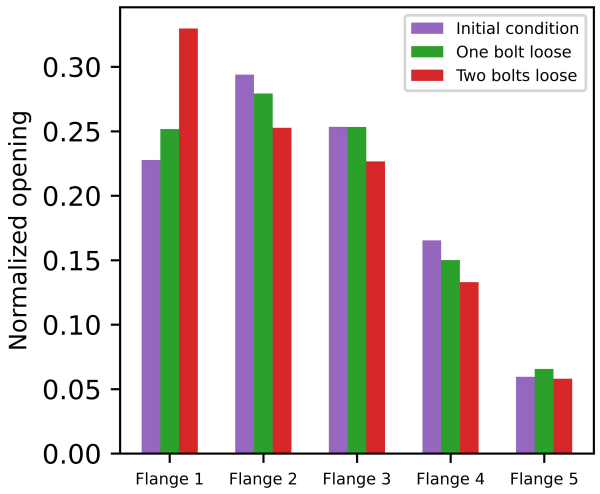

Figure 5.10: The normalized opening at each flange during free vibration when zero, one and two bolts were loosened. The opening was determined by integrating the strain data to calculate displacement and then normalizing by the total flange opening along the entire tower. This was done to show a relative change in the distribution of flange openings when bolts were loosened.

ϕ-OTDR

Due to the limitations of the laboratory scale for ϕ-OTDR, one readout channel is examined, the gauge length of which spanned the joint where bolts were loosened. Figure 5.11 shows this readout channel for both the north and south sides of the tower during the free vibration test. As shown, there is a clear increase in strain amplitude. For the north side, the maximum

strain values recorded after one wavelength of oscillation were 57, 81 and 86 $\mu\varepsilon$ for the cases of no loose bolts, one and two loose bolts respectively. For the south side of the tower, the strain amplitudes were 61, 82 and 92 $\mu\varepsilon$ for the respective conditions. These strains correspond to elongations in the sensing fiber between 117 and 175 µm for the length of fiber spanning the flange.

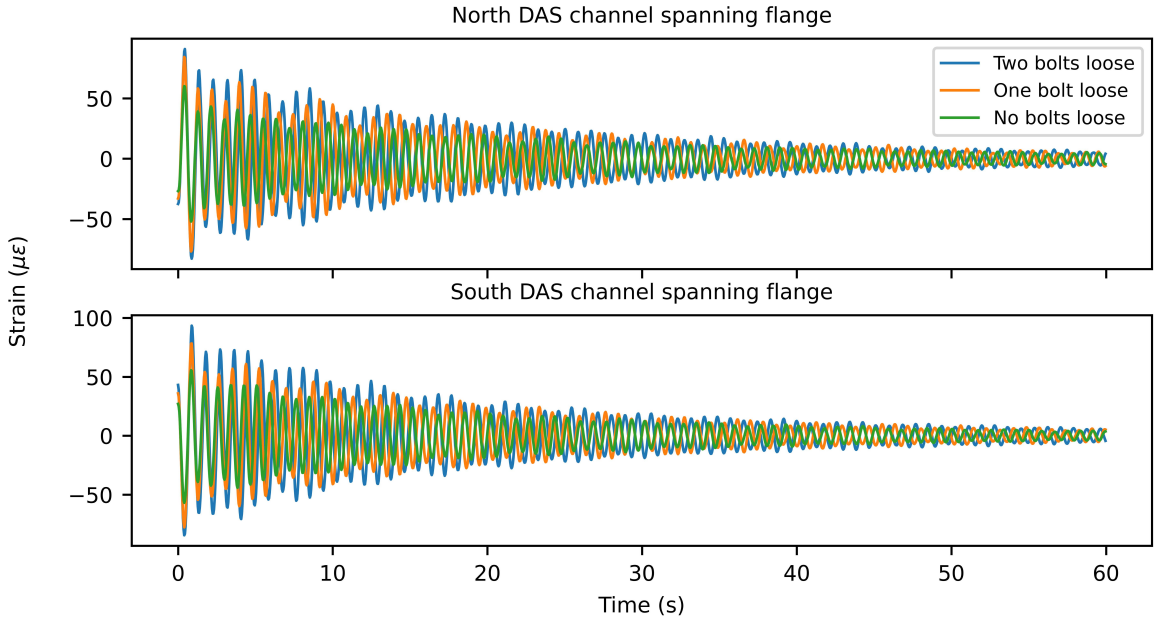

Figure 5.11: ϕ-OTDR strain time-series spanning the first flange during the free vibration tests when zero, one and two bolts were loosened.

5.5.2 Loose Bolt and Damage Detection by Change in Natural Frequency

The natural frequencies of the tower can be measured directly using the time-series data from both OFDR and ϕ-OTDR. In this section, the results of two sets of tests are presented for both technologies; free vibration with varying bolt tightness and forced vibration that caused localized material yielding. Each damage state resulted in altered natural frequencies of the structure and the technologies are compared for their ability to measure the frequency shifts.

Bolt Loosening

Spectra obtained with OFDR are displayed in Figure 5.12 for channels located at and away from a flange during free vibration tests with bolt loosening. The power spectra of the strain

data show a broadening across lower frequencies as bolts are loosened. Also, the peak natural frequency shifts downwards when bolts are loosened versus when they are not. Downward shifts occurred for both axes' first mode natural frequencies and were calculated as identical values for channels at and away from a flange opening.

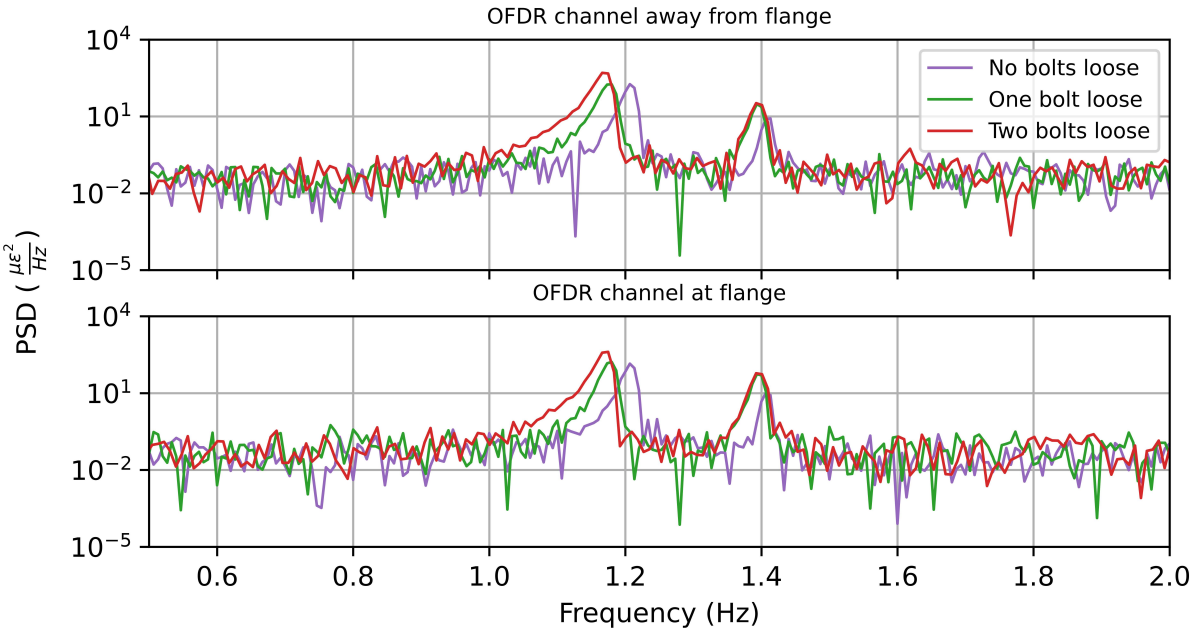

Figure 5.12: Power spectra of OFDR strain time series measurements during the free vibration tests when zero, one and two bolts were loosened at the first flange. The power-spectra were calculated for the locations indicated in Figure 5.4.

The stiffer north-south axis exhibited natural frequencies of 1.41, 1.40 and 1.39 Hz for each condition, while the east-west axis had frequencies of 1.21, 1.18 and 1.17 Hz for each respective condition of all bolts tight, one and two bolts loose. In addition to the shift in natural frequency, the width of the spectrum, specifically in the condition when two bolts were loosened, widen with a tail that stretches toward the lower frequencies. The frequency information gathered by ϕ–OTDR also shows frequency shifts during bolt loosing as well as similar broadening of the spectra when bolts are loosened. These results are shown in Figure 5.13.

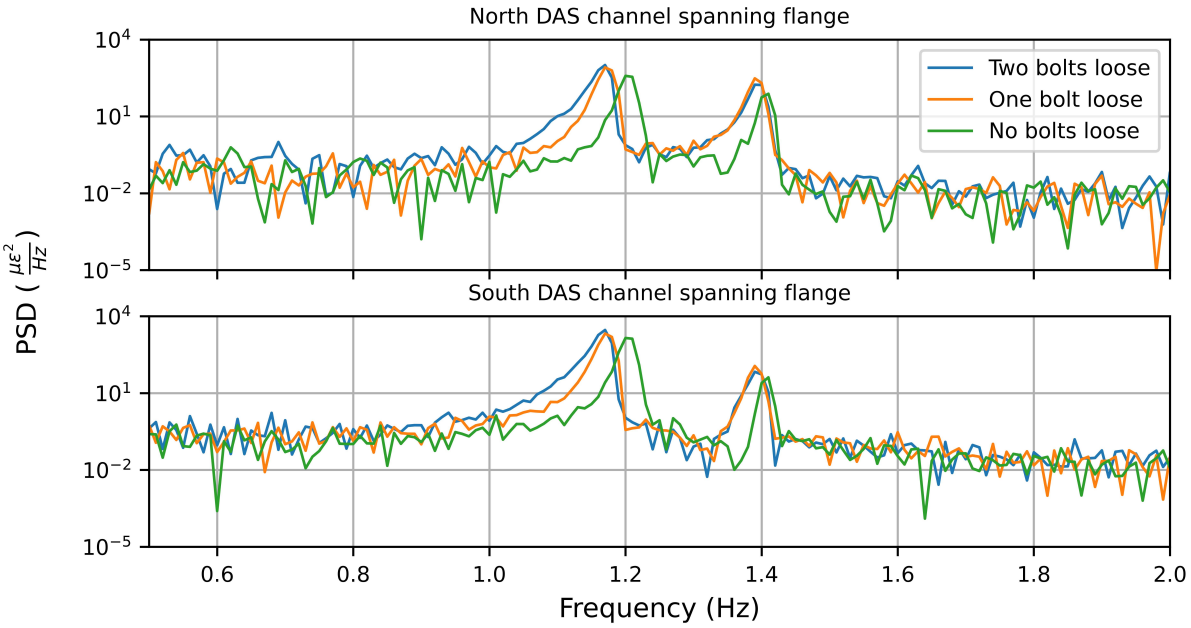

Figure 5.13: Power spectra of ϕ-OTDR strain time series measurements for measurements channels and the North and South sides spanning the first flange during the free vibration tests when zero, one and two bolts were loosened at the first flange.

The peak frequencies for the stiffened axis were 1.41, 1.40 and 1.39 Hz, while the peak frequencies for the unstiffened axis were 1.20, 1.17 and 1.17 Hz for the cases of no bolts loose, one and two bolts loose, respectively.

Damage due to Forced Vibration

After the bolt loosening tests, a similar comparison was conducted for the tower by vibrating it near its resonant frequency repeatedly with the vibration generator. The tower experienced localized material yielding at the first flange during the resonance testing. An example of this damage is shown in Figure 5.14(a), where the flange separation at the northern extent of the tower is shown. Figure 5.14(b) and 5.14(c) show stills from a forced vibration test, where the extent of the deflection can be seen to both the north and south.

Figure 5.14: (a) Flange separation at the northern extent of the tower after the first forced resonance; the tower deflecting during forced vibration to the South (b) and North (c).

The spectra were examined for both OFDR and ϕ–OTDR before and after each test. Figure 5.15 shows the comparison of natural frequencies as determined by both technologies.

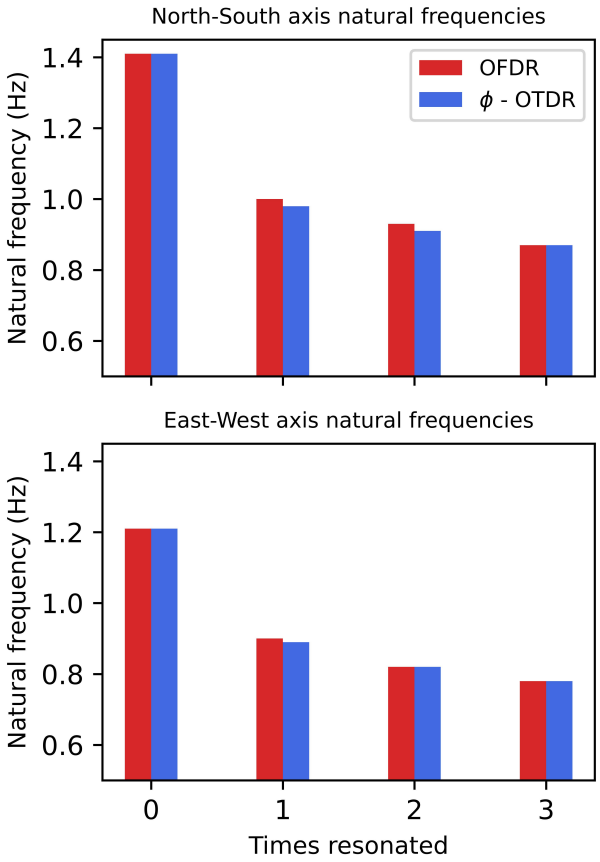

Figure 5.15: Natural frequencies measured before and after each forced vibration test using OFDR and ϕ–OTDR. The vibration generator was ramped up in frequency until the tower began to resonate and then it was slowed to a stop. 120 s of vibration after the vibration generator was stopped was used for the natural frequency measurements. The same measurements locations were used as Figures 5.12 (at the flange) and 5.13 (North).

The natural frequencies match for almost every measurement. However, where the slight mismatching comes in is a matter of one frequency bin in the power spectrum. For consistency, the spectra were calculated with data sampled at 25 Hz for both technologies. This required decimation by a factor of 160 for the ϕ–OTDR data. Then, 1000 datapoints of the time series were used to compute the power spectra. This process results in frequency resolutions of 0.0125 Hz. The largest difference in natural frequency determination between the two technologies was one frequency bin, which can be attributed to using a relatively small number of samples for the calculation.

5.6 Validation of ϕ–OTDR as a Viable SHM Technique

To validate the ϕ–OTDR measurements, both datasets can be converted from strain with different gauge lengths to their equivalent cumulative displacement fields. This requires some understanding of the measurement principles used by each technology. In OFDR, strain readings are made for each 2.6 mm of fiber length. The cumulative displacements can be calculated by integrating spatially over the fiber length at each point in time, much as was done in the previous section to quantify the openings observed at the flanges during vibration. ϕ-OTDR fundamentally measures the optical phase shift over a gauge length of the sensing fiber, 2.04 m in this study. This optical phase shift is then converted to a strain measurement. To compute the displacement field for ϕ-OTDR, Equation 2.28 can be multiplied by the gauge length such that:

$$dU = \frac{d\phi\lambda}{4\pi n\xi} \tag{5.2}$$

where dU is the displacement over a single gauge length. The sensing fiber's total elongation can be determined by using equation 4 to calculate the displacement for each gauge length along a sensing fiber and summing. The spatially integrated OFDR measurements and spatially accumulated ϕ-OTDR measurements at each time can be analyzed as time series data, still sampled at the original 25Hz. An example of this time series for both OFDR and ϕ-OTDR is shown in Figure 5.16 as the cumulative elongation at the top of the north side of the tower during free vibration. The measurements made from OFDR and ϕ-OTDR match incredibly well. The average percent error in the ϕ-OTDR data, with the OFDR data as the reference point, is -4.4%. This is sufficient to conclude that ϕ-OTDR is effective at measuring strain and therefore displacement in a SHM application; it is comparable to the state-of-the-art OFDR system.

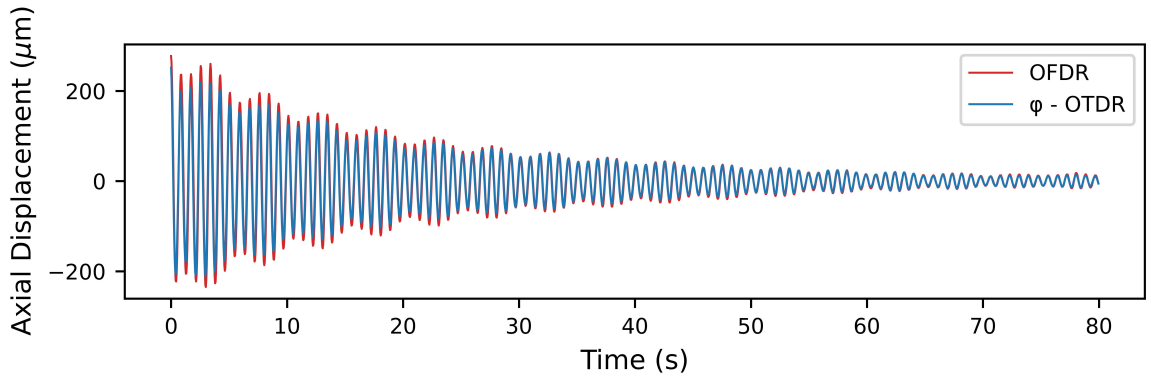

Figure 5.16: Displacement time-series for the top of the tower in the direction of the sensing fiber during free vibration as calculated from both OFDR and ϕ–OTDR by integrating the OFDR measurements and converting the ϕ–OTDR measurements to relative displacement and then summing non-overlapping measurements along the tower.

By calculating the time-series shown in Figure 5.16 at each readout point for both OFDR and ϕ-OTDR and taking their envelope, Figure 5.17 is produced. This figure shows the cumulative elongation of both sensing fibers during 80 seconds of the free vibration test. In addition, two spatial profiles at 0 and 40 seconds comparing the OFDR and ϕ-OTDR measurements are shown. This figure shows that the dynamic displacement measurements made by ϕ-OTDR and OFDR agree at all locations on the sensing fiber. Furthermore, it shows that the correlation between the datasets is not amplitude dependent. Figure 5.17 also demonstrates the readout resolution difference between the technologies. ϕ-OTDR is shown as individual blue lines in the 3-D plot and discrete points in the cross-sections because measurements have a 1.02 m spacing. The OFDR data appears as a solid surface and then solid lines in the 3-D and cross-section plots. This is because the OFDR data is spaced 2.6 mm along the sensing line. Therefore, the individual points cannot be distinguished. Nonetheless, both technologies capture the same behavior and ϕ-OTDR is a solution where less dense data is needed and longer sensing ranges are required.

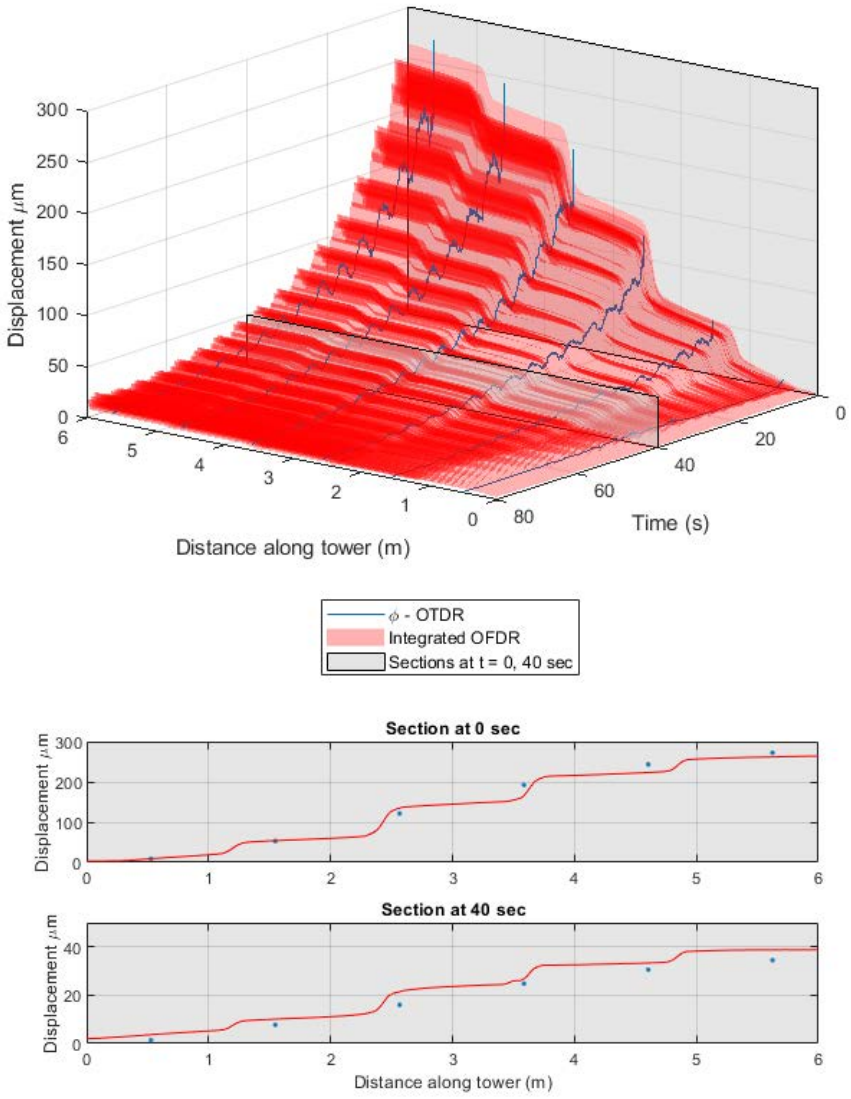

Figure 5.17: 3-D plot of the envelope of north axial displacement in the direction of the sensing fiber versus time and location on the tower for both OFDR and ϕ-OTDR during a free vibration test, and 2-D plots of displacement versus distance at the extracted times of 0 and 40 s. The OFDR data is shown as a red surface in the 3-D plot and red lines in the 2-D plots. The ϕ-OTDR data is shown as blue lines in the 3-D plot and blue dots in the 2-D plot due to its limited spatial data density compared to OFDR.

5.7 Summary of Research Contributions

ϕ-OTDR was used to monitor distributed, dynamic strain in a model wind turbine under free and forced vibration conditions. The measurement distance limited but industry-accepted OFDR was used to validate the dynamic strain measurements made with ϕ-OTDR. ϕ-OTDR was tested for its ability to identify changes in strain and natural frequency associated with bolt loosening and local material yielding. It was found that ϕ-OTDR is capable of quantitatively measuring strain, and in-turn displacement, at the structural frequencies exhibited by wind turbine towers. A thorough comparison of the two technologies proved that ϕ-OTDR and OFDR measure displacement fields within 5% of each other. ϕ-OTDR was shown to be able to measure localized strain associated with the opening of flange joints and detect small changes in natural frequency caused by structural damage. ϕ-OTDR has been demonstrated as an effective and promising technology for SHM of large and distributed structures due to its dynamic measurement capability, high strain sensitivity and maximum measurement distance.

Chapter 6

Conclusions and Recommended Future Works

6.1 Summary and Conclusions

ϕ-OTDR is a promising DFOS technology that has been used extensively in the earth and planetary science community for measuring seismic wave propagation, environmental noise, and vibration signals from anthropogenic events. ϕ-OTDR is a member of a broader family of technologies referred to as DAS or DVS. The most exciting part about ϕ-OTDR for civil infrastructure applications is the combination of dynamic strain measurement precision, high acquisition rate and long measurement distance. The combination of capabilities is currently not available from other DFOS technologies currently used in the civil engineering field. A major gap to implementation, though, was validating the amplitude of ϕ-OTDR measurements in practical installation environments. In the previous uses for monitoring seismic wave propagation scientific studies, the amplitude of the strain measurements was not typically considered, and the accuracy of the strain measurements in the field had not been rigorously verified. Moreover, a thorough investigation of strain measurement amplitudes in realistic field deployments for monitoring infrastructure had not been conducted. This dissertation served to demonstrate that the accurate dynamic strain measurements can be made with ϕ-OTDR, and practical implementations are possible. It was shown that ϕ-OTDR can quantitatively measure the dynamic deformation of soil, pavement and a superstructure all when subject to dynamic loading. Measurements were verified using highly-sensitive velocity transducers, standard strain gauges and another DFOS technique. ϕ-OTDR proved to be able to measure phenomena in infrastructure that other currenlty-used DFOS techniques cannot, due mostly to its superior strain measurement precision and acquisition rates. Overall this dissertation has served to demonstrate ϕ-OTDR as a new tool for monitoring civil infrastructure that offers capabilities that have previously not been possible.

6.2 Recommended Future Works

This dissertation did not explore extending ϕ-OTDR measurements to zero frequency (static strain). The phase noise and temperature induced refractive index changes that manifest as low frequency noise were removed through high pass filtering the measurements. There have been recent advances that make static measurements possible [187]. Such advancements are promising for implementing ϕ-OTDR to simultaneously monitor pseudostatic deformation and dynamic properties. More studies need to be done deploying these DC-coupled instruments within civil infrastructure.

This dissertation also did not examine the extreme sensitivity of ϕ-OTDR measurements to temperature. It has been shown the sensitivities as small as millikelvin are possible [88]. Such sensitivity to temperature also opens the door to monitoring how extremeley small temperature gradients can be indicative to infrastructure health. More work needs to be done to quantify the temperature measurements and separate the temperature and strain effects from phase measurements.

Finally, ϕ-OTDR is a technology that is rapidly advancing. Just during the writing of this document there has been published research on improving ϕ-OTDR techniques in terms of sensitivity, spatial resolution and range [188]. Inevitably the technology will continue to advance and keeping it at the forefront of civil infrastructure research will ensure that these technologies are implemented widely in the future, if it is in the best interest of society to do so.

Bibliography

[1] Anjali Singhvi et al. "Miami's Surfside Condo Was Flawed and Failing. Here's a Look Inside." In: *N.Y. Times* (2021). ISSN: 0362-4331. URL: https://www.nytimes.com/interactive/2021/09/01/us/miami-building-collapse.html.

[2] Campbell Robertson and Sophie Kasakove. "Pittsburgh Bridge Collapses Hours Before Biden Infrastructure Visit". In: *N.Y. Times* (2022). ISSN: 0362-4331. URL: https://www.nytimes.com/2022/01/28/us/pittsburgh-bridge-collapse-biden.html.

[3] J. M. W. Brownjohn. "Structural health monitoring of civil infrastructure". In: *Philos. Trans. Royal Soc. A* 365.1851 (Dec. 2006), pp. 589–622. ISSN: 1471-2962. DOI: 10.1098/rsta.2006.1925.

[4] Kenichi Soga and Linqing Luo. "Distributed fiber optics sensors for civil engineering infrastructure sensing". In: *J. Struct. Integrity Maint.* 3.1 (2018), pp. 1–21. ISSN: 2470-5314. DOI: 10.1080/24705314.2018.1426138.

[5] K. C. Kao and G. A. Hockham. "Dielectric-fibre surface waveguides for optical frequencies". In: *Proc. Inst. Electr. Eng.* 113.7 (1966), pp. 1151–1158. ISSN: 2053-7891. DOI: 10.1049/piee.1966.0189.

[6] D. Colladon. "On the reflections of a ray of light inside a parabolic liquid stream". In: *Comptes Rendus* 15 (1842), pp. 800–802.

[7] Narinder S. Kapany. "Fiber Optics". In: *Sci. Am.* (1960).

[8] Eugene Hecht. *Optics, 5th Edition*. Pearson, 2016. ISBN: 978-0133979091.

[9] D. Gloge. "Weakly Guiding Fibers". In: *Appl. Opt.* 10.10 (1971), pp. 2252–2258. ISSN: 2155-3165. DOI: 10.1364/AO.10.002252.

[10] *Commercial Building Telecommunications Cabling Standards*. Standard. Arlington, VA: Telecommunications Industry Association, 2015.

[11] Arthur H Hartog. *An Introduction to Distributed Optical Fibre Sensors*. Boca Raton: CRC Press, 2017. ISBN: 978-1138082694.

[12] Nikola Zlatanov. "Introduction to Fiber Optics Theory". In: *The Optical Fiber Communication Conference and Exhibition 2017* (Los Angeles, CA). IEEE Computer Society, 2017. DOI: 10.13140/RG.2.2.29183.20641.

[13] R. Juškaitis et al. "Interferometry with Rayleigh backscattering in a single-mode optical fiber". In: *Opt. Lett.* 19.3 (1994), pp. 225–227. ISSN: 1539-4794. DOI: 10.1364/OL.19.000225.

[14] Byeong Ha Lee et al. "Interferometric Fiber Optic Sensors". In: *Sensors* 12.3 (2012), pp. 2467–2486. ISSN: 1424-8220. DOI: 10.3390/s120302467.

[15] Mark Froggatt and Jason Moore. "High-spatial-resolution distributed strain measurement in optical fiber with Rayleigh scatter". In: *Appl. Opt.* 37.10 (1998), pp. 1735–1740. ISSN: 2155-3165. DOI: 10.1364/AO.37.001735.

[16] Andreas Othonos. "Fiber Bragg gratings". In: *Rev. Sci. Instrum.* 68.12 (1997), pp. 4309–4341. ISSN: 0034-6748. DOI: 10.1063/1.1148392.

[17] Christoph M. Monsberger and Werner Lienhart. "Distributed Fiber Optic Shape Sensing of Concrete Structures". In: *Sensors* 21.18 (2021), p. 6098. ISSN: 1424-8220. DOI: 10.3390/s21186098.

[18] Ping Lu et al. "Distributed optical fiber sensing: Review and perspective". In: *Appl. Phys. Rev.* 6.4 (2019), p. 041302. ISSN: 1931-9401. DOI: 10.1063/1.5113955.

[19] SEAFOM. *Measuring Sensor Performance Document – 02 (SEAFOM MSP-02)*. United Kingdom: IOP Publishing SEAFOM Fiber Optic Monitoring Group, 2018.

[20] Zhaoyong Wang et al. "Recent Progress in Distributed Fiber Acoustic Sensing with ϕ-OTDR". In: *Sensors (Basel, Switzerland)* 20.22 (2020). DOI: 10.3390/s20226594.

[21] Bin Lu et al. "High spatial resolution phase-sensitive optical time domain reflectometer with a frequency-swept pulse". In: *Opt. Lett.* 42.3 (2017), pp. 391–394. ISSN: 1539-4794. DOI: 10.1364/OL.42.000391.

[22] W. Eickhoff and R. Ulrich. "Optical frequency domain reflectometry in single-mode fiber". In: *Appl. Phys. Lett.* 39.9 (1981), pp. 693–695. ISSN: 0003-6951. DOI: 10.1063/1.92872.

[23] A. V. Oppenheim, J. R. Buck, and R. W. Schafer. *Discrete-time Signal Processing (2nd Ed.)* Prentice Hall, 1999.

[24] Jianqin Peng et al. "Distributed strain and temperature fast measurement in Brillouin optical time-domain reflectometry based on double-sideband modulation". In: *Opt. Express* 30.2 (2022), pp. 1511–1520. ISSN: 1094-4087. DOI: 10.1364/OE.445143.

[25] M. K. Barnoski and S. M. Jensen. "Fiber waveguides: a novel technique for investigating attenuation characteristics". In: *Appl. Opt.* 15.9 (1976), pp. 2112–2115. ISSN: 2155-3165. DOI: 10.1364/AO.15.002112.

[26] S. D. Personick. "Photon Probe—An Optical-Fiber Time-Domain Reflectometer". In: *Bell System Technical Journal* 56.3 (1977), pp. 355–366. ISSN: 0005-8580. DOI: 10.1002/j.1538-7305.1977.tb00513.x.

[27] Leonid B. Liokumovich et al. "Fundamentals of Optical Fiber Sensing Schemes Based on Coherent Optical Time Domain Reflectometry: Signal Model Under Static Fiber Conditions". In: *J. Lightwave Technol.* 33.17 (June 2015), pp. 3660–3671. ISSN: 1558-2213. DOI: 10.1109/JLT.2015.2449085.

[28] Nicholas Lagakos, J. H. Cole, and J. A. Bucaro. "Microbend fiber-optic sensor". In: *Appl. Opt.* 26.11 (June 1987), pp. 2171–2180. ISSN: 2155-3165. DOI: 10.1364/AO.26.002171.

[29] J. N. Ross. "Measurement of magnetic field by polarisation optical time-domain reflectometry". In: *Electron. Lett.* 17.17 (1981), pp. 596–597. ISSN: 1350-911X. DOI: 10.1049/el:19810419.

[30] Sascha Liehr, Sven Münzenberger, and Katerina Krebber. "Wavelength-scanning coherent OTDR for dynamic high strain resolution sensing". In: *Opt. Express* 26.8 (2018), pp. 10573–10588. ISSN: 1094-4087. DOI: 10.1364/OE.26.010573.

[31] Koyamada Yahei. *New Technique for Distributed Strain Measurement in Optical Fibers with Very High Sensitivity by Making Use of Rayleigh Backscattering*. Proceedings. Institute of Electronics, Information and Communication Engineers, 1998.

[32] Arthur H. Hartog. "Raman sensors and their applications". In: *Proceedings Volume 8421, OFS2012 22nd International Conference on Optical Fiber Sensors*. Vol. 8421. SPIE, 2012, pp. 147–152. DOI: 10.1117/12.974845.

[33] Zhenyang Ding et al. "Distributed Optical Fiber Sensors Based on Optical Frequency Domain Reflectometry: A review". In: *Sensors (Basel, Switzerland)* 18.4 (2018). DOI: 10.3390/s18041072.

[34] Stephen T. Kreger et al. "High Resolution Distributed Strain or Temperature Measurements in Single-and Multi-mode Fiber Using Swept-Wavelength Interferometry". In: *Optica Publishing Group* (2006), ThE42. DOI: 10.1364/OFS.2006.ThE42.

[35] Aldo Minardo et al. "Proposal of Brillouin optical frequency-domain reflectometry (BOFDR)". In: *Opt. Express* 24.26 (2016), pp. 29994–30001. ISSN: 1094-4087. DOI: 10.1364/OE.24.029994.

[36] Emir Karamehmedovic and Ulrich Glombitza. "Fiber optic distributed temperature sensor using incoherent optical frequency domain reflectometry". In: *Proceedings Volume 5363, Emerging Optoelectronic Applications*. Vol. 5363. SPIE, 2004, pp. 107–115. DOI: 10.1117/12.528794.

[37] Juan Clement et al. "Incoherent Optical Frequency-Domain Reflectometry Based on Homodyne Electro-Optic Downconversion for Fiber-Optic Sensor Interrogation". In: *Sensors* 19.9 (2019), p. 2075. ISSN: 1424-8220. DOI: 10.3390/s19092075.

[38] F. P. Kapron, D. G. Kneller, and P. M. Garel-Jones. "Aspects of optical frequency-domain reflectometry". In: *Optica Publishing Group* (1981), WF2. DOI: 10.1364/OFC.1981.WF2.

[39] Mark B. Hausner et al. "Calibrating Single-Ended Fiber-Optic Raman Spectra Distributed Temperature Sensing Data". In: *Sensors* 11.11 (2011), pp. 10859–10879. ISSN: 1424-8220. DOI: 10.3390/s111110859.

[40] Robert C. Youngquist, Sally Carr, and D. E. N. Davies. "Optical coherence-domain reflectometry: a new optical evaluation technique". In: *Opt. Lett.* 12.3 (1987), pp. 158–160. ISSN: 1539-4794. DOI: 10.1364/OL.12.000158.

[41] Yosuke Mizuno et al. "Proposal of Brillouin optical correlation-domain reflectometry (BOCDR)". In: *Opt. Express* 16.16 (2008), pp. 12148–12153. ISSN: 1094-4087. DOI: 10.1364/OE.16.012148.

[42] Kinzo Kishida, Che-Hien Li, and Ken'ichi Nishiguchi. "Pulse pre-pump method for cm-order spatial resolution of BOTDA". In: *Proceedings Volume 5855, 17th International Conference on Optical Fibre Sensors*. Vol. 5855. SPIE, 2005, pp. 559–562. DOI: 10.1117/12.624259.

[43] Xiaoyi Bao and Liang Chen. "Recent Progress in Distributed Fiber Optic Sensors". In: *Sensors* 12.7 (2012), pp. 8601–8639. ISSN: 1424-8220. DOI: 10.3390/s120708601.

[44] Kwang Yong Song and Kazuo Hotate. "Distributed Fiber Strain Sensor With 1-kHz Sampling Rate Based on Brillouin Optical Correlation Domain Analysis". In: *IEEE Photonics Technol. Lett.* 19.23 (2007), pp. 1928–1930. ISSN: 1941-0174. DOI: 10.1109/LPT.2007.908772.

[45] Aldo Minardo, Ester Catalano, and Luigi Zeni. "Cost-effective method for fast Brillouin optical time-domain analysis". In: *Opt. Express* 24.22 (2016), pp. 25424–25431. ISSN: 1094-4087. DOI: 10.1364/OE.24.025424.

[46] Bo Li et al. "Dynamic Strain Measurement Using Small Gain Stimulated Brillouin Scattering in STFT-BOTDR". In: *IEEE Sens. J.* 17.9 (2017), pp. 2718–2724. ISSN: 1558-1748. DOI: 10.1109/JSEN.2017.2657119.

[47] Agnese Coscetta, Aldo Minardo, and Luigi Zeni. "Distributed Dynamic Strain Sensing Based on Brillouin Scattering in Optical Fibers". In: *Sensors* 20.19 (2020), p. 5629. ISSN: 1424-8220. DOI: 10.3390/s20195629.

[48] Dengwang Zhou et al. "Single-shot BOTDA based on an optical chirp chain probe wave for distributed ultrafast measurement". In: *Light Sci. Appl.* 7.32 (2018), pp. 1–11. ISSN: 2047-7538. DOI: 10.1038/s41377-018-0030-0.

[49] Elias Abdoli Oskoui, Todd Taylor, and Farhad Ansari. "Reference-Free Dynamic Distributed Monitoring of Damage in Multispan Bridges". In: *J. Struct. Eng.* 147.1 (2021), p. 04020292. DOI: 10.1061/(ASCE)ST.1943-541X.0002858.

[50] R. M. Liu et al. "Experimental study on structural defect detection by monitoring distributed dynamic strain". In: *Smart Mater. Struct.* 24.11 (2015), p. 115038. ISSN: 0964-1726. DOI: 10.1088/0964-1726/24/11/115038.

[51] Alice Scarella et al. "Dynamic Brillouin Scattering–Based Condition Assessment of Cables in Cable-Stayed Bridges". In: *J. Bridge Eng.* 22.3 (2017), p. 04016130. DOI: 10.1061/(ASCE)BE.1943-5592.0001010.

[52] Agnese Coscetta et al. "Wind Turbine Blade Monitoring with Brillouin-Based Fiber-Optic Sensors". In: *J. Sens.* 2017 (2017), p. 9175342. ISSN: 1687-725X. DOI: 10.1155/2017/9175342.

[53] Lisa N. Wheeler et al. "Measurement of distributed dynamic rail strains using a Rayleigh backscatter based fiber optic sensor: Lab and field evaluation". In: *Transp. Geotech.* 14 (2018), pp. 70–80. ISSN: 2214-3912. DOI: 10.1016/j.trgeo.2017.10.002.

[54] L.N. Wheeler et al. "Use of fiber optic sensing to measure distributed rail strains and determine rail seat forces under a moving train". In: *Canadian Geotechnical Journal* 56.1 (2019), pp. 1–13. DOI: 10.1139/cgj-2017-0163.

[55] Zachary Broth and Neil A. Hoult. "Dynamic distributed strain sensing to assess reinforced concrete behaviour". In: *Eng. Struct.* 204 (2020), p. 110036. ISSN: 0141-0296. DOI: 10.1016/j.engstruct.2019.110036.

[56] Ryan Regier and Neil A. Hoult. "Distributed Strain Behavior of a Reinforced Concrete Bridge: Case Study". In: *J. Bridge Eng.* 19.12 (2014), p. 05014007. DOI: 10.1061/(ASCE)BE.1943-5592.0000637.

[57] J. M. Henault et al. "MONITORING OF CONCRETE STRUCTURES USING OFDR TECHNIQUE". In: *AIP Conf. Proc.* 1335.1 (2011), pp. 1386–1393. ISSN: 0094-243X. DOI: 10.1063/1.3592094.

[58] Luna Innovations Incorporated. *Introducing the ODiSI-B 5.1 for Strain & Temperature*. Virginia: IOP Publishing Luna Innovations Incorporated, 2020.

[59] Luna Innovations Incorporated. *ODiSI 6000: Optical Distributed Sensor Interrogators*. Virginia: IOP Publishing Luna Innovations Incorporated, 2020.

[60] *ODiSI 6000 Data Sheet*. ODiSI6. REV.5.7. LUNA Innovations. 2022.

[61] Ali Masoudi and Trevor P. Newson. "Contributed Review: Distributed optical fibre dynamic strain sensing". In: *Rev. Sci. Instrum.* 87.1 (2016), p. 011501. ISSN: 0034-6748. DOI: 10.1063/1.4939482.

[62] R. Abbott et al. "Observation of Gravitational Waves from Two Neutron Star–Black Hole Coalescences". In: *Astrophys. J. Lett.* 915.1 (2021), p. L5. ISSN: 2041-8205. DOI: 10.3847/2041-8213/ac082e.

[63] B. Culshaw, D. E. N. Davies, and S. A. Kingsley. "Acoustic sensitivity of optical-fibre waveguides". In: *Electron. Lett.* 13.25 (1977), pp. 760–761. ISSN: 1350-911X. DOI: 10.1049/el:19770537.

[64] Andrew B. Lewis and Stuart Russell. "Method and Apparatus for Fiber Optic Intrusion Sensing". US-5194847-A. 1993.

[65] John Philip Dakin and Christopher Lamb. "Distributed fibre optic sensor system". GB2222247A. 1990.

[66] Andrew B. Lewis and Stuart Russell. "Method and Apparatus for Acoustic Sensing Using Multiple Optical Pulses". US-7742157-B2. 2010.

[67] A E Alekseev et al. "A phase-sensitive optical time-domain reflectometer with dual-pulse phase modulated probe signal". In: *Laser Physics* 24.11 (2014), p. 115106. DOI: 10.1088/1054-660x/24/11/115106.

[68] Stuart. Russell, Justin Peter Wiliam. Hayward, and Andrew B Lewis. "Acoustic Sensing Using an Optical Fibre". GB-2442745-A. 2006.

[69] Andrew B. Lewis and Stuart Russell. "Fibre Optic Distributed Sensing". US-20120278043-A1. 2012.

[70] R. Posey, G. A. Johnson, and S. T. Vohra. "Strain sensing based on coherent Rayleigh scattering in an optical fibre". In: *Electron. Lett.* 36.20 (2000), pp. 1688–1689. ISSN: 1350-911X. DOI: 10.1049/el:20001200.

[71] A Masoudi, M Belal, and T P Newson. "A distributed optical fibre dynamic strain sensor based on phase-OTDR". In: *Measurement Science and Technology* 24.8 (2013), p. 085204. DOI: 10.1088/0957-0233/24/8/085204.

[72] M. Johnson and Yv Delaporte. "A passive homodyne fibre vibrometer using a three-phase detector array". In: *Meas. Sci. Technol.* 4.8 (1993), pp. 854–859. ISSN: 0957-0233. DOI: 10.1088/0957-0233/4/8/010.

[73] Chang Wang et al. "Distributed acoustic mapping based on interferometry of phase optical time-domain reflectometry". In: *Opt. Commun.* 346 (2015), pp. 172–177. ISSN: 0030-4018. DOI: 10.1016/j.optcom.2015.02.044.

[74] Mahmoud Farhadiroushan, T. R. Parker, and Sergey Shatalin. "Method and Apparatus for Optical Sensing". US-20120060615-A1. 2012.

[75] Mahmoud Farhadiroushan, T. R. Parker, and Sergey Shatalin. "Optical Sensor and Method of Use". US-20120162639-A1. 2012.

[76] Roger Ian Crickmore and David John Hill. "Phase Based Sensing". US-8537345-B2. 2013.

[77] Hao Li et al. "Fading Suppression for Distributed Acoustic Sensing Assisted With Dual-Laser System and Differential-Vector-Sum Algorithm". In: *IEEE Sens. J.* 22.10 (2022), pp. 9417–9425. ISSN: 1558-1748. DOI: 10.1109/JSEN.2022.3164695.

[78] Dian Chen, Qingwen Liu, and Zuyuan He. "High-fidelity distributed fiber-optic acoustic sensor with fading noise suppressed and sub-meter spatial resolution". In: *Opt. Express* 26.13 (2018), pp. 16138–16146. ISSN: 1094-4087. DOI: 10.1364/OE.26.016138.

[79] A. H. Hartog et al. "The use of multi-frequency acquisition to significantly improve the quality of fibre-optic-distributed vibration sensing". In: *Geophys. Prospect.* 66.S1 (2018), pp. 192–202. ISSN: 0016-8025. DOI: 10.1111/1365-2478.12612.

[80] Andrew Biggerstaff Lewis and Stewart John Russell. "Fibre Optic Distributed Sensing". US-20120278043-A1. 2012.

[81] *MATLAB version 9.11.0.1873467 (R2021b)*. The Mathworks, Inc. Natick, Massachusetts, 2022.

[82] J. A. Bucaro and T. R. Hickman. "Measurement of sensitivity of optical fibers for acoustic detection". In: *Appl. Opt.* 18.6 (1979), pp. 938–940. ISSN: 2155-3165. DOI: 10.1364/AO.18.000938.

[83] Thomas G Giallorenzi, G H Sigel, and J A Bucaro. "Optical fiber sensor technology". In: vol. 18. 4. Optical Society of America, 1982, pp. 626–665. DOI: 10.1364/OFC.1982.ThGG1.

[84] F. Pockels. "Ueber die durch einseitigen Druck hervorgerufene Doppelbrechung regulärer Krystalle, speciell von Steinsalz und Sylvin". In: *Ann. Phys.* 275.3 (1890), pp. 440–469. ISSN: 0003-3804. DOI: 10.1002/andp.18902750313.

[85] R. Hughes and J. Jarzynski. "Static pressure sensitivity amplification in interferometric fiber-optic hydrophones". In: *Appl. Opt.* 19.1 (1980), pp. 98–107. ISSN: 2155-3165. DOI: 10.1364/AO.19.000098.

[86] John Schroeder. "Brillouin scattering and pockels coefficients in silicate glasses". In: *J. Non-Cryst. Solids* 40.1 (1980), pp. 549–566. ISSN: 0022-3093. DOI: 10.1016/0022-3093(80)90129-5.

[87] A. A. Zhirnov et al. "Influence of the Laser Frequency Drift in Phase-Sensitive Optical Time Domain Reflectometry". In: *Opt. Spectrosc.* 127.4 (2019), pp. 656–663. ISSN: 1562-6911. DOI: 10.1134/S0030400X1910031X.

[88] Juan Pastor-Graells et al. "Dynamic distributed measurement of temperature changes using phase-sensitive OTDR with chirped pulses". In: *Proceedings Volume 9916, Sixth European Workshop on Optical Fibre Sensors*. Vol. 9916. SPIE, 2016, pp. 387–390. DOI: 10.1117/12.2236192.

[89] Xin Lu and Katerina Krebber. "Phase error analysis and unwrapping error suppression in phase-sensitive optical time domain reflectometry". In: *Opt. Express* 30.5 (2022), pp. 6934–6948. ISSN: 1094-4087. DOI: 10.1364/OE.446517.

[90] Eileen R. Martin et al. "Introduction to Interferometry of Fiber-Optic Strain Measurements". In: *Distributed Acoustic Sensing in Geophysics*. American Geophysical Union (AGU), 2021. Chap. 9, pp. 111–129. ISBN: 9781119521808. DOI: 10.1002/9781119521808.ch9.

[91] T. Dean et al. "The Effects of Pulse Width on Fibre-optic Distributed Vibration Sensing Data". In: *European Association of Geoscientists & Engineers* 2016.1 (2016), pp. 1–5. ISSN: 2214-4609. DOI: 10.3997/2214-4609.201600684.

[92] A. E. Alekseev et al. "A phase-sensitive optical time-domain reflectometer with dual-pulse phase modulated probe signal". In: *Laser Phys.* 24.11 (2014), p. 115106. ISSN: 1054-660X. DOI: 10.1088/1054-660x/24/11/115106.

[93] Xin Lu et al. "Evaluating Phase Errors in Phase-Sensitive Optical Time-Domain Reflectometry Based on I/Q Demodulation". In: *J. Lightwave Technol.* 38.15 (2020), pp. 4133–4141. ISSN: 1558-2213. DOI: 10.1109/JLT.2020.2981439.

[94] Timothy Dean, Theo Cuny, and Arthur H. Hartog. "The effect of gauge length on axially incident P-waves measured using fibre optic distributed vibration sensing". In: *Geophys. Prospect.* 65.1 (2017), pp. 184–193. ISSN: 0016-8025. DOI: 10.1111/1365-2478.12419.

[95] Xin Lu and Katerina Krebber. "Characterizing detection noise in phase-sensitive optical time domain reflectometry". In: *Opt. Express* 29.12 (2021), pp. 18791–18806. ISSN: 1094-4087. DOI: 10.1364/OE.424410.

[96] A. Mateeva et al. "Advances in Distributed Acoustic Sensing (DAS) for VSP". In: *SEG Technical Program Expanded Abstracts 2012*. 2012, pp. 1–5. DOI: 10.1190/segam2012-0739.1.

[97] T.M. Daley et al. "Field testing of modular borehole monitoring with simultaneous distributed acoustic sensing and geophone vertical seismic profiles at Citronelle, Alabama". In: *Geophysical Prospecting* 64.5 (2016), pp. 1318–1334. DOI: 10.1111/1365-2478.12324.

[98] Alexis Constantinou et al. "Improving DAS acquisition by real-time monitoring of wireline cable coupling". In: *SEG Technical Program Expanded Abstracts 2016*. 2016, pp. 5603–5607. DOI: 10.1190/segam2016-13950092.1.

[99] Martin Karrenbach et al. "Hydraulic-fracturing-induced strain and microseismic using in situ distributed fiber-optic sensing". In: *The Leading Edge* 36.10 (2017), pp. 837–844. DOI: 10.1190/tle36100837.1.

[100] Julia Correa et al. "3D vertical seismic profile acquired with distributed acoustic sensing on tubing installation: A case study from the CO2CRC Otway Project". In: *Interpretation* 7.1 (2019), SA11–SA19. DOI: 10.1190/INT-2018-0086.1.

[101] Nathaniel J. Lindsey and Eileen R. Martin. "Fiber-Optic Seismology". In: *Annual Review of Earth and Planetary Sciences* 49.1 (2021), pp. 309–336. DOI: 10.1146/annurev-earth-072420-065213.

[102] N. M. Shapiro and M. Campillo. "Emergence of broadband Rayleigh waves from correlations of the ambient seismic noise". In: *Geophysical Research Letters* 31.7 (2004). DOI: 10.1029/2004GL019491.

[103] Shan Dou et al. "Distributed Acoustic Sensing for Seismic Monitoring of The Near Surface: A Traffic-Noise Interferometry Case Study". In: *Sci. Rep.* 7.11620 (2017), pp. 1–12. ISSN: 2045-2322. DOI: 10.1038/s41598-017-11986-4.

[104] Eileen R. Martin et al. "Seismic monitoring leveraging existing telecom infrastructure at the SDASA: Active, passive, and ambient-noise analysis". In: *The Leading Edge* 36.12 (2017), pp. 1025–1031. DOI: 10.1190/tle36121025.1.

[105] Nathaniel J. Lindsey et al. "City-Scale Dark Fiber DAS Measurements of Infrastructure Use During the COVID-19 Pandemic". In: *Geophysical Research Letters* 47.16 (2020), e2020GL089931. DOI: 10.1029/2020GL089931.

[106] Zack J. Spica et al. "Urban Seismic Site Characterization by Fiber-Optic Seismology". In: *Journal of Geophysical Research: Solid Earth* 125.3 (2020). DOI: 10.1029/2019JB018656.

[107] Jonathan B. Ajo-Franklin et al. "Distributed Acoustic Sensing Using Dark Fiber for Near-Surface Characterization and Broadband Seismic Event Detection". In: *Sci. Rep.* 9.1328 (2019), pp. 1–14. ISSN: 2045-2322. DOI: 10.1038/s41598-018-36675-8.

[108] Nathaniel J. Lindsey et al. "Fiber-Optic Network Observations of Earthquake Wavefields". In: *Geophysical Research Letters* 44.23 (2017), pp. 11, 792–11, 799. DOI: 10.1002/2017GL075722.

[109] Herbert F. Wang et al. "Ground motion response to an ML 4.3 earthquake using co-located distributed acoustic sensing and seismometer arrays". In: *Geophys. J. Int.* 213.3 (2018), pp. 2020–2036. ISSN: 0956-540X. DOI: 10.1093/gji/ggy102.

[110] Zefeng Li and Zhongwen Zhan. "Pushing the limit of earthquake detection with distributed acoustic sensing and template matching: a case study at the Brady geothermal field". In: *Geophysical Journal International* 215.3 (2018), pp. 1583–1593. ISSN: 0956-540X. DOI: 10.1093/gji/ggy359.

[111] Nathaniel J. Lindsey, T. Craig Dawe, and Jonathan B. Ajo-Franklin. "Illuminating seafloor faults and ocean dynamics with dark fiber distributed acoustic sensing". In: *Science* 366.6469 (2019), pp. 1103–1107. ISSN: 0036-8075. DOI: 10.1126/science.aay5881.

[112] Philippe Jousset et al. "Dynamic strain determination using fibre-optic cables allows imaging of seismological and structural features". In: *Nat. Commun.* 9.2509 (2018), pp. 1–11. ISSN: 2041-1723. DOI: 10.1038/s41467-018-04860-y.

[113] Veronica Rodriguez Tribaldos and Jonathan B. Ajo-Franklin. "Aquifer Monitoring Using Ambient Seismic Noise Recorded With Distributed Acoustic Sensing (DAS) Deployed on Dark Fiber". In: *J. Geophys. Res. Solid Earth* 126.4 (2021). ISSN: 2169-9313. DOI: 10.1029/2020JB021004.

[114] Ethan F. Williams et al. "Scholte wave inversion and passive source imaging with ocean-bottom DAS". In: *The Leading Edge* 40.8 (2021), pp. 576–583. DOI: 10.1190/tle40080576.1.

[115] Srikanth Jakkampudi et al. "Footstep detection in urban seismic data with a convolutional neural network". In: *The Leading Edge* 39.9 (2020), pp. 654–660. DOI: 10.1190/tle39090654.1.

[116] Robert J. Ferguson, Matthew A. D. McDonald, and David J. Basto. "Take the Eh? train: Distributed Acoustic Sensing (DAS) of commuter trains in a Canadian City". In: *J. Appl. Geophys.* 183 (2020), p. 104201. ISSN: 0926-9851. DOI: 10.1016/j.jappgeo.2020.104201.

[117] Jonathan B Ajo-Franklin et al. "Distributed Acoustic Sensing Using Dark Fiber for Near-Surface Characterization and Broadband Seismic Event Detection". In: *Scientific Reports* 9.1 (2019). DOI: 10.1038/s41598-018-36675-8.

[118] Robert J. Mellors et al. "Modeling Subsurface Explosions Recorded on a Distributed Fiber Optic Sensor". In: *J. Geophys. Res. Solid Earth* 126.12 (2021), e2021JB022690. ISSN: 2169-9313. DOI: 10.1029/2021JB022690.

[119] Tieyuan Zhu, Junzhu Shen, and Eileen R. Martin. "Sensing Earth and environment dynamics by telecommunication fiber-optic sensors: an urban experiment in Pennsylvania, USA". In: *Solid Earth* 12.1 (2021), pp. 219–235. ISSN: 1869-9510. DOI: 10.5194/se-12-219-2021.

[120] Diane Rivet et al. "Preliminary assessment of ship detection and trajectory evaluation using distributed acoustic sensing on an optical fiber telecom cable". In: *J. Acoust. Soc. Am.* 149.4 (2021), p. 2615. ISSN: 0001-4966. DOI: 10.1121/10.0004129.

[121] Ralph Posey. "Rayleigh scattering based distributed sensing system for structural monitoring". In: *Proceedings Volume 4185, Fourteenth International Conference on Optical Fiber Sensors*. Vol. 4185. SPIE, 2000, pp. 85–88. DOI: 10.1117/12.2302157.

[122] Peter G. Hubbard et al. "Quantifying the Surface Strain Field Induced by Active Sources with Distributed Acoustic Sensing: Theory and Practice". In: *Sensors* 22.12 (2022). ISSN: 1424-8220. DOI: 10.3390/s22124589.

[123] Albena Mateeva et al. "Distributed acoustic sensing for reservoir monitoring with vertical seismic profiling". In: *Geophys. Prospect.* 62.4 (2014), pp. 679–692. ISSN: 0016-8025. DOI: 10.1111/1365-2478.12116.

[124] Zhenghong Song, Xiangfang Zeng, and Clifford H. Thurber. "Surface-wave dispersion spectrum inversion method applied to Love and Rayleigh waves recorded by distributed acoustic sensing". In: *Geophysics* (2021). DOI: 10.1190/geo2019-0691.1.

[125] Joseph P. Vantassel et al. "Extracting High-Resolution, Multi-Mode Surface Wave Dispersion Data from Distributed Acoustic Sensing Measurements using the Multichannel Analysis of Surface Waves". In: *arXiv* (2022). DOI: 10.48550/arXiv.2202.04779.

[126] J. Virieux and S. Operto. "An overview of full-waveform inversion in exploration geophysics". In: *Geophysics* 74.6 (2009), WCC1–WCC26. ISSN: 0016-8033. DOI: 10.1190/1.3238367.

[127] Anton Egorov et al. "Elastic full-waveform inversion of vertical seismic profile data acquired with distributed acoustic sensors". In: *Geophysics* (2018). DOI: 10.1190/geo2017-0718.1.

[128] Matthew V. Eaid, Scott D. Keating, and Kristopher A. Innanen. "Multiparameter seismic elastic full-waveform inversion with combined geophone and shaped fiber-optic cable dataFWI with combined geophone and DAS data". In: *Geophysics* 85.6 (2020), R537–R552. ISSN: 0016-8033. DOI: 10.1190/geo2020-0170.1.

[129] Ronald N. Bracewell. *The Fourier Transform and Its Applications*. New York, NY, USA: McGraw-Hill, 1986. ISBN: 0-070070156.

[130] Farhad Ansari and Yuan Libo. "Mechanics of Bond and Interface Shear Transfer in Optical Fiber Sensors". In: *J. Eng. Mech.* 124.4 (1998), pp. 385–394. DOI: 10.1061/(ASCE)0733-9399(1998)124:4(385).

[131] Dong-Sheng Li et al. "Strain transferring analysis of fiber Bragg grating sensors". In: *Optical Engineering, 45(2)*. SPIE, 2006, p. 024402. DOI: 10.1117/1.2173659.

[132] Thomas Reinsch, Tom Thurley, and Philippe Jousset. "On the mechanical coupling of a fiber optic cable used for distributed acoustic/vibration sensing applications—a theoretical consideration". In: *Meas. Sci. Technol.* 28.12 (2017), p. 127003. ISSN: 0957-0233. DOI: 10.1088/1361-6501/aa8ba4.

[133] Michael S. Hons and Robert R. Stewart. *Transfer functions of geophones and accelerometers and their effects on frequency content and wavelets*. CREWES Research Report 18(3)18. Consortium for Research in Elastic Wave Exploration Seismology (CREWES), 2006.

[134] Charles A. Langston. "Spatial Gradient Analysis for Linear Seismic Arrays". In: *Bull. Seismol. Soc. Am.* 97.1B (2007), pp. 265–280. ISSN: 0037-1106. DOI: 10.1785/0120060100.

[135] S. A. L. de Ridder and A. Curtis. "Seismic gradiometry using ambient seismic noise in an anisotropic Earth". In: *Geophys. J. Int.* 209.2 (2017), pp. 1168–1179. ISSN: 0956-540X. DOI: 10.1093/gji/ggx073.

[136] Hugo Benioff. "A linear strain seismograph". In: *Bull. Seismol. Soc. Am.* 25.4 (1935), pp. 283–309. ISSN: 0037-1106. DOI: 10.1785/BSSA0250040283.

[137] Cinna Lomnitz. "Frequency response of a strainmeter". In: *Bull. Seismol. Soc. Am.* 87.4 (1997), pp. 1078–1080. ISSN: 0037-1106. DOI: 10.1785/BSSA0870041078.

[138] Eileen R. Martin et al. "Introduction to Interferometry of Fiber-Optic Strain Measurements". In: *Distributed Acoustic Sensing in Geophysics*. American Geophysical Union (AGU), 2021, pp. 111–129. ISBN: 978-1119521808. DOI: 10.1002/9781119521808.ch9.

[139] N. Anders Petersson and Bjorn Sjogreen. "geodynamics/sw4: SW4, version 2.0". In: *Zenodo* (2017). DOI: 10.5281/zenodo.1045297.

[140] J. D. Achenbach. *Wave Propagation in Elastic Solids*. Amsterdam: Elsevier, 1999. ISBN: 978-0720403251.

[141] Bin Luo, Frantisek Stanek, and Ge Jin. "Near-field strain of microseismic events in downhole DAS data". In: *First International Meeting for Applied Geoscience & Energy Expanded Abstracts*. Society of Exploration Geophysicists, 2021, pp. 402–406. DOI: 10.1190/segam2021-3582141.1.

[142] Aleksei Titov et al. "Modeling and interpretation of scattered waves in interstage distributed acoustic sensing vertical seismic profiling survey". In: *GEOPHYSICS* 86.2 (2021), pp. D93–D102. DOI: 10.1190/geo2020-0293.1.

[143] Kenneth H. Stokoe II et al. "NHERIUTexas Experimental Facility With Large-Scale Mobile Shakers for Field Studies". In: *Front. Built Environ.* 0 (2020). ISSN: 2297-3362. DOI: 10.3389/fbuil.2020.575973.

[144] Martin H. Weik. *Fiber Optics Standard Dictionary*. Second. Chapman & Hall, 1997. ISBN: 978-0442233877.

[145] Joseph P. Vantassel et al. "Characterization of the NHERI@UTexas Hornsby Bend Test Site". In: *DesignSafe-CI* (2022). DOI: 10.17603/ds2-bz52-ep82.

[146] *Kevlar Aramid Fiber Technical Guide*. 0319. Dupont. 2019. URL: https://www.dupont.com/content/dam/dupont/amer/us/en/safety/public/documents/en/Kevlar_Technical_Guide_0319.pdf.

[147] *Mechanical properties of Desmopan and Texin*. Covestro. 2019. URL: https://solutions.covestro.com/en/highlights/articles/theme/product-technology/mechanical-properties-tpu.

[148] Peter G. Hubbard et al. "Road Deformation Monitoring and Event Detection using Asphalt-embedded Distributed Acoustic Sensing (DAS)". In: *Struct Control Health Monit* e3067 (2022). DOI: 10.1002/stc.3067.

[149] FHWA. *Table HM-12 - highway statistics 2020 - policy: Federal Highway Administration*. United States: U.S. Department of Transportation/Federal Highway Administration, 2021.

[150] RD Holtz, WD Kovacs, and TC Sheahan. *An Introduction to Geotechnical Engineering*. New York: Pearson, 2011. ISBN: 978-0132497466.

[151] AASHTO. *AASHTO Guide for Design of Pavement Structures: 1993*. Washington, DC: American Association of State Highway and Transportation Officials, 1993.

[152] AASHTO. *Mechanistic-Empirical Pavement Design Guide: A Manual of Practice*. Washington, DC: American Association of State Highway and Transportation Officials, 2020.

[153] Wenjing Xue, Dong Wang, and Linbing Wang. "A Review and Perspective about Pavement Monitoring". In: *International journal of pavement research and technology* 5.5 (2012), pp. 295–302.

[154] Van Phuc Tran et al. "One stage detector (RetinaNet)-based crack detection for asphalt pavements considering pavement distresses and surface objects". In: *J. Civil Struct. Health Monit.* 11.1 (2021), pp. 205–222. ISSN: 2190-5479. DOI: 10.1007/s13349-020-00447-8.

[155] PE Sebaaly et al. *Instrumentation for flexible pavements-field performance of selected sensors*. Tech. rep. FHWA-RD-91-094. Washington, D.C.: Federal Highway Administration, 1992.

[156] M Huhtala et al. "Behavior of bituminous materials under moving wheel loads (with discussion)". In: *Journal of the Association of Asphalt Paving Technologists* 59 (1990), pp. 422–442.

[157] Zia Zafir, Raj Siddharthan, and Peter E Sebaaly. "Dynamic Pavement Strain Histories from Moving Traffic Load". In: *Journal of Transportation Engineering* 120.5 (1994), pp. 821–842. DOI: 10.1061/(ASCE)0733-947X(1994)120:5(821).

[158] A. Bayat, M. A. Knight, and Hamid R. Soleymani. "Field monitoring and comparison of thermal- and load-induced strains in asphalt pavement". In: *International Journal of Pavement Engineering* 13.6 (2012), pp. 508–514. DOI: 10.1080/10298436.2011.577776.

[159] Salil Gokhale et al. "Evaluation of Pavement Strain Gauge Repeatability: Results from Accelerated Pavement Testing". In: *Transportation Research Record* 2094.1 (2009), pp. 30–40. DOI: 10.3141/2094-04.

[160] Patricia Kara De Maeijer, Wim Van den bergh, and Cedric Vuye. "Fiber Bragg Grating Sensors in Three Asphalt Pavement Layers". In: *Infrastructures* 3.2 (2018), p. 16. ISSN: 2412-3811. DOI: 10.3390/infrastructures3020016.

[161] Samim Mustafa et al. "Identification of external load information using distributed optical fiber sensors embedded in an existing road pavement". In: *Optical Fiber Technology* 67 (2021), p. 102705. DOI: 10.1016/j.yofte.2021.102705. URL: https://www.sciencedirect.com/science/article/pii/S1068520021002558.

[162] Loizos Pelecanos et al. "Distributed Fiber Optic Sensing of Axially Loaded Bored Piles". In: *Journal of Geotechnical and Geoenvironmental Engineering* 144.3 (2018), p. 04017122. DOI: 10.1061/(ASCE)GT.1943-5606.0001843.

[163] Branko Glisic, Jeremy Chen, and David Hubbell. "Streicker Bridge: a comparison between Bragg-grating long-gauge strain and temperature sensors and Brillouin scattering-based distributed strain and temperature sensors". In: *Sensors and Smart Structures Technologies for Civil, Mechanical, and Aerospace Systems 2011*. Ed. by Masayoshi Tomizuka. Vol. 7981. International Society for Optics and Photonics. SPIE, 2011, pp. 674–683. DOI: 10.1117/12.881818.

[164] Huiyong Liu et al. "Vehicle Detection and Classification Using Distributed Fiber Optic Acoustic Sensing". In: *IEEE Trans. Veh. Technol.* 69.2 (Dec. 2019), pp. 1363–1374. ISSN: 1939-9359. DOI: 10.1109/TVT.2019.2962334.

[165] Nathaniel J Lindsey et al. "City-Scale Dark Fiber DAS Measurements of Infrastructure Use During the COVID-19 Pandemic". In: *Geophysical Research Letters* 47.16 (2020), e2020GL089931. DOI: 10.1029/2020GL089931.

[166] National Center for Statistics and Analysis. *Traffic safety facts 2019: A compilation of motor vehicle crash data*. Tech. rep. DOT HS 813 141. Washington, D.C.: National Highway Traffic Safety Administration, 2021.

[167] M P Huijser et al. *Wildlife-Vehicle Collision Reduction Study: Report To Congress*. Tech. rep. FHWA-HRT-08-034. McLean, VA: Federal Highway Administration, 2008.

[168] Ole Henrik Waagaard et al. "Real-time low noise distributed acoustic sensing in 171 km low loss fiber". In: *OSA Continuum* 4.2 (2021), pp. 688–701. ISSN: 2578-7519. DOI: 10.1364/OSAC.408761.

[169] Peter G. Hubbard et al. "Dynamic structural health monitoring of a model wind turbine tower using distributed acoustic sensing (DAS)". In: *J. Civil Struct. Health Monit.* 11 (2021), pp. 833–849. ISSN: 2190-5479. DOI: 10.1007/s13349-021-00483-y.

[170] Joyce Lee and Feng Zhao. *Global Wind Report 2019*. Brussels, Belgium: Global Wind Energy Council, 2020.

[171] United Nations. *Energy Statistics Yearbook 2001*. New York: United Nations Publication, 2004.

[172] United Nations. *Energy Statistics Yearbook 2018*. New York: United Nations Publication, 2021.

[173] Ryan Wiser, Mark Bolinger, and Eric Lantz. "Assessing wind power operating costs in the United States: Results from a survey of wind industry experts". In: *Renewable Energy Focus* 30 (2019), pp. 46–57. ISSN: 1755-0084. DOI: 10.1016/j.ref.2019.05.003.

[174] Danish Energy Agency and Energinet. *Technology data: Generation of electricity and district heating*. Denmark: IOP Publishing Danish Energy Agency, 2016.

[175] Wout Weijtjens et al. "Vibration based structural health monitoring of the substructures of five offshore wind turbines". In: *Procedia Eng.* 199 (2017), pp. 2294–2299. ISSN: 1877-7058. DOI: 10.1016/j.proeng.2017.09.187.

[176] Wonsul Kim et al. "Vibration-based Structural Health Assessment of a Wind Turbine Tower Using a Wind Turbine Model". In: *Procedia Eng.* 188 (2017), pp. 333–339. ISSN: 1877-7058. DOI: 10.1016/j.proeng.2017.04.492.

[177] Cong-Uy Nguyen et al. "Vibration-based damage detection in wind turbine towers using artificial neural networks". In: *1.* 5.4 (2018), p. 507. ISSN: 2288-6605. DOI: 10.12989/smm.2018.5.4.507.

[178] Chia Chen Ciang, Jung-Ryul Lee, and Hyung-Joon Bang. "Structural health monitoring for a wind turbine system: a review of damage detection methods". In: *Meas. Sci. Technol.* 19.12 (2008), p. 122001. ISSN: 0957-0233. DOI: 10.1088/0957-0233/19/12/122001.

[179] Gustavo Oliveira et al. "Vibration-based damage detection in a wind turbine using 1 year of data". In: *Struct. Control Health Monit.* 25.11 (2018), e2238. ISSN: 1545-2255. DOI: 10.1002/stc.2238.

[180] L. D. Avendaño-Valencia and S. D. Fassois. "Natural vibration response based damage detection for an operating wind turbine via Random Coefficient Linear Parameter Varying AR modelling". In: *J. Phys. Conf. Ser.* 628.1 (2015), p. 012073. ISSN: 1742-6588. DOI: 10.1088/1742-6596/628/1/012073.

[181] He Xianlong and She Tianli. "A New Identification Method for Bolt Looseness in Wind Turbine Towers". In: *Shock Vib.* 2019 (2019), p. 6056181. ISSN: 1070-9622. DOI: 10.1155/2019/6056181.

[182] Tuan-Cuong Nguyen et al. "Hybrid bolt-loosening detection in wind turbine tower structures by vibration and impedance responses". In: *Wind and Structures* 24.4 (2017), pp. 385–403. ISSN: 1226-6116. DOI: 10.12989/was.2017.24.4.385.

[183] M. Benedetti, V. Fontanari, and D. Zonta. "Structural health monitoring of wind towers: remote damage detection using strain". In: *Smart Mater. Struct.* 20.5 (2011), p. 055009. ISSN: 0964-1726. DOI: 10.1088/0964-1726/20/5/055009.

[184] Hyung-Joon Bang, Hong-Il Kim, and Kang-Su Lee. "Measurement of strain and bending deflection of a wind turbine tower using arrayed FBG sensors". In: *Int. J. Precis. Eng. Manuf.* 13.12 (2012), pp. 2121–2126. ISSN: 2005-4602. DOI: 10.1007/s12541-012-0281-2.

[185] P. Moyo et al. "Development of fiber Bragg grating sensors for monitoring civil infrastructure". In: *Eng. Struct.* 27.12 (2005), pp. 1828–1834. ISSN: 0141-0296. DOI: 10.1016/j.engstruct.2005.04.023.

[186] D E Hudson. *Synchronized vibration generators for dynamic tests of full-scale structures*. Pasadena, California: California Institute of Technology, 1962.

[187] R Crickmore and E Ku. "Fibre optic distributed sensing". US-10247584-B2. 2019.

[188] Yunjiang Rao et al. "Recent Advances in Phase-Sensitive Optical Time Domain Reflectometry (ϕ-OTDR)". In: *Photonic Sens.* 11.1 (2021), pp. 1–30. ISSN: 2190-7439. DOI: 10.1007/s13320-021-0619-4.